Quantitative investigation of group III-nitride interfaces by a combination of scanning tunneling microscopy and off-axis electron holography

Yuhan Wang

Information
Band / Volume 64
ISBN 978-3-95806-534-5

Mitglied der Helmholtz-Gemeinschaft

JÜLICH
Forschungszentrum

Schriften des Forschungszentrums Jülich
Reihe Information / Information Band / Volume 64

Forschungszentrum Jülich GmbH
Physik Nanoskaliger Systeme (ER-C-1)/
Mikrostrukturforschung (PGI-5)

Quantitative investigation of group III-nitride interfaces by a combination of scanning tunneling microscopy and off-axis electron holography

Yuhan Wang

Schriften des Forschungszentrums Jülich
Reihe Information / Information Band / Volume 64

ISSN 1866-1777 ISBN 978-3-95806-534-5

Bibliografische Information der Deutschen Nationalbibliothek.
Die Deutsche Nationalbibliothek verzeichnet diese Publikation in der
Deutschen Nationalbibliografie; detaillierte Bibliografische Daten
sind im Internet über http://dnb.d-nb.de abrufbar.

Herausgeber und Vertrieb: Forschungszentrum Jülich GmbH
Zentralbibliothek, Verlag
52425 Jülich
Tel.: +49 2461 61-5368
Fax: +49 2461 61-6103
zb-publikation@fz-juelich.de
www.fz-juelich.de/zb

Umschlaggestaltung: Grafische Medien, Forschungszentrum Jülich GmbH

Druck: Grafische Medien, Forschungszentrum Jülich GmbH

Schriften des Forschungszentrums Jülich
Reihe Information / Information, Band / Volume 64

D 82 (Diss. RWTH Aachen University, 2021)

ISSN 1866-1777
ISBN 978-3-95806-534-5

Contents

Chapter 1

Introduction

Due to the superior inherent properties, group III-nitride semiconductors have become the most promising material system for applications in solid state lighting devices and high power electronics,[1] such as laser diodes (LDs), light emitting diodes (LEDs),[2, 3, 4, 5] solar cells,[6] high-electron-mobility transistors (HEMTs) and metal oxide semiconductor field effect transistors (MOSFETs).[7, 8, 9]

For the realization of these devices, heterojunctions are required. The definition of a heterojunction is an interface between two layers with different chemical compositions which have unequal band structure, i.e. band gap, vacuum energy, electron affinity, and Fermi energy.[10] The band discontinuities thereby induce band alignments at the heterointerface to ensure that the Fermi levels of both materials are equal and continuous. The band alignment modifies the local band structure in the vicinity of the heterointerface and thus controls the motion of the charge carriers (carrier injection or confinement).[11] Depending on different applications, the relevant carrier transport is either across the interface (LDs, LEDs) or along the interface (MOSFETs).[12] Hence, an accurate and reproducible band alignment at the heterointerface is the most important challenge for heterojunction devices.

However, heterointerfaces give rise to localized features too, such as electronic interface states and polarization changes. These have the potential to considerably affect the band alignment and therefore the heterojunction devices' performance. Some of these localized electronic features induce also undesired changes on the band alignment at heterointerfaces, reducing the devices' efficiency: E.g. uncontrolled charging of interface states inducing band bending at the heterointerface may lead to a current collapse in field-effect transistors.[13, 14, 15] Particularly, polarization changes significantly affect the properties of heterojunctions and are mostly undesired.

Unlike silicon and GaAs, wurtzite group III-nitrides have large spontaneous and piezoelectric polarizations due to the noncentrosymmetric wurtzite structure.[16, 17] A two-dimensional sheet of bound charges at the heterointerface was reported to be caused by polarization changes,[18, 19] which pronouncedly affects electric fields and carrier distribution. The polarization-induced electric fields in quantum wells can result in the spatial separation of electrons and holes modifying recombination paths and rates. In addition the polarization-induced change of the shape of barriers enables otherwise forbidden transitions and thus reduces the multi-quantum-well LED devices' efficiency.[20, 21] The effective band gap can be reduced too due to the polarization-induced electric fields,[22, 23] leading to a red-shift in optical spectra.[24]

Therefore, polarization fields in group III-nitride semiconductors grown along the c direction are one of the most critical problem for quantum well devices. The origins of polarization fields at interfaces in group III-nitride semiconductors are the spatial displacement of the center of mass of N atom and group III atom in the wurtzite structure along the c direction as well as lattice relaxation at strained interface. In order to avoid polarization fields, the growth on nonpolar planes (perpendicular to c direction) has attracted significant interest due to the absence of the polarization fields along nonpolar directions.[25, 26, 27, 28] However, polarization fields in c direction can also be avoided by the so called polarization engineering, which is tuning the polarization by adjusting ternary or quaternary compositions.[29, 30, 31, 32, 33] A successful application of this rather delicate task requires sophisticated growth techniques on the one hand, but on the other hand advanced microscopic and spectroscopic characterization to critically scrutinize the growth results. Such microscopic and spectroscopic approaches need to give insight to interface properties such as polarization changes, sheet charges, lattice relaxation, electron affinity changes, etc.

However, such characterization, requiring atomic resolution as well as meV energy sensitivity, a rather difficult task. On the one hand, the band structure can be probed by X-ray photoelectron spectroscopy and ultraviolet photoelectron spectroscopy with high energy resolution,[34, 35, 36] but no sufficient spatial resolution. On the other hand, in order to obtain a high spatial resolution, electron microscopy and scanning probe microscopy are the characterization techniques of choice.[37, 38] Since conventional transmission electron microscopy (TEM) records the intensity information, it reveals primarily the chemical and structural properties. In this case, the phase information of the electron wavefunction is lost. Off-axis electron holography in TEM enables, however, access to both phase and amplitude of the electron wave. This opens the opportunity to derive quantitative information of the electrostatic fields at heterointerface from the recorded electron phase.[39, 40] Indeed, the electrostatic potential across the group III-nitride heterointerfaces has been investigated by off-axis electron holography previously.[41, 42, 43, 44] However, all these prior investigations are rather *qualitative*, and lack at closer look quantitative results. This arises from the influence of amorphized layers and defects at TEM lamellas on the surface potential as well as its screening toward the bulk. This surface potential critically modifies the average electrostatic potential probed by electron holography, covering up the intrinsic properties of materials and interfaces. Hence for a *quantitative* potential mapping by electron holography, the surfaces of the TEM lamellas have to be precisely characterized and the internal screening needs to be taken into account quantitatively.

In this thesis the path toward real quantitative electron holography is demonstrated. By determining the surface Fermi level pinning, arising from defects induced by the focused ion beam (FIB) preparation, electron holography can be calibrated. Thereby the polarization and electron affinity changes at group III-nitride heterointerfaces are probed quantitatively using a combination of off-axis electron holography, scanning tunneling spectroscopy (STS), secondary ion mass spectrometry (SIMS), and self-consistent simulations.

This thesis is structured as follows: The main experimental techniques employed for the characterization are described in Chapter 2. The sample description, e.g. sample compositions obtained by SIMS and sample structures, as well as the sample preparation for different techniques are given in Chapter 3. Investigations of group III-nitride heterostructures' surfaces and interfaces by cross-sectional scanning tunneling microscopy (STM) and STS are presented in Chapter 4. A quantitative characterization of electron affinity changes and polarization changes at heterointerfaces by combining off-axis electron holography, self-consistent simulation and SIMS are discussed in Chapter 5. In addition, a surface pinning level induced by the FIB preparation is identified. In Chapter 6, the electron affinity and polarization changes at heterointerfaces obtained in Chapter 5 are compared with expected values, which are derived from experimental and theoretical literature data and on basis of the lattice constant changes measured by scanning transmission electron microscopy (STEM). Chapter 7 summarizes the results.

Chapter 2

Theoretical and experimental background

2.1 Scanning tunneling microscopy

The scanning tunneling microscope, invented by Binnig and Rohrer in 1981,[45, 46] plays a very important role in the field of surface science. Compared with other surface sensitive instruments, the scanning tunneling microscope provides a direct observation of geometric and electronic surface structures with atomic resolution. It also can be utilized in many environments like vacuum, gases, and liquids, as well as at various temperatures.

A schematic of the scanning tunneling microscope is shown in Fig. 2.1. A metal-insulator-metal structure is formed by approaching a metal tip close to a surface of the metallic sample in vacuum. The principle of scanning tunneling microscopy (STM) is to measure the tunnel current between a metallic tip and the surface of a conductive sample, upon application of a voltage between the tip and the sample.

Piezo scanners drive the probe tip in x, y, and z directions with subatomic precision. To keep the tunneling current constant, the z piezo actuator is controlled by a feedback loop. Thus, by scanning the tip over the sample surface, a surface image can be obtained with an atomic resolution.[45] In the following the theoretical background for the interpretation of such images is described.

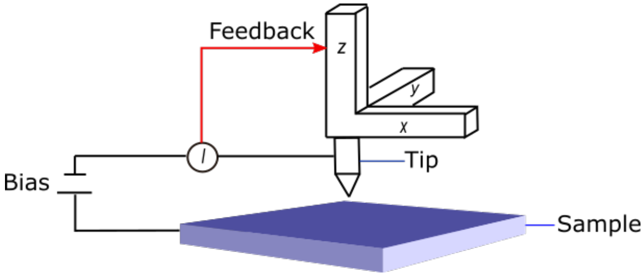

Figure 2.1: Principle of the scanning tunneling microscope. The tip is attached to a three-dimensional piezoelectric actuator. The x and y piezos control the scanning over the surface plane. The z piezo adjusts the tip-sample distance which is controlled by a feedback loop. Applying a voltage between the tip and the sample, generates a tunnel current, which is exponentially dependent on the tip-sample separation.

2.2 The concept of tunneling

2.2.1 One-dimensional model

To understand the basic principle of STM, the quantum mechanical tunneling effect needs to be recalled. In classical mechanics, an electron with a kinetic energy E is not able to pass a potential barrier V_0, if V_0 is larger than E. However, in quantum mechanics, the position and the momentum of an electron cannot be determined precisely at the same time. Hence, the electron is described by a wave function. The wave function can penetrate in a potential barrier, leading to a probability of transmission through the barrier. The transmission probability is given by the time-independent Schrödinger equation,[47]

$$-\frac{\hbar^2}{2m}\frac{\mathrm{d}^2}{\mathrm{d}z^2}\psi(z) + V(z)\psi(z) = E\psi(z) \tag{2.1}$$

Figure 2.2 shows a schematic illustration of the tunneling principle. $V(z)$ is shown as a red line and defined by

$$\begin{aligned} V(z) &= V_0 \quad , \quad 0 < z < d, \\ &= 0 \quad , \quad \text{otherwise.} \end{aligned} \tag{2.2}$$

In region I and III the kinetic energy of the electrons E is larger than the potential $V(z)$ in this region, while in region II it is smaller than the potential barrier V_0.

To solve the time-independent Schrödinger equation, we need to treat these three regions separately. Hence, the solution of Eq. 2.1 is given in three regions as follows:[48]

$$\begin{aligned} \Psi_{\mathrm{I}}(z) &= e^{ikz} + \widetilde{R}e^{-ikz}, \\ \Psi_{\mathrm{II}}(z) &= \widetilde{A}e^{i\kappa z} + \widetilde{B}e^{-i\kappa z}, \\ \Psi_{\mathrm{III}}(z) &= \widetilde{T}e^{ikz}, \end{aligned} \tag{2.3}$$

with the wave vector k

$$k = \sqrt{\frac{2m}{\hbar^2}(E - V(z))} \quad , E > V(z). \tag{2.4}$$

and the decay constant κ

$$\kappa = \sqrt{\frac{2m}{\hbar^2}(V(z) - E)} \quad , E < V(z). \tag{2.5}$$

where m is the electron mass and $\hbar$ is Planck's constant.

In region I, the plane wave consists of the incoming wave (e^{ikz}) and a wave reflected at the potential barrier ($\widetilde{R}e^{-ikz}$). In region II, the wave function is the sum of the wave function penetrating into the barrier from left side and its reflection from the right side of the barrier ($\widetilde{B}e^{-i\kappa z}$). In region III, only a transmitted wave function needs to be considered, since there is no incoming wave from the right side.

There are four coefficients $\widetilde{R}$, $\widetilde{A}$, $\widetilde{B}$, and $\widetilde{T}$ in the equations. $\widetilde{R}$ and $\widetilde{T}$ are the reflection and transmission coefficients, respectively. The probability of finding electrons behind the barrier is the absolute square of the transmission coefficient $|\widetilde{T}|^2$, given by[47]

$$|\widetilde{T}|^2 = \frac{4E(V_0 - E)}{4E(V_0 - E) + V_0^2 \sinh^2(d\kappa)}. \tag{2.6}$$

Thus, with a finite potential barrier V_0, even if the energy of electrons is smaller than the potential barrier V_0, the probability of electron transmission through the barrier is not zero. However, if the barrier is infinite, $|\widetilde{T}|^2$ tends to zero, which is called the classical limit. Furthermore, the transmission coefficient decays exponentially with the width of the potential barrier d.

Eq. 2.6 provides a basic model of the scanning tunneling microscope: The metal tip corresponds to area I. Region II represents vacuum and the width of the barrier is related to the distance between the tip and the sample. Region III is the sample.

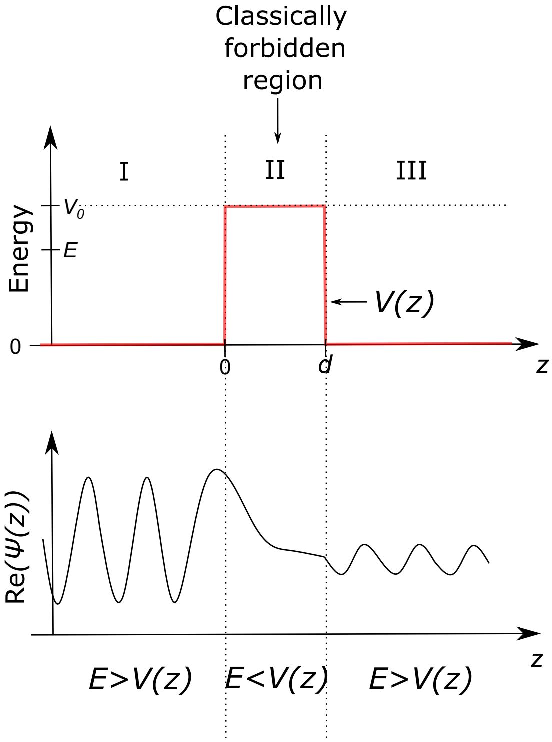

Figure 2.2: One-dimensional tunneling model with a potential barrier. The height of the potential barrier with rectangular shape in region II is V_0 and E is the kinetic energy of the electron. $\psi(z)$ is the wave function in the three regions. If the barrier is thin, the wave can pass through the potential barrier, which is a forbidden region in classical physics. Thus, the wave shows a non-zero probability $|\psi(z)|^2$ behind the potential barrier.

2.2.2 The tunneling current in Bardeen's model

Although the one-dimensional model is a simplified approximation of the real three-dimensional situation, it shows the fundamental properties of metal-vacuum-sample system.[49]

A more elaborate model for calculating the tunneling between two electrodes has been proposed by Bardeen.[50] It is based on solving the time-dependent Schrödinger equation for the tip states and the sample states separately. The tunneling from the tip to the sample is then treated as a perturbation.[51] The transition rate $\Gamma_{\mathrm{t}\rightarrow\mathrm{s}}$ can be expressed by Fermi's golden rule.[52, 53]

$$\Gamma_{\mathrm{t}\rightarrow\mathrm{s}} = \frac{2\pi}{\hbar}|M_{\mathrm{ts}}|^2\delta(E_{\mathrm{sample}} - E_{\mathrm{tip}}), \tag{2.7}$$

With E_{sample} and E_{tip} being the energy of the sample and tip states, respectively. The tunneling matrix element M_{ts} can be expressed by an integration over an arbitrary surface plane separating tip and sample[50]

$$M_{\mathrm{ts}} = \frac{\hbar^2}{2m}\int d\vec{S}(\psi_{\mathrm{t}}\vec{\nabla}\psi_{\mathrm{s}}^* - \psi_{\mathrm{s}}^*\vec{\nabla}\psi_{\mathrm{t}}). \tag{2.8}$$

The tunnel current is calculated by multiplying the total transition rate with the electron charge e and by summing up all initial and final states. Hence, the current is described by[54, 55]

$$I = \frac{4\pi}{\hbar}e\sum_{\mathrm{t,s}}|M_{\mathrm{ts}}|^2\delta(E_{\mathrm{sample}} - E_{\mathrm{tip}}). \tag{2.9}$$

This can be transformed into

$$I = \frac{4\pi}{\hbar}e\int_0^{eV}\rho_{\mathrm{tip}}(\varepsilon)\rho_{\mathrm{sample}}(\varepsilon)|M(\varepsilon)|^2 d\varepsilon, \tag{2.10}$$

with the density of the states of tip and sample, $\rho_{\mathrm{tip}}(\varepsilon)$ and $\rho_{\mathrm{sample}}(\varepsilon)$, respectively. The Fermi level of the sample is set to zero. Thus, the tip's Fermi level is at eV. Thus, the product of the densities of states of the tip and sample times the energy dependent matrix element have to be integrated over the whole energy range from the sample's to the tip's Fermi level.

To simplify the matrix element, we assume the potential barrier to be a one-dimensional rectangular barrier. Since we only consider elastic tunneling, i.e. $E_{\mathrm{sample}}{=}E_{\mathrm{tip}}{=}\tilde{E}$, the matrix element $M_{\mathrm{ts}}{=}M(\tilde{E})$ can be transformed into an energy dependent matrix element and it is given as[56]

$$M(\tilde{E}) = \frac{\hbar^2}{2m}\int d\vec{S}[\psi_{\mathrm{tip}}(z,\tilde{E})\nabla\psi^*_{\mathrm{sample}}(z,\tilde{E}) - \psi^*_{\mathrm{sample}}(z,\tilde{E})\nabla\psi_{\mathrm{tip}}(z,\tilde{E})], \quad (2.11)$$

The solutions of the wave function of tip and sample in the vacuum are[56]

$$\psi_{\mathrm{tip}}\left(z\right) = \psi_{\mathrm{tip}}\left(0\right)e^{-\kappa z} \quad (2.12)$$

and

$$\psi_{\mathrm{sample}}\left(z\right) = \psi_{\mathrm{sample}}\left(d\right)e^{\kappa(z-d)}, \quad (2.13)$$

respectively.

Both wave functions decay exponentially within the barrier. Inserting Eq. 2.12 and Eq. 2.13 into Eq. 2.11, the matrix element can be obtained to[56]

$$\begin{aligned} M(\tilde{E}) &= \frac{\hbar^2}{2m}\int 2\kappa\psi_{\mathrm{tip}}(0)\psi_{\mathrm{sample}}(d)e^{-\kappa z_s}e^{\kappa(z_s-d)}d\vec{S} \\ &= \frac{\hbar^2}{m}\kappa\psi_{\mathrm{tip}}(0)\psi_{\mathrm{sample}}(d)Ae^{-\kappa d}, \end{aligned} \quad (2.14)$$

where z_{s} is the position of the arbitrary surface plane used of integration and A is the area of the tunneling contact. $|M(\tilde{E})|^2$ corresponds to the transmission probability $T_{\mathrm{M}}(\phi, d)$ in the one-dimensional approximation. This yields the transmission probability[56]

$$T_{\mathrm{M}}(\phi, d) \propto \exp\left(-2d\sqrt{\frac{2m}{\hbar^2}\phi}\right). \quad (2.15)$$

where ϕ is the height of a rectangular barrier in a simple one-dimensional model. However, in reality the barrier is rather trapezoidal and depends on the work functions ϕ_{tip} and ϕ_{sample} of tip and sample, respectively, as well as on the applied voltage V. The energy diagrams in Fig. 2.3 illustrate the potential barrier without and with applied voltage V. The work functions are given by the minimum energy required to extract one electron to the vacuum energy level from the Fermi energy.

Without external voltage applied to the sample (Fig. 2.3 (a)), the potential barrier is defined by the work functions of tip and sample. The average height of the potential barrier can be approximated by ($\bar{\phi}$=(ϕ_{tip}+ϕ_{sample})/2). However, if a voltage is applied (Fig. 2.3 (b)), the Fermi level of the tip $E_{\mathrm{F,tip}}$ is shifted by eV with respect to the Fermi level of the sample $E_{\mathrm{F,sample}}$. This changes the height of the

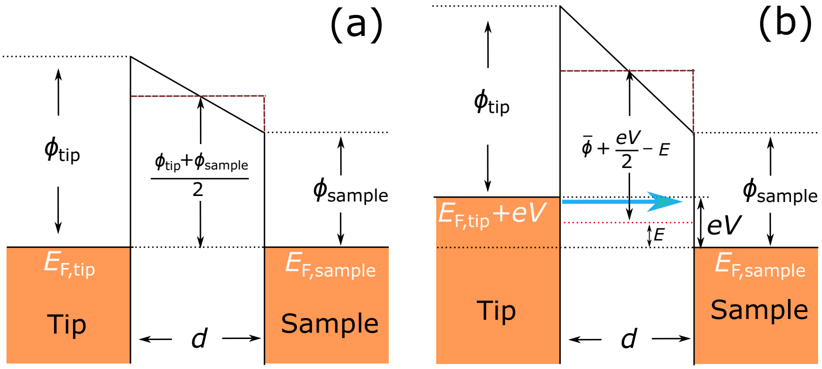

Figure 2.3: (a) Without external voltage, the tunneling barrier induced by a difference between the work function of the tip ϕ_{tip} and the sample ϕ_{sample}. (b) Tunneling barrier with an additional external voltage V applied. The application of e.g. a positive voltage at the sample relative to the tip shifts the filled states of the tip upward, such that they are facing empty states of the sample. Thus, an elastic tunnel current from the filled tip states into the empty sample states arises marked by the blue arrow. The height of the tunneling barrier is also changed by the applied voltage V. The image is modified from Ref. [56].

potential barrier as well. For a state with energy E, the tunneling barrier height changes to $\phi = \bar{\phi}$+$eV/2$-E, with 0≤ $E \leq eV$.

The transmission probability can be rewritten as a function of the width of the potential barrier d, work functions of the sample ϕ_{sample} and the tip ϕ_{tip}, and the applied voltage V[56]

$$T_{\text{M}}(E, eV, d) \propto \exp\left(-\frac{2d\sqrt{2m}}{\hbar}\sqrt{\frac{\phi_{\text{sample}}+\phi_{\text{tip}}}{2}+\frac{eV}{2}-E}\right). \tag{2.16}$$

2.2.3 The Tersoff-Hamann model

In the Tersoff-Hamann model[54, 55] two approximations are applied to Bardeen's tunneling model. First, the applied voltage between the tip and sample is assumed to have a neglectable small effect on the energy dependence of the matrix element and the density of the states. Thus, the matrix element is approximated as voltage independent and only valid for $V \ll \phi$. Second, the state of the tip is taken as a spherical s orbital. With these simplifications we only need to consider the center of tip $\vec{r_0}$ and the tip's work function in the tunnel current equation and we can rewrite the tunnel current as

$$I \propto \sum_{\mathrm{n}} |\psi_{\mathrm{n}}(\vec{r_0})|^2 \delta(E_{\mathrm{n}} - E_{\mathrm{F}}), \tag{2.17}$$

ψ_{n} and E_{n} are the surface wave functions and energies of all sample states.

With the sum being the sample's local density of states, evaluated at the position of the center of the tip $\vec{r_0}$, the tunnel current is given as[54, 55]

$$I \propto \rho_{\mathrm{sample}}(\vec{r_0}, E_{\mathrm{F}}), \tag{2.18}$$

The sample's density of states at the center of the tip can be related to the samples density of states at the sample surface by considering the exponential decay of the density of states into the vacuum.

$$\rho_{\mathrm{sample}}(\vec{r_0}, E_{\mathrm{F}}) = \rho_{\mathrm{sample}}(0, E_{\mathrm{F}}) \cdot e^{-2\kappa d}. \tag{2.19}$$

with d being now the separation of the center of the tip's s orbital to the sample surface.

2.3 Off-axis electron holography

Denis Gabor originally described electron holography using an electron microscope in 1948.[57] The advantage of using electron holography lies in the fact that it provides access to both, the phase and amplitude of the transmitted electron wave. In a conventional transmission electron microscope only the amplitudes can be probed. The phase change (cf. Fig. 2.4), caused by the transmission of the electrons through the sample, depends on the sample's electrostatic and magnetic fields. Hence, electron holography in a transmission electron microscope provides access to electrostatic potentials and magnetic fields simultaneously with high spatial resolution.

2.3.1 Hologram formation and recording

In this work, the off-axis electron holography mode has been used. In this mode an expanded but parallel electron beam is partially passing through the sample (object wave in Fig. 2.4(b)) and partially passing through vacuum (reference wave in Fig. 2.4(b)). An electron biprism, realized by a charged wire ($< 1\,\mu$m diameter), is mounted below the specimen (cf. Fig. 2.4). With applied voltage, the biprism deflects both parts of the electron beams, leading to an overlap region of the reference wave and the object wave (cf. Fig. 2.4(a)) at the detector and yielding the hologram. The hologram is recorded by a charged coupled device, with the intensity distribution[58]

$$I(r) = 1 + A^2(r) + I_{\mathrm{inel}}(r) + 2\mu A(r)\cos(2\pi q_c r + \mathit{\Phi}(r)) \tag{2.20}$$

where $A(r)$ and $\mathit{\Phi}(r)$ denote the amplitude and phase of the image wave, respectively. q_{c} is the carrier frequency of the interference fringes and μ is the contrast of fringes. An inelastic term is added as $I_{\mathrm{inel}}(r)$.

2.3.2 Hologram reconstruction

The recorded hologram of a 300 nm thickness lamella is shown in Fig. 2.5(a). From this interference pattern, the phase shift (and amplitude) of the electrons transmitted through the specimen is extracted using a reconstruction process. First, the hologram is Fourier transformed into three parts, in the form

$$\begin{aligned} \Im I(r) = {} & \Im[1 + A^2(r) + I_{\mathrm{inel}}(r)] \\ & + \delta(q + q_c) \otimes \mu\Im[A(r)e^{i\mathit{\Phi}(r)}] \\ & + \delta(q - q_c) \otimes \mu\Im[A(r)e^{i\mathit{\Phi}(r)}]. \end{aligned} \tag{2.21}$$

Figure 2.5(b) illustrates the calculated hologram by a Fourier transform. The central peak is derived from the conventional image and two sidebands are from the complex image wave. By selecting one of these sidebands and using an inverse Fourier transformation (IFT), a complex image can be obtained, including the amplitude (real part) and phase (imaginary part) information.

Neglecting the effects of dynamical diffraction and in the absence of magnetic fields, the phase shift caused by electric fields is given by the expression[59]

$$\Delta\phi\,(x, y, z) = C_{\mathrm{E}} \int (V_{\mathrm{EP}}\,(x, y, z) + V_{\mathrm{MIP}}\,(x, y, z))\,dz, \tag{2.22}$$

where z is the direction of incident electron beam, x, y are the in-plane projected positions within the sample. V_{EP} is the electrostatic potential and V_{MIP} is the mean

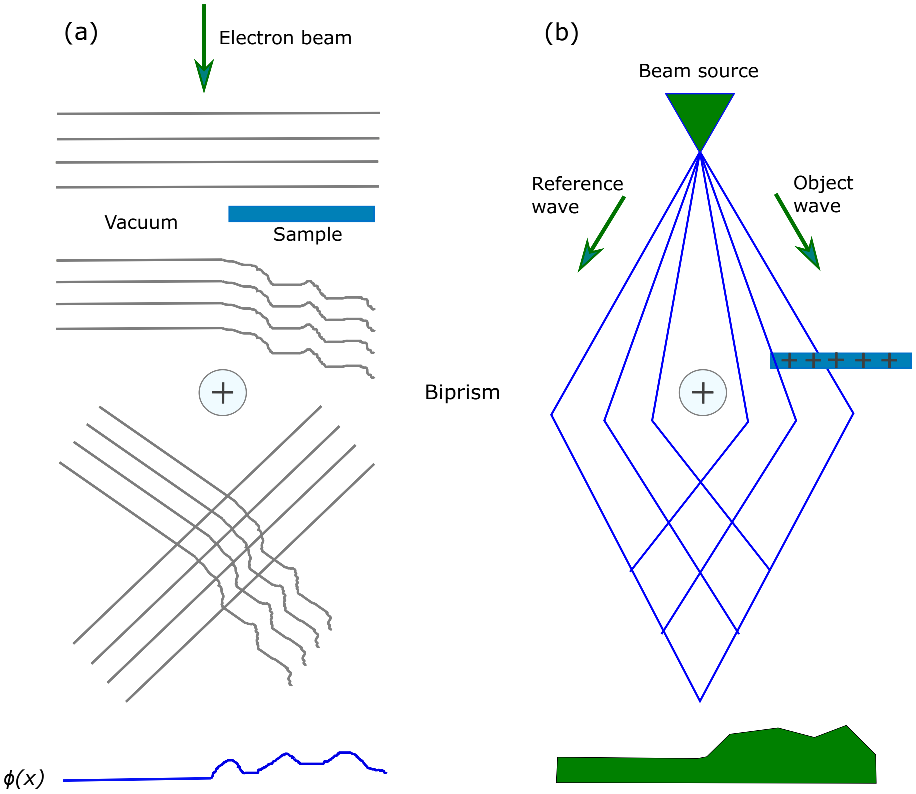

Figure 2.4: Schematic of off-axis electron holography in a transmission electron microscope. (a) Deformation of the wave fronts by the phase shift induced by the overlap of a vacuum reference electron wave and the electron wave that passes through the specimen. (b) Schematic of the beam paths of the vacuum reference and object waves in off-axis electron holography while applying a voltage on a biprism. Adapted from Ref. [42]

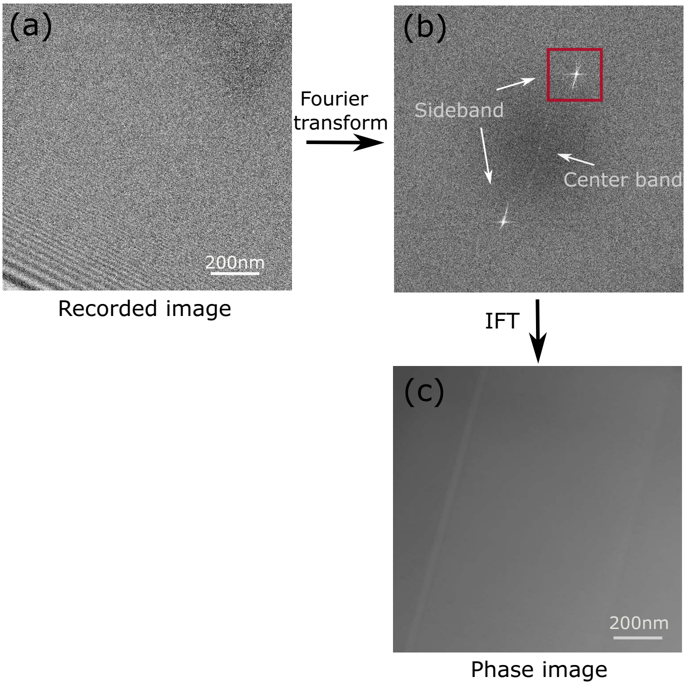

Figure 2.5: (a) Off-axis electron hologram obtained from a heterostructure lamella. (b) Fourier transform of the hologram. (c) Phase image derived by the inverse Fourier transformation (IFT) of the sideband marked in the red box.

inner potential (MIP). The constant C_E is given by

$$C_E = \frac{2\pi e}{\lambda E}\frac{E_0 + E}{2E_0 + E}. \tag{2.23}$$

E and E_0, are kinetic and rest mass electron energies, respectively. λ is the relativistic wavelength of incident wave, which depends on the acceleration voltage in the microscope. At 300 kV, C_E has a value of 6.53×10^6 rad/(V·m).

2.3.3 Self-consistent simulations of the phase changes

In order to calculate the electrostatic potential at the interface, we use the finite-difference algorithm for the solution of the Poisson equation as described in Ref.[60]. Since a polarization change is expected to exist at some interfaces, we extended the

Poisson equation by including the charge caused by the polarization change $\vec{P}$. It is given by

$$\Delta V_{\mathrm{EP}}(x, y, z) = -\frac{e}{\epsilon_0 \epsilon_r} \times [\rho(x, y, z) - \vec{\nabla} \cdot \vec{P}] \tag{2.24}$$

where $V_{\mathrm{EP}}(x, y, z)$ is the three dimensional electrostatic potential, ϵ_0 and ϵ_r are the vacuum and material's relative permittivity, respectively. $\rho(x, y, z)$ describes the three dimensional total charge density, which is given by $\rho(x, y, z)$=[$p(x, y, z)$-$n(x, y, z)$+N_D^+-N_A^+].[60] $p(x, y, z)$ and $n(x, y, z)$ denote the concentration of free charges (hole and electron, respectively) . The fixed ionized donor (acceptor) concentration is described by N_D^+ (N_A^+). Besides, $\vec{P}$ is the polarization consisting of both, spontaneous and piezoelectric polarization, with the assumption $\vec{P}$ is independent of the electric field $\vec{E}$. Hence, the electrostatic potential change is dependent on the charge distribution $\rho(x, y, z)$ and the polarization $\vec{P}$, built-in potentials, as well as surfaces states and much more.

We set the integration range in z direction to the width of the equidistant finite-difference grid used in the finite difference algorithm for the calculation of V_{EP} . In addition, two assumptions need to be applied: 1. The charge distribution in the lamella is not changed by the incident electron beam. 2. Without polarizations, the electrical and mechanical properties of materials are isotropically continuous.

Chapter 3

Sample description and preparation

3.1 The investigated heterostructure

3.1.1 Overview of sample

The investigated group III-nitride heterostructure sample (A3777) was grown by metal organic vapor phase epitaxy (MOVPE) at the École Polytechnique Fédérale de Lausanne (EPFL) in the Advanced Semiconductors for Photonics and Electronics Lab (LASPE).

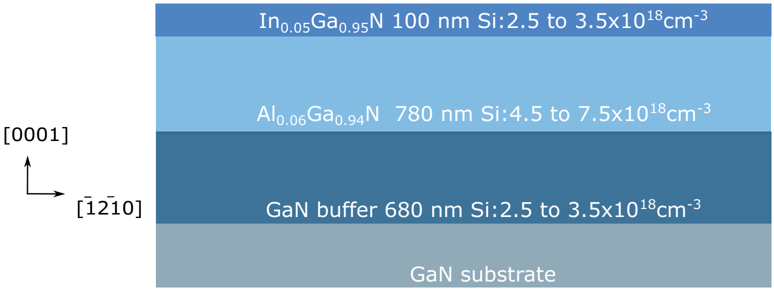

Figure 3.1: Schematic of the $In_{0.05}Ga_{0.95}N/Al_{0.06}Ga_{0.94}N/GaN$ heterostructure on a freestanding GaN substrate (sample number A3777). A 100 nm $In_{0.05}Ga_{0.95}N$ layer was grown on a 780 nm $Al_{0.06}Ga_{0.94}N$ layer deposited on a 680 nm GaN buffer layer, grown on a *c* plane freestanding GaN substrate by MOVPE. The thicknesses of layers shown were measured by SEM. All layers are Si doped.

The layer system, grown on a c plane free-standing GaN substrate, consists nominally of a 700 nm thick GaN buffer [Si doped: 2.5 to $3.5 \times 10^{18}\,\mathrm{cm}^{-3}$], 750 nm $\mathrm{Al_{0.06}Ga_{0.94}N}$ [Si doped: 4.5 to $7.5 \times 10^{18}\,\mathrm{cm}^{-3}$], and 100 nm $\mathrm{In_{0.05}Ga_{0.95}N}$ [Si doped: 2.5 to $3.5 \times 10^{18}\,\mathrm{cm}^{-3}$]. These nominal layer thicknesses were checked using scanning electron microscopy (SEM) and found to be slightly different in the actually grown sample: the GaN buffer and $\mathrm{Al_{0.06}Ga_{0.94}N}$ are 680 nm and 780 nm thick, respectively. Figure 3.1 illustrates the sample structure with corrected thicknesses.

3.1.2 Crystal structure of wurtzite structure group III-nitride compounds

The crystal structures of group III-nitride compounds are usually wurtzite and zincblende types. The difference between these two structures is the stacking sequence. The stacking sequence of the wurtzite structure is AaBbAaBb along the [0001] axis, whereas the zincblend structure is stacking along the [111] axis as AaBbCcAaBbCc. Since the sample we investigated has a wurtzite structure, we only discuss the wurtzite structure. Figure 3.2 displays the schematic of wurtzite structure. Three typical planes are represented in different colors (see in Fig. 3.2(a)). In Fig. 3.2(b), the atom structure is illustrated along the [0001] Ga-polar direction. The blue and green spheres represent the group III metal atom and the nitrogen atom, respectively. The tetrahedral geometry introduces a polarization along c direction. Thus, the c plane is a polar plane, whereas the a and m are nonpolar planes. The atom distribution in each plane are displayed in Fig. 3.2(c-e).

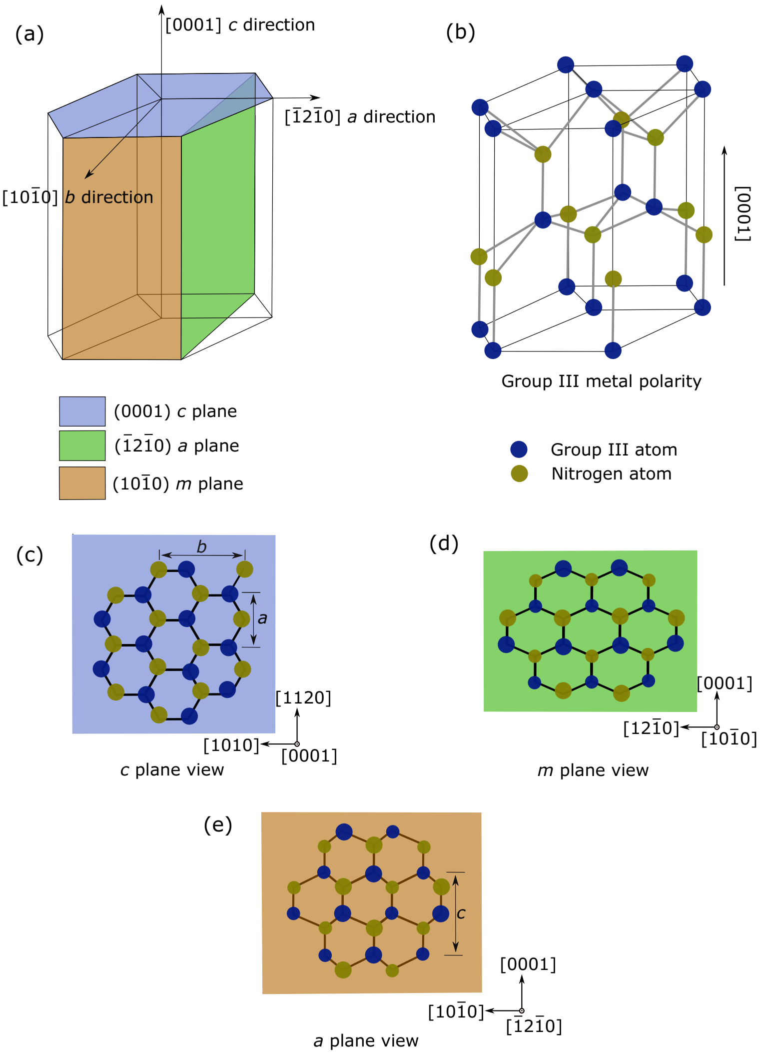

Figure 3.2: Crystal structure of wurtzite structure group III-nitride compounds. (a) Schematic of typical planes in wurtzite structure. a, c and m planes are shown in different colors. (b) Arrangement of atoms: group III atoms and nitrogen atoms. The primitive hexagonal structure position is occupied by Ga atoms and the [0001] Ga-polar direction is indicated by the arrow. (c) Distributions of atoms in c, (d) m, and (e) a planes in hexagonal structure. The projections reveal different stacking sequences of atoms. Lattice constants a, b and c are indicated by the double arrow.

3.1.3 Composition and doping profiles

Overview of compositions

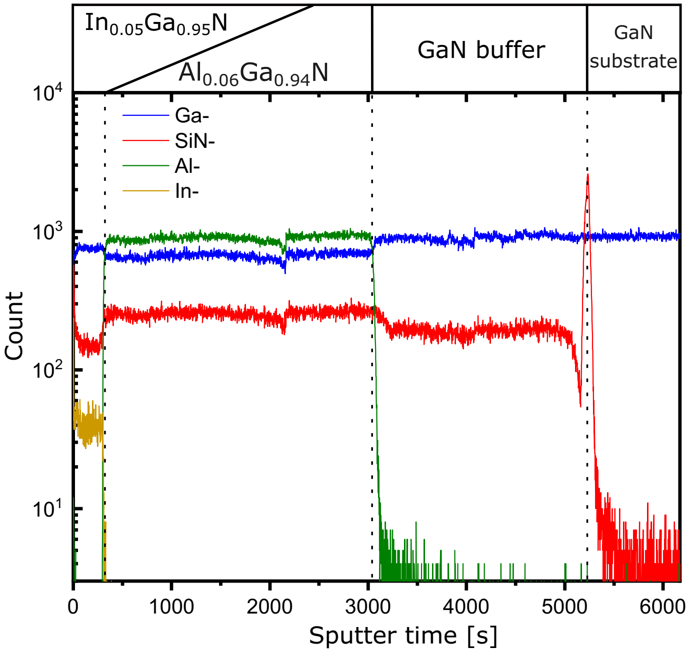

Figure 3.3: Counts of SiN^-, Ga^-, Al^-, In^- ions measured by SIMS as a function of sputter time. The blue line illustrates the distribution of Ga^- ions extracted along the growth direction. The green curve represents the count of Al^- ions, revealing an Al presence in one layer only, along with a decrease of Ga. Thus, it is related to the $Al_{0.06}Ga_{0.94}N$ layer. The counts of In^- ions are displayed by a yellow line, revealing an In composition only in the top layer. The red signal corresponding to the Si doping shows a nearly constant concentration in all layers, except at the GaN buffer/GaN substrate interface, where a delta-type Si doping is found.

SIMS was employed to determine the doping profile and check the order and types of the ternary alloy epitaxial layers. In the TOF.SIMS 5.NCS IONTOF GmbH system, Cs^+ ions (1 keV, 90 nA) were used as primary sputter beam to remove material in an area $300\times300\,\mu m^2$ wide. This is followed by a pulsed 30 keV Bi^+ ion beam for sampling the composition in the center within an area of $50\times50\,\mu m^2$. The sputtered secondary ions were collected and counted by a mass spectrometer.

An overview of the ion signals is illustrated in Fig. 3.3. The counts of Al^-, Ga^-, In^-, and SiN^- sputtered ions are shown as a function of sputter time, which is indicative of the depth from sample surface. The dashed lines indicate the „position“ of interfaces between the epitaxial layers.

The counts of Ga^-, Al^-, and In^- ions all agree well with the nominal sample structure. The counts of SiN^- ions are almost constant in all layers. This agrees well with the nominal doping concentrations in the epitaxial layers. However, a significant rise of the SiN^- ion count can be observed at GaN buffer/GaN substrate interface. It reveals a Si delta-type doping layer with high Si concentration at this interface.

Si concentration profile at GaN buffer/GaN substrate interface

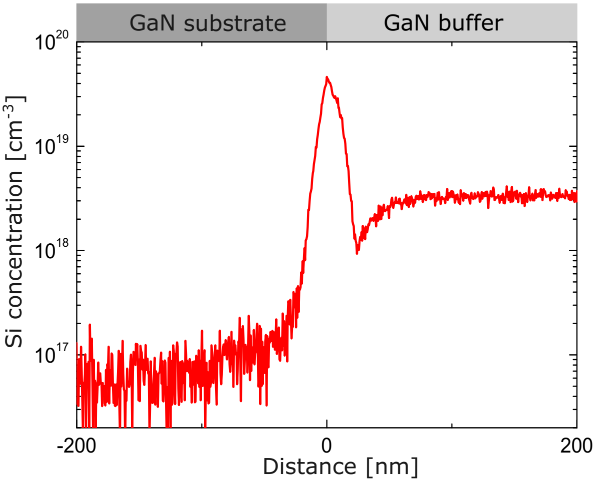

Figure 3.4: Concentration profile of Si, as a function of distance to the GaN substrate/GaN buffer interface. The profile reveals a delta-type doping peak at the interface, followed by a dip next to the interface in the GaN buffer.

To further quantify the width and the concentration profile of the Si delta-type doping layer at the GaN buffer/GaN substrate interface, the SiN^- ion intensity signal has been calibrated using a standard GaN MOVPE sample with a known Si concentration of $3 \times 10^{18}\,\mathrm{cm}^{-3}$.

Figure 3.4 shows the calibrated Si concentration profile as a function of distance to the GaN buffer/GaN substrate interface. The curve shows again a delta-type doping peak at the GaN buffer/GaN substrate interface with a dip on the side of the GaN buffer. The Si concentration peak reaches $5 \times 10^{19}\,\mathrm{cm}^{-3}$. The full width at half maximum (FWHM) of the Si peak is about 20 nm. The Si concentration in the buffer is constant at $3 \times 10^{18}\,\mathrm{cm}^{-3}$. The measured Si concentration in the substrate is at/below the detection limit.

3.2 Sample and tip preparation for cross-sectional scanning tunneling microscopy

The preparation for cross-sectional STM measurements includes two processes: First, tip preparation by electrochemical etching. Second, sample preparation for cleavage in the vacuum chamber of scanning tunneling microscope.

3.2.1 Tip preparation

For all investigations by cross-sectional STM in this thesis, tungsten tips are used. The tips are produced by electrochemical etching with a sodium hydroxide solution (NaOH). A platinum (Pt) ring is used as cathode and supports a free-standing film of the suspended NaOH solution. A tungsten wire with a diameter of 0.25 mm, as anode for the electrochemical reaction, is penetrating through the center of the NaOH film in the Pt ring. When a voltage is applied between the tungsten wire and the Pt ring, the following chemical reaction is induced:[61]

$$\begin{array}{rcl} \text{Anode:} & W_{(s)} + 8(OH)^- & \rightarrow WO_4^{2-} + 4H_2O + 6e^-, \\ \text{Cathode:} & 6H_2O + 6e^- & \rightarrow 3H_{2(g)} + 6(OH)^-, \\ \text{Overall:} & W_{(s)} + 2(OH)^- + 2H_2O & \rightarrow WO_4^{2-} + 3H_{2(g)} \end{array} \tag{3.1}$$

In order to obtain a tip without undesired products from chemical reactions, applying short pulses of reversed voltages is critical. It prevents oxide deposition on the tungsten tip.[62] A 3-4 mm long section of tungsten wire is etched off by this process and collected in a glass full of shaving foam. The aim is to damp the falling of the etched-off tip and thereby protect the apex of the tip. Afterwards, the tip is cleaned in distilled water followed by ethanol. Directly after cleaning, the tip is mounted in a tip holder and inserted into the vacuum chamber of scanning tunneling microscope to avoid contamination and oxidation.

The thickness and concentration of the NaOH film in the Pt ring significantly affect the tip properties. The best results are obtained using an approx 0.7 nm thick NaOH films and a 2 molar NaOH solution. The radius of curvature of the tip apex is ideally around 10 nm.[63, 64]

3.2.2 Sample preparation

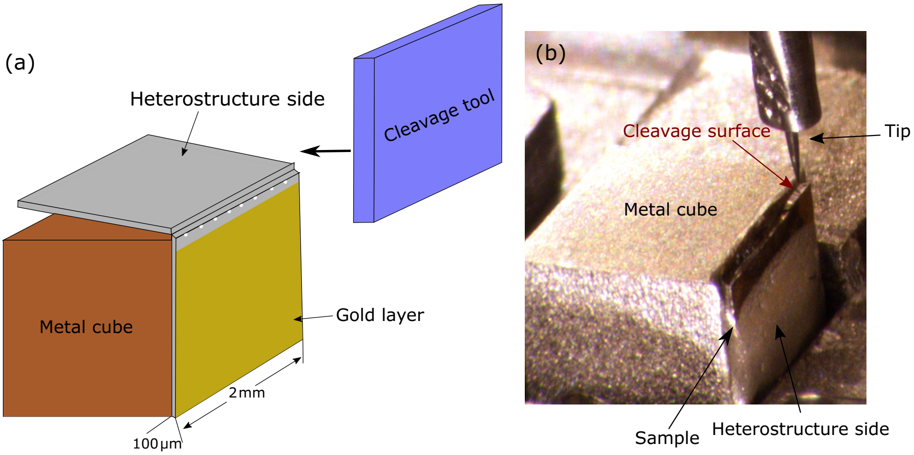

Figure 3.5: (a) Schematic diagram of sample preparation for cleavage. The white spots are pressed by a knoop indenter on the heterostructure side to define the cleavage plane. (b) Cleaved sample in the analysis chamber of the scanning tunneling microscope.

Since the sample needs to be cleaved in the vacuum chamber of scanning tunneling microscope, a suitable size and thickness are required. Therefore, the wafers were cut into roughly $2 \times 5\,\mathrm{mm}^2$ rectangular pieces, then grinded and polished from the substrate side to achieve a thickness of approximately $100\,\mu$m. To contact the samples electrically, a layer of gold was sputtered on one half of the samples from both sides. In fact, an electrical discharge is necessary, in order to merge the gold with the underlying semiconductor sample. In addition, a Knoop indenter was pressed on the heterostructure side at a few spots to define the cleavage plane. Finally, the sample was glued using an electrically conducting two-component adhesive on a metal cube, mounted afterwards on the sample holder. Directly after finishing all the preparation, the sample mounted on the holder was inserted into the load lock of the vacuum system to minimize contaminations.

Figure 3.5(a) illustrates the sample cleavage process. The samples were cleaved in ultra-high vacuum with a pressure of 1×10^{-10} mbar to ensure clean cleavage surfaces. The cleave was done by pushing the upper part of the sample with the heterostructure side against a cleavage tool. A uniform cleavage pressure is critical. Figure 3.5(b) shows the cleaved sample, transferred to the analysis chamber. An ideal cleavage surface is atomically flat and settled slightly above the metal cube at the positions defined by the Knoop indenter.

3.3 Preparation of lamella for off-axis electron holography

For investigation by off-axis electron holography, a thin electron transparent lamella is cut from the same sample investigated by STM previously. A SEM/FIB system, equipped with a gas injection system (GIS), is used for the lamella preparation. The system allows both electron- and ion-induced local deposition. First, to avoid damage from ion implantation and high acceleration voltage, the surface of the sample is coated by a thin layer ($\sim$20 nm) of electron-induced carbon, followed by a 2 μm thick layer of ion-induced carbon. Second, a thick lamella with the size of $\sim$10 μm in length, $\sim$5 μm in width and $\sim$2 μm in thickness is cut and lifted out by a tungsten needle in the FIB system.

Third, the thick lamella is transferred onto a heating chip and glued by ion-induced Pt deposition. Since we are interested in investigating the interfaces, the interfaces in the lamella have to be perpendicular to the lamella's surfaces and to the heating chips' surface, so that the interfaces would be edge-on in the TEM observation. But due to the complex structure of the heating chip, the lamella cannot be oriented exactly parallel to the heating chip. There is a small angle of about 7.5° between the heating chip and lamella. Figure 3.6(a) shows the overview of the lamella mounted on the heating chip before thinning. The deposed carbon and the interfaces system are indicated in this figure.

To further thin the lamella, the heating chip is manually rotated by 90°. The lamella is milled at a voltage of 30 kV, followed by polishing at low voltages of 5 kV and 2 kV to reduce the thickness of the amorphous and Ga implantation layer. The final thickness of the lamella is about 300 nm. Figure 3.6(b) shows an SEM secondary electron image illustrating the thickness and length of the lamella used for electron holography measurement.

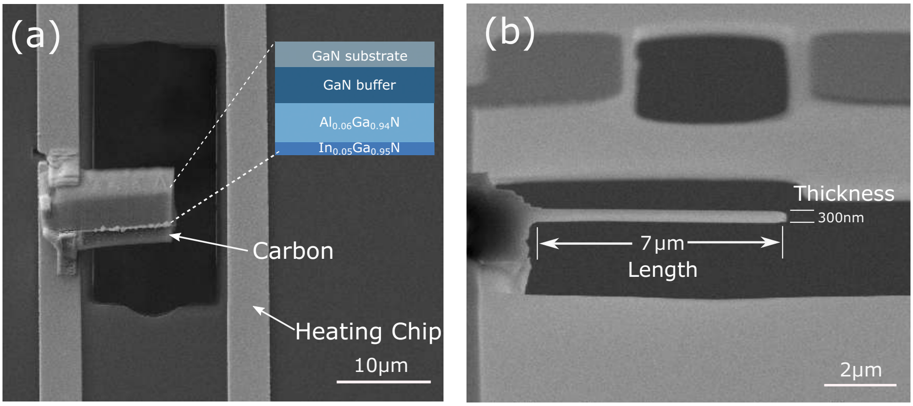

Figure 3.6: SEM images: (a) Overview of the lammela mounted on the heating chip before thinning. In the lamella, the carbon layer is deposed on the heterostructrue side and the orientation of the interfaces are perpendicular to the lamella's surfaces and the heating chips' surface. (b) After the lamella has been thinned, the final thickness and length are shown in the image.

Since the thickness of the lamella is a critical parameter for the quantitative analysis of the phase shift, an accurate thickness value is needed. The total thickness of the lamella has been measured to 296.4±1.3 nm by SEM. However, the convergent beam electron diffraction (CBED) determined a crystalline thickness to 277.9±1.3 nm. This indicates the lamella's surfaces are covered by approximately 9 nm amorphous layers, which is induced by FIB preparation (gray boxes in Fig. 3.7).[65] The amorphous layer is an electrically inactive layer,[66] which can be assumed to be homogenous over the whole sample and thus does not contribute to the local phase change. Thus, we use the crystalline thickness measured by CBED as the electrical active thickness.

After the preparation is finished, the lamella, mounted on the heating chip, is stored in a vacuum chamber to avoid contaminating until electron holography measurements can be performed.

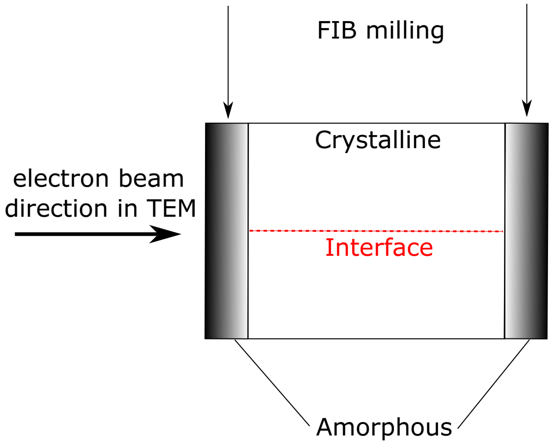

Figure 3.7: Schematic of an off-axis electron holography lamella, prepared by FIB milling. Thin and thick arrows indicate the incident beam direction for the FIB milling and the electron holography in TEM, respectively. The FIB preparation induced amorphous surface layers are illustrated in gray. They surround the crystalline region. The interface orientation in the heterostructure sample is indicated by a red dashed line.

Chapter 4

STM of nitride heterostructure

The aim of this chapter is to probe the electronic structure of the binary and ternary group III-nitride layers and their heterointerfaces using cross-sectional STM + STS on freshly cleaved *m* plane surfaces.

The chapter first presents the topography revealed in the STM images, then focuses on the spectroscopic properties of the different layer, deriving the influence of surface states, and finally addresses the spectroscopic features at the heterointerfaces.

4.1 Topography of the cross-sectional cleavage surface

Figure 4.1(a) shows a constant-current overview STM image of the whole heterostructure in cross-sectional view. One can recognize from left to right, the GaN substrate, the GaN buffer, the $\mathrm{Al_{0.06}Ga_{0.94}N}$ layer and $\mathrm{In_{0.05}Ga_{0.95}N}$ layer. Since the slow scan direction was not completely parallel to the interfaces, the 100 nm thin $\mathrm{In_{0.05}Ga_{0.95}N}$ layer is only visible as small, bright triangular area at bottom-right corner. The interface between the $\mathrm{In_{0.05}Ga_{0.95}N}$ and the $\mathrm{Al_{0.06}Ga_{0.94}N}$ layer is highlighted by a black dashed line. The other interfaces are marked by white dashed lines.

The presence of the interfaces gives rise to localized contrast changes in the constant-current STM images. The $\mathrm{Al_{0.06}Ga_{0.94}N}$/GaN and the $\mathrm{In_{0.05}Ga_{0.95}N}$/$\mathrm{Al_{0.06}Ga_{0.94}N}$ interfaces induce a downward and upward height change, respectively. The GaN buffer/GaN substrate interface shows up as bright contrast line.

In addition, the density and orientation of cleavage steps vary for the different layers. In the GaN substrate the density of steps is relatively low and the step

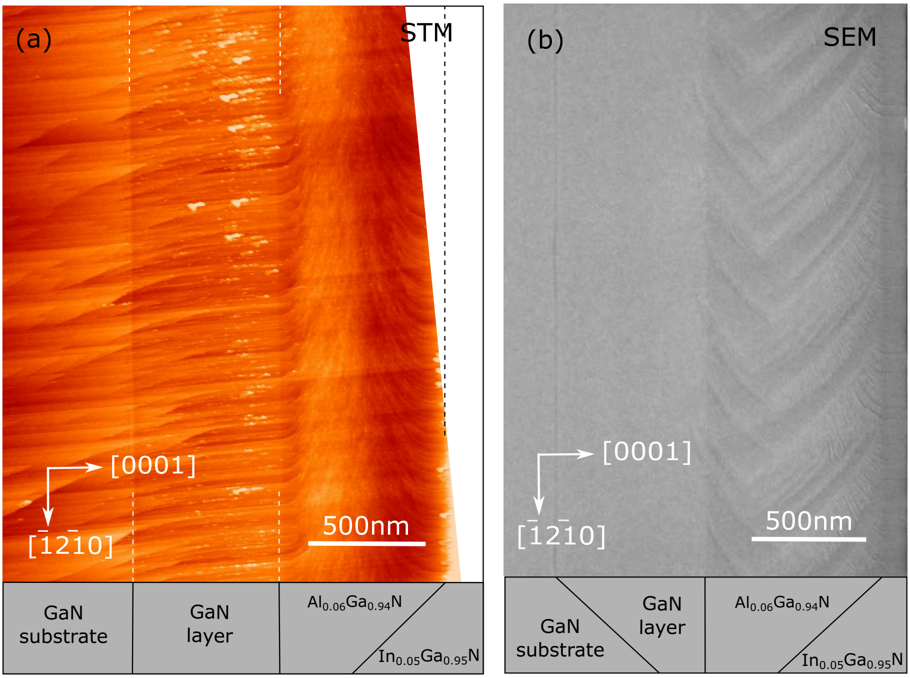

Figure 4.1: (a) Cross-sectional constant-current STM overview image of the $In_{0.04}Ga_{0.96}N/Al_{0.06}Ga_{0.94}N/GaN$ heterostructure measured at -2.5 V and 80 pA at a non-polar *m* plane cleavage surface. (b) SEM image acquired at the same cleavage surface. The different layers, as labeled at the bottom, can be discerned by different contrasts at the interfaces as well as different surface features. In particular, the density of cleavage steps in the $Al_{0.06}Ga_{0.94}N$ layer is significantly increased, while the step edge direction is bent towards the $[1\bar{2}10]$ direction at the center of this layer.

edges are oriented mostly in [0001] direction. In the GaN buffer layer the direction of the step edges remains unchanged, but the step density increases. In the first part of the $Al_{0.06}Ga_{0.94}N$ layer the steps start to bend towards the $[1\bar{2}10]$ direction. In addition, the step density increases strongly. In the second half of the $Al_{0.06}Ga_{0.94}N$ layer the steps bend backward to the [0001] direction, without clear further change of the step density.

This surface topography can be corroborated by SEM. The SEM image in Fig. 4.1(b), acquired on the same cleavage surface, exhibits similar features as compared to the STM image in Fig. 4.1(a). No contrast change can be recognized between the

GaN substrate and GaN buffer, except at the interface, where a dark line appears. The $Al_{0.06}Ga_{0.94}N$ layer exhibits a slightly darker contrast. In addition, a high step density, with step orientations bended similarly as detected by STM in Fig. 4.1(a), can be discerned. Finally the $In_{0.05}Ga_{0.95}N$ layer exhibits the darkest contrast with steps along [0001] direction.

4.2 STS of the ternary nitride layers

4.2.1 Experimental results

In this section we address the electronic properties of the different ternary group-III nitride layers. Since the contrast in constant-current STM images is determined by an interplay of topographic and electronic properties, the electronic structure can only be extracted using tunneling spectroscopy. Hence, STS measurements were performed on the freshly cleaved cross-sectional surface for this purpose.

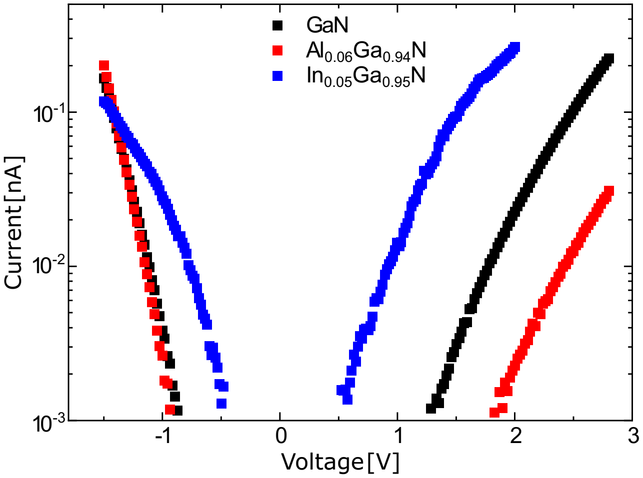

Figure 4.2: Averaged tunnel spectra of GaN, $Al_{0.06}Ga_{0.94}N$, and $In_{0.05}Ga_{0.95}N$, shown as black, red, and blue filled symbols, respectively. The spectra were measured at a freshly cleaved *m* plane surface, sufficiently far away from the layers' interfaces, using a setpoint of -1.4 V and 80 pA.

The averaged $I-V$ spectra of GaN, $Al_{0.06}Ga_{0.94}N$, and $In_{0.05}Ga_{0.95}N$ are shown as black, red, and blue filled symbols in Fig. 4.2, respectively. The spectra were obtained at regions sufficiently far away from interface areas. All spectra show semiconducting properties, characterized by a voltage range without detectable tunnel current close to 0 V. We denote this range as apparent band gap. The boundary of this voltage range is delimited by so-called onset voltages. Although the nominal band gaps of GaN, $\mathrm{Al_{0.06}Ga_{0.94}N}$ and $\mathrm{In_{0.05}Ga_{0.95}N}$ do not vary much owing to the small Al and In contents, the spectra of the three layers exhibit significant differences in their onset voltages: The tunnel current of $\mathrm{In_{0.05}Ga_{0.95}N}$ exhibits significantly smaller onset voltages for both, the negative and the positive voltage branches, as compared to GaN and $\mathrm{Al_{0.06}Ga_{0.94}N}$. The negative branches of tunnel current of GaN and $\mathrm{Al_{0.06}Ga_{0.94}N}$ exhibit similar onset voltages close to -1 V, but the onset-voltage of the positive branch is much larger for $\mathrm{Al_{0.06}Ga_{0.94}N}$ (+1.8 V) as compared to GaN (+1.2 V), and $\mathrm{In_{0.05}Ga_{0.95}N}$ (+0.5 V). If we define the noise level of the tunnel current in this measurement to be 1 pA, the apparent band gap is $\sim$ 1 eV, 2.3 eV, and 2.8 eV, for $\mathrm{In_{0.05}Ga_{0.95}N}$, GaN and $\mathrm{Al_{0.06}Ga_{0.94}N}$, respectively. These apparent band gaps do not agree with the fundamental band gaps.

Furthermore, the onset voltages are also influenced by the step density. Figure 4.3 illustrates the onset voltages of the tunnel current obtained at regions with different step densities within the $\mathrm{Al_{0.06}Ga_{0.94}N}$ layer, as indicated in the STM image shown as inset. The negative current branch remains unchanged with step density. Only the positive current branch changes. In the inset, one can recognize that the areas of the cleaved $\mathrm{Al_{0.06}Ga_{0.94}N}$ layer toward the underlying GaN buffer and overlying $\mathrm{In_{0.05}Ga_{0.95}N}$ layer exhibit a lower step density with steps being oriented primarily along [0001] direction. In between the step density is much higher and the orientation of the steps is bended toward the $[1\bar{2}10]$ direction. Hence, the onset voltages of the positive tunnel current branch increases with step density. This is corroborated by a voltage line profile at constant current, extracted from the current-imaging-tunneling spectroscopy (CITS) map evaluated at 0.02 nA, across the $\mathrm{Al_{0.06}Ga_{0.94}N}$ layer (cf. Fig. 4.4). The line profile demonstrates an increase of the voltage in regions with higher step density, as compared to the regions with lower step density. Note, the electronic properties of the interfaces modify the voltage profile near the interfaces.

4.2.2 Discussion of the tunneling spectra of m plane group III-nitride surfaces

At this stage, the origin of the tunnel current needs to be recalled. At negative voltages, electrons tunnel out from the filled states in the valence band of the

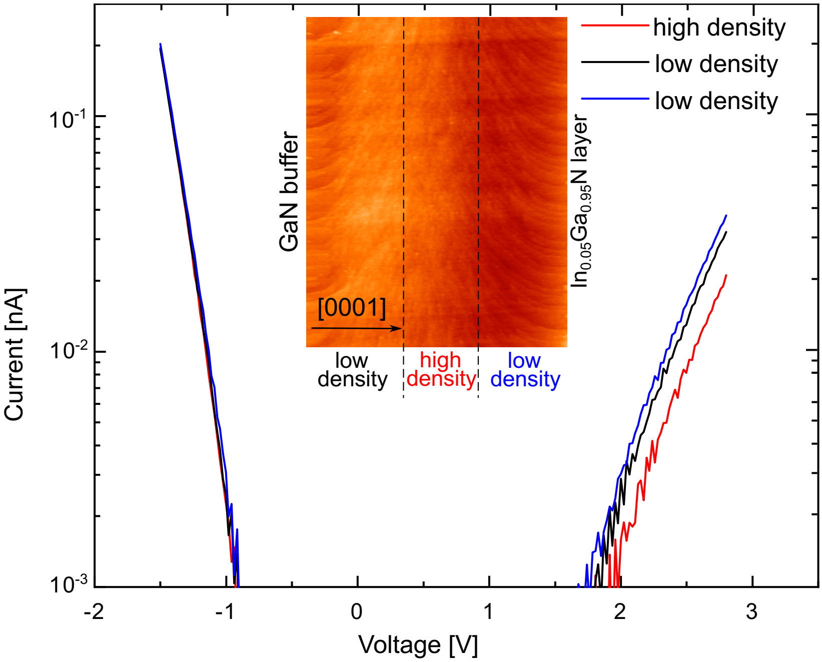

Figure 4.3: Averaged tunnel spectra measured at different regions within the $Al_{0.06}Ga_{0.94}N$ layer at a m plane cleavage surface. The black and blue I-V curves were measured at regions with lower step densities, while the red spectrum has been acquired at the center of the layer, where a higher step density is present. The setpoint is -1.4 V and 80 pA. The morphology of the step edges within the $Al_{0.06}Ga_{0.94}N$ layer is illustrated by the STM image in the inset. Regions with higher and lower step density are separated by dashed black lines.

sample surface to the tip (current from the valence band I_V). At positive voltages, electrons are driven from the tip to the empty sample states in the conduction band of the sample surface (current into the conduction band, I_C). Under a flat band conditions (cf. Fig. 4.5(a)), the band gap of the surface is given by the voltage range without detectable tunnel current in tunneling spectra. However, the presence of the surface state and the tip-induced band bending significantly change the spectra, such that a straight forward interpretation is not possible anymore.

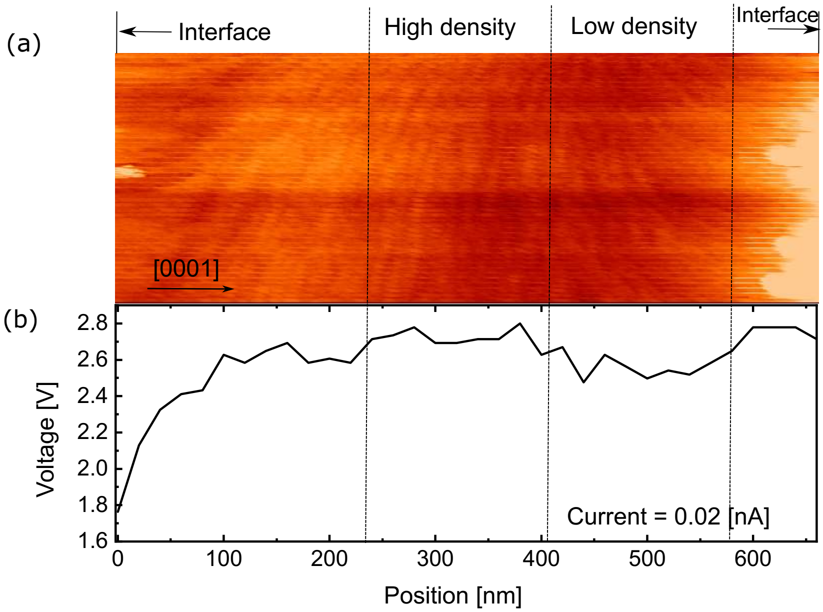

Figure 4.4: (a) Cross-sectional constant-current STM image, depicting regions of higher and lower step densities within the $Al_{0.06}Ga_{0.94}N$ layer. Setpoint and orientation are the same as for the STM image in the inset of Fig. 4.3. (b) Voltage line profile at constant current, extracted from the CITS maps by evaluating the inversed tunnel spectra $V(I)$ at 20 pA across the regions with different step densities, as indicated by the dashed black lines. Indeed, an increased voltage $V(20\,\mathrm{pA})$ in high step density areas is found.

Tip-induced band bending

The electric field induced by the voltage applied between tip and sample penetrates into the sample where it is screened by a redistribution of the free charge carriers. This leads to an upward or downward bending of band edges (depending on the polarity of the applied voltage).[67] This process is called tip-induced band bending.

If no surface states are present in the fundamental band gap, the Fermi level is not pinned (called *unpinned* surface in the following). In this case, the band edges follow the electrostatic potential that penetrates into the sample.

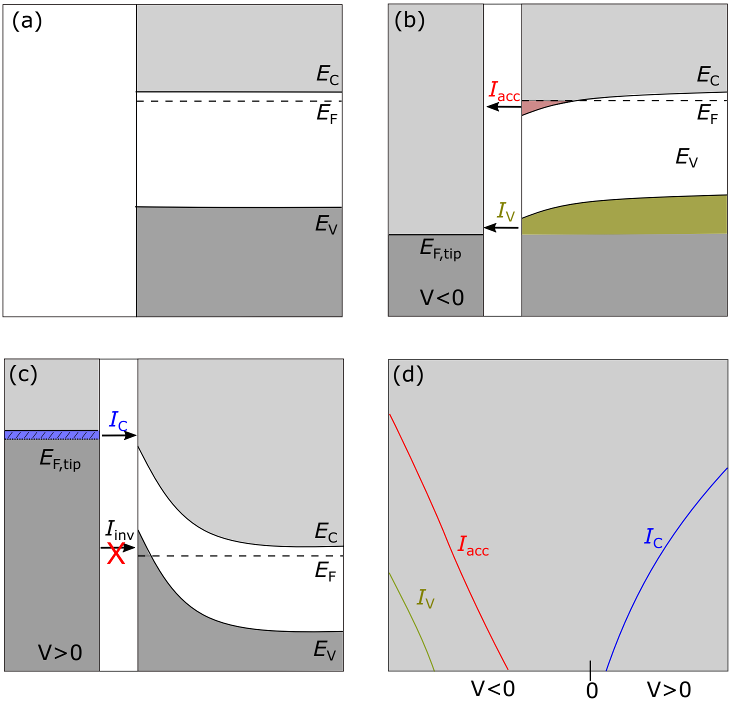

Figure 4.5: Schematic band diagrams (a-c) of an *unpinned*, n-type semiconductor surface for different cases: (a) In absence of a metal tip, the band edges (i.e. the valence band maximum E_V and the conduction band minimum E_C) are unchanged throughout the whole semiconductor. (b) In presence of a negatively biased tip, the applied potential penetrates into the sub-surface region of the sample leading to a downward band bending. If E_C is dragged below the Fermi level, an electron accumulation arises (red). These accumulated electrons can tunnel to the tip, giving rise to a tunnel current I_{acc}. For sufficiently large negative voltages, tunneling out of filled valence band states (green) into the tip emerges (denoted as I_V). (c) For a positively biased tip, tunneling from tip states (blue) into empty conduction band states (denoted as I_C) arises already at small voltages, since the Fermi level is close to E_C. With increasing positive voltage, the band edges bend further upwards and E_V can be dragged above the Fermi level. In thermal equilibrium, this would lead to an inversion zone, i.e. an accumulation of holes at the sample's surface. However, under tunneling conditions, no holes will be present at the surface due to a sufficiently large supply of tip electrons which can tunnel instantly into arising empty valence band states. Thus, an inversion zone cannot be sustained. (d) Resulting tunnel current components of an unpinned n-type semiconductor surface. At positive voltages, tunneling into empty conduction band states is probed, while at negative voltages tunneling out of the conduction band's accumulation zone is dominant.

Figures 4.5(b) and (c) illustrate schematically the tip-induced band bending at an unpinned n-type surface. E_V and E_C denote the bulk valence band maximum and the bulk conduction band minimum, respectively. In the absence of the tip, the bands are unchanged from the bulk towards the surface (i.e. flat bands, cf. Fig. 4.5(a)). Upon approaching a tip to the surface, the band edges are shifted downwards or upwards for negative or positive applied voltage, respectively.

At negative voltages (cf. Fig. 4.5(b)), the downward band bending drags the conduction band below the Fermi level for n-type material. This creates an accumulation of electrons in the conduction band. These accumulated electrons can tunnel into the empty states of the tip. This component of the tunnel current is called accumulation current I_acc.[68] Hence, the negative branch of the tunneling spectrum is a sum of the current from the valence band (I_V) and from the accumulation layer in the conduction band (I_acc).

Note, the accumulation current I_acc dominates if the surface band gap is a direct band gap (surface band gap at the $\overline{\Gamma}$ point),[69, 70] as e.g. GaN($10\bar{1}0$). In this case, the valence band states cannot be probed. In contrast, for indirect surface band gap materials, where the surface conduction band edge is located at the edge of the Brillouin zone, the accumulation current is suppressed and hence, the current from the valence band I_V dominates. This suppression arises from momentum conservation in elastic tunneling:[68] Electrons in the accumulation layer have a non-zero momentum, which can be accommodated in the tip with lower probability only.

At positive voltages (see Fig. 4.5(c)) the tunnel current into the conduction band (I_C) starts close to 0 V, since the Fermi level of an n-type semiconductor is situated close to the conduction band. At larger positive voltages, the valence band edge can be dragged in principle above the Fermi level, creating an inversion zone (i.e. accumulation of minority carriers). However, under tunneling conditions, the inversion zone cannot be maintained as electrons tunnel with higher probability into the inversion zone, as they can be removed from it.[68] Hence, at positive voltages only tunneling into conduction band occurs.

Figure 4.5(d) illustrates the resulting components of the tunnel current for the case of an unpinned GaN nonpolar surface. At negatives voltages, the dominant component of the tunnel current arises from tunneling out of filled conduction band states I_acc, whereas at positive voltages, the tunnel current is composed of tunneling into empty conduction band states (I_C). Hence at both voltage polarities, the conduction band is probed.[71] Therefore, no fundamental band gaps can be measured for nonpolar group III-nitride surfaces.

Surface states

In general, surfaces exhibit surface states. The influence of these surface states on the electronic properties depends primarily on the energetic position and on their density. Therefore, one has to discuss the different possible types of surface states. Surface states can categorized as intrinsic or extrinsic.

Extrinsic surface states arise from defects of the crystal structure or adsorbates, such as vacancies, steps or contaminations. In the present case of a freshly cleaved surface in ultra high vacuum, contaminations can be ruled out. The STM images suggest that the dominating extrinsic defects are rather cleavage steps.

Intrinsic surface states are related to the termination of the bulk and reconstruction of the surface. In the present case of a non-polar m plane surface of group III-nitrides, the intrinsic surface states are derived by the nitrogen- and group-III dangling bonds.

Both types of surface states can result in a surface Fermi level pinning, if the energy of the surface state is in the fundamental band gap. The nitrogen derived dangling bond is situated at the valence band edge for all group-III nitrides. For pure InN, the In derived surface state is in the conduction band.[72] Hence these states do not play a significant role for the pinning.

However, the empty group-III derived dangling bond is for GaN and AlN in the upper half of the fundamental band gap[73, 74] and surface states arising from cleavage steps are typically energetically located close to midgap position. These intrinsic and extrinsic gap states induce Fermi level pinning.

Figure 4.6 shows the schematic band diagrams for the example of the n-type GaN nonpolar surface, (a) pinned by the intrinsic empty surface state and (b) by extrinsic surface states (i.e. steps-induced). The minimum of the Ga-derived empty surface state $\mathrm{S_{Ga}}$ lies at around 1 eV below the bulk conduction band minimum E_C, whereas the N-derived occupied surface state $\mathrm{S_N}$ is located at the bulk valence band maximum E_V (0 eV) (cf. Fig 4.6(a)).[73] In addition, the step-induced extrinsic surface state, located at the middle of the bulk band gap, is schematically illustrated in Fig 4.6(b). For both cases, the Fermi level of the semiconductor and the surface state level align in electronic equilibrium without an applied electric field. Hence, the $\mathrm{S_{Ga}}$ and step-induced surface state are partially occupied. This occupation leads to a pinning of the Fermi level, thus the conduction band edge is bent towards upward.

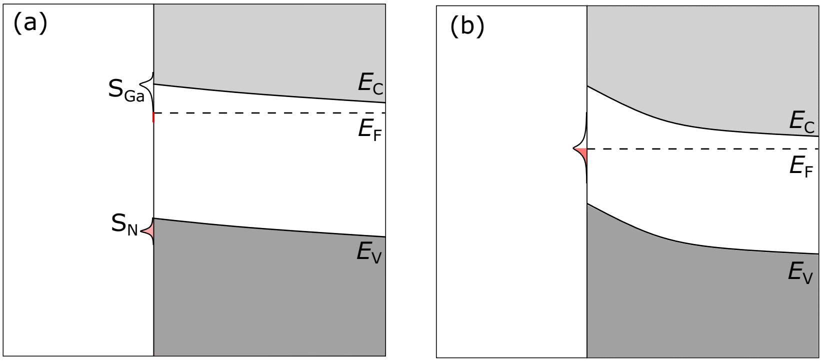

Figure 4.6: Schematic band diagrams of the *pinned* n-type GaN non-polar surface. (a) Pinning by intrinsic surface states: The filled N-derived surface state is situated at the valence band maximum, far off the Fermi level, and is thus electrically inactive. However, the minimum of the empty Ga-derived surface state lies approximately 1 eV below the conduction band minimum within the fundamental band gap. The bulk Fermi level close to the conduction band edge leads to a partial occupation of this otherwise empty state, resulting in an upward shift of the band edges at the surface. (b) Pinning by extrinsic surface states (e.g. step-induced states): Extrinsic surface states commonly lead to a Fermi level pinning in the center of the band gap. In absence of a probe tip, the potential shift at the n-type GaN non-polar surface is expected to be larger for an extrinsic pinning than for an intrinsic pinning.

Interaction of tip and surface state-induced Fermi level pinning

At this stage, we turn to the discussion, first qualitatively, of simultaneous surface state-induced Fermi level pinning and tip-induced band bending, as present in STM. This is followed by simulations of the tunnel current.

1. Model of only intrinsic surface state

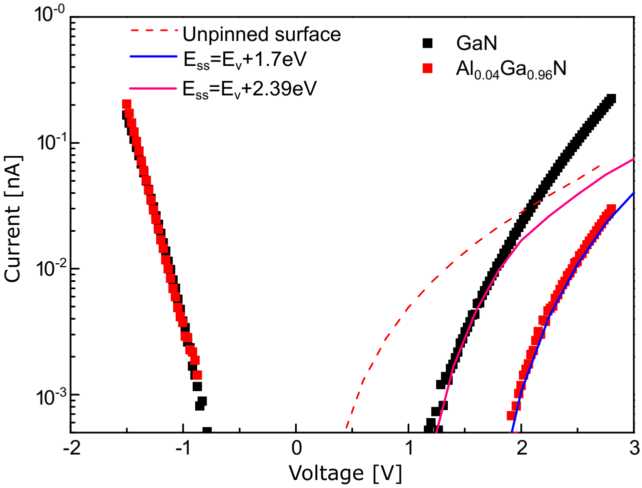

Figure 4.7: Comparison of *I*-*V* spectra measured at non-polar *m* plane GaN and $Al_{0.06}Ga_{0.94}N$ surfaces (symbols) with tunnel current simulations (lines). For GaN, simulations were carried out for both an unpinned (red dashed line) and a pinned (red solid line) surface. However, at positive voltages, tunneling into empty conduction band states starts at about 0.4 V and thus at much smaller voltages than experimentally obtained. This is indicative for an upward band bending, caused by an partial occupation of the Ga-derived surface state. Indeed, the best agreement between the simulated and measured *I*-*V* curves for GaN at positive voltages has been obtained for a pinning of the Fermi energy about 1 eV below the conduction band edge (cf. black symbols and red solid line). In analogy, a pinning of the Fermi energy at 1.69 eV below the conduction band edge has been derived for the $Al_{0.06}Ga_{0.94}N$ surface (cf. red symbols and blue solid line).

The intrinsic surface state is empty in equilibrium. However, by occupation with electrons, the surface state causes a pinning of the Fermi energy, which leads to an offset of the voltage scale. In order to quantify this, Fig. 4.7 displays the simulated tunnel current for the unpinned *n*-doped GaN surface (red dashed line) and the pinned surface (solid lines) with different surface state energies. The experimentally measured spectra of GaN are superimposed as black symbols.

At positive voltages, without surface state, the calculated tunnel current from the tip into the empty conduction band states (red dashed line) starts at a much smaller tunneling voltage than experimentally found. This is in agreement with previous observations.[71] This effect is due to the Fermi level position close to the conduction band edge in n-type GaN. The experimental data suggests rather a larger onset voltage. This can be obtained if the empty surface state creates an voltage (energy) offset by pinning the Fermi energy about 1 eV below the conduction band edge. The simulation of the tunnel current under this assumption (solid red line) agrees very well with the experimentally measured data. Hence, the shift of the current onset to larger positive voltages is given by the energy difference between the intrinsic empty surface state in the band gap and the conduction band edge.[71]

At negative voltages, the situation is somewhat different. If the intrinsic empty surface state would act as pinning state also at negative voltages, the current onset at negative voltages would correspond to the valence band edge. Hence one would measure the real fundamental band gap of 3.4 eV. Instead the apparent band gap is much smaller. This indicates the presence and dominance of a current from electrons accumulating in the conduction band and hence a tip-induced downward band bending. The condition for this scenario is that the empty surface state remains empty under tunneling conditions. Indeed, it has been shown that electrons are prohibited due to momentum conservation to transfer from the conduction band minimum into the empty Ga-derived surface states. This effect reduces the filling probability of the empty surface state in downward band bending condition. In addition, electrons can tunnel easily out of the empty dangling bond if existing. As a result, under tunneling conditions no electron will remain in the empty surface state and hence no Fermi level pinning occurs at negative voltages.

Figure 4.8 illustrates the schematic band diagram of the GaN surface pinned by intrinsic surface states with the tip present.

In analogy, for $Al_{0.06}Ga_{0.94}N$ the empty surface state is located deeper in the band gap as indicated by the larger voltage shift of the onset voltage of the positive current branch. The best agreement is found for a intrinsic empty surface state 1.7 eV below the conduction band edge.

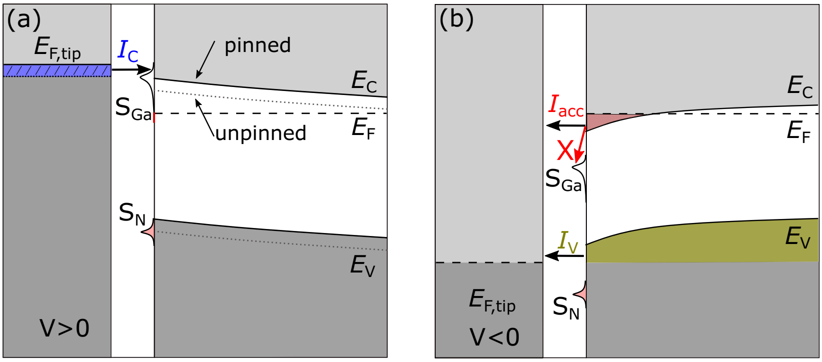

Figure 4.8: Schematic band diagram of a clean nonpolar m-plane GaN surface in presence of a metallic probe tip. (a) At positive voltages, the Fermi level of the tip $E_{\mathrm{F,tip}}$ needs to overcome the conduction band minimum before a tunnel current can emerge. The empty Ga-derived surface state induces a surface Fermi-level pinning that gives rise to a shift of the conduction band minimum towards higher energies compared to the unpinned case (cf. solid versus dotted line). (b) At negative voltages, one would actually expect a pinning by the Ga-derived surface state and thus an upward band bending, too. However, as experimentally shown, the pinning by the Ga-derived surface state cannot be preserved under these conditions. This is due to a quantum mechanically prohibited electron transfer from the conduction band minimum into the Ga-derived surface state. Therefore, under tunneling conditions, the probability of emptying this state by electrons tunneling into the tip is higher than the probability of refilling it by conduction band electrons. As a result, no Fermi level pinning occurs and the tip induced band bending drags the conduction band edge below the Fermi level, which leads to an accumulation current.

2. Model of additional step-induced pinning

The STM images of the $Al_{0.06}Ga_{0.94}N$ surface topography (see in Fig. 4.1) reveal a remarkable amount of steps on the $Al_{0.06}Ga_{0.94}N$ cleavage surface. This points to the presence of additional extrinsic surface states on the $Al_{0.06}Ga_{0.94}N$ $(10\bar{1}0)$ surface. Thus, we need to discuss the influence of step-induced extrinsic surface states on the tunnel current.

As shown in Figs. 4.3 and 4.4 the onset of the positive branch of the tunnel current shifts to higher voltages in area with higher step density. This indicates that the steps play a role. However, this effect is only small: For this we turn to the band structure in presence of pinning by extrinsic surface states. Figure 4.9 illustrates the interaction of tip and the extrinsic surface states (i.e. step-induced) induced Fermi level pinning on a GaN surface.

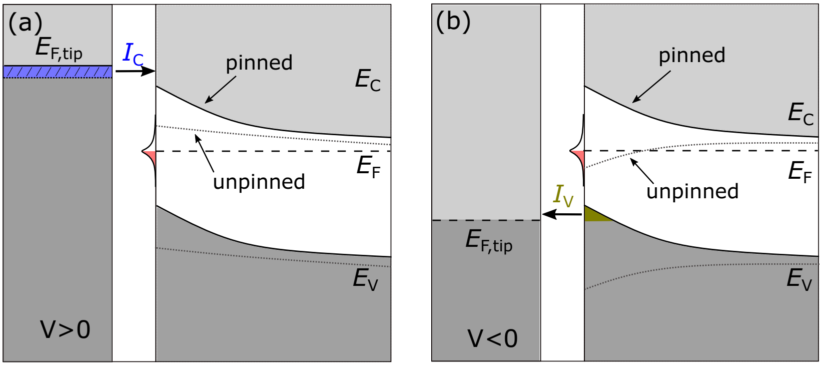

Figure 4.9: Schematic band diagram of a n-type semiconductor pinned by extrinsic surface states in presence of a metallic probe tip. The extrinsic surface state commonly leads to a surface Fermi level pinning at midgap position and thus to an upward band bending. This band bending remains essentially unchanged for both, (a) positive and (b) negative voltages and the tip induced band bending (dotted lines) is suppressed. Thus, the real fundamental band gap can be probed.

At positive voltages, similar to the intrinsic surface state case, the Fermi level is pinned by the extrinsic surface state and the onset voltage is shifted towards a larger value. However, due to a lower energy position of extrinsic surface state (usually at the midgap), the shift of the onset voltage is expected to be much larger than the intrinsic-pinning case.

At negative voltages, the band edges are fixed by the extrinsic surface state. Thus, there is no accumulation current from the conduction band. The tunneling process starts until the Fermi level of the tip is below the valence band edge of the sample.

Hence, one can measure the real fundamental band gap of $Al_{0.06}Ga_{0.94}N$ (3.5 eV) in this case. In addition, the onset voltage of positive and negative branches should exhibit similar values due to the midgap pinning. However, the measured apparent band gap of $Al_{0.06}Ga_{0.94}N$ is 2.7 eV and the onset voltage of the negative branch is much smaller than the positive one. Thus, the tunneling on the $Al_{0.06}Ga_{0.94}N$ surface can not be explained by only extrinsic pinning. Hence, the pinning by surface states on the $Al_{0.06}Ga_{0.94}N$ surface is a combination of intrinsic and extrinsic surface states. The high step density induces only a small additional band bending, but the dominating Fermi level pinning is due to the intrinsic surface state.

4.3 STS at interfaces

4.3.1 Experimental results

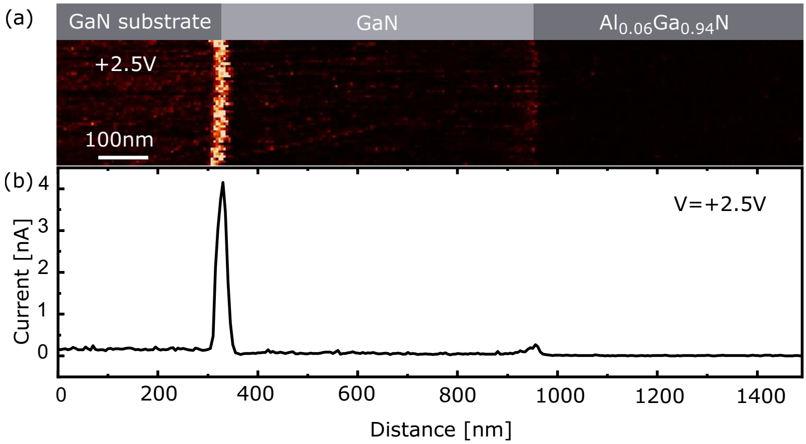

Figure 4.10: (a) Current-imaging-tunneling spectroscopy (CITS) map of the GaN substrate/GaN buffer/$Al_{0.06}Ga_{0.94}N$ layers evaluated at +2.5 V. The two interfaces induce localized current increases. (b) The line profile of the CITS map. At the GaN buffer/GaN substrate interface the tunnel current increases within a ~20 nm (FWHM) region. At the $Al_{0.06}Ga_{0.94}N$/GaN buffer interface, a less pronounced peak can be observed.

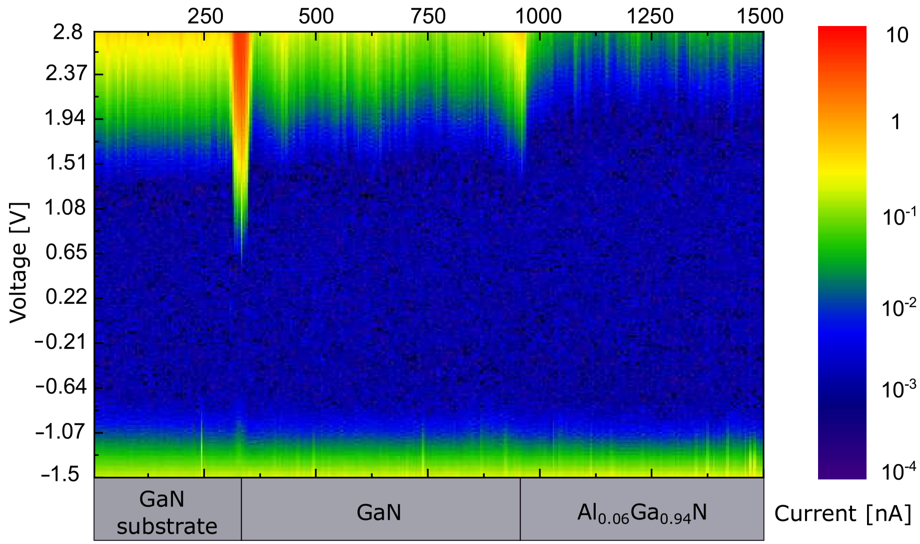

Figure 4.11: Spatial evolution of the tunneling spectra across the $Al_{0.06}Ga_{0.94}N$/GaN buffer/GaN substrate layers. The setpoint is -1.4 V and 80 pA. The *I*-*V* spectra shown in the image are averaged parallel to the interface. At the GaN buffer/GaN substrate interface the onset voltage of the positive tunnel current branch shows a considerable shift towards smaller values within a ∼20 nm (FWHM) region. At the $Al_{0.06}Ga_{0.94}N$/GaN buffer interface, a less pronounced downward shift can be observed.

Figure 4.10 illustrates the local changes at two of the three interfaces (GaN buffer/GaN substrate and $Al_{0.06}Ga_{0.94}N$/GaN buffer interfaces) using a CITS map. The line profile of the CITS map in Fig. 4.10 (b) demonstrates that the interfaces give rise to peaks of the tunnel current with a FWHM of about 20 nm. The increase of the tunnel current by a factor ~ 80 for the GaN buffer/GaN substrate interface is much larger than the increase by a factor of ~ 5 for the $Al_{0.06}Ga_{0.94}N$/GaN buffer interface (values with respect to the GaN buffer). The data illustrates that the local changes of electronic properties are confined at the interfaces and depend strongly on the interface properties.

In order to obtain a deeper insight into the interface properties and origin of the changes at the interfaces, detailed spectra across the interfaces are extracted from the experimental measurements shown in Fig. 4.11 for each interface. Figure 4.12 displays I-V spectra across the GaN buffer/GaN substrate interface, each averaged within a 20 nm wide region parallel to the interface. Each spectrum shown represents the average of about 200 individual spectra. The spectra reveal a strong decrease of the onset voltage by 0.8 V of the positive current branches at the interface. This corresponds to the strong current increase found in Fig. 4.10. The negative current branches remain essentially unchanged.

In analogy, Fig. 4.13 illustrates I-V spectra across the $Al_{0.06}Ga_{0.94}N$/GaN buffer interface. At the interface, again a downward shift of the onset voltage of the positive current branch occurs. However, the shift is significantly smaller with approximately 0.3 V with respect to the GaN buffer. This is in line with the weaker current change for this interface as compared to the former GaN buffer/GaN substrate interface (Fig. 4.10). In addition, the comparison of the spectra on the $Al_{0.06}Ga_{0.94}N$ and GaN side of the interface corroborates the onset shift between the two materials observed in Fig. 4.4 far away from the interfaces already. The negative current branches are again essentially unchanged.

Figure 4.14 presents I-V spectra across the $In_{0.05}Ga_{0.95}N/Al_{0.06}Ga_{0.94}N$ interface, in analogy to the previous interfaces. The spectra reveal a continuous downward (upward) shift of the onset voltage of the positive (negative) current branch from $Al_{0.06}Ga_{0.94}N$ to $In_{0.05}Ga_{0.95}N$. The final spectrum of $In_{0.05}Ga_{0.95}N$ exhibits only a very small apparent band gap of 0.67 V.

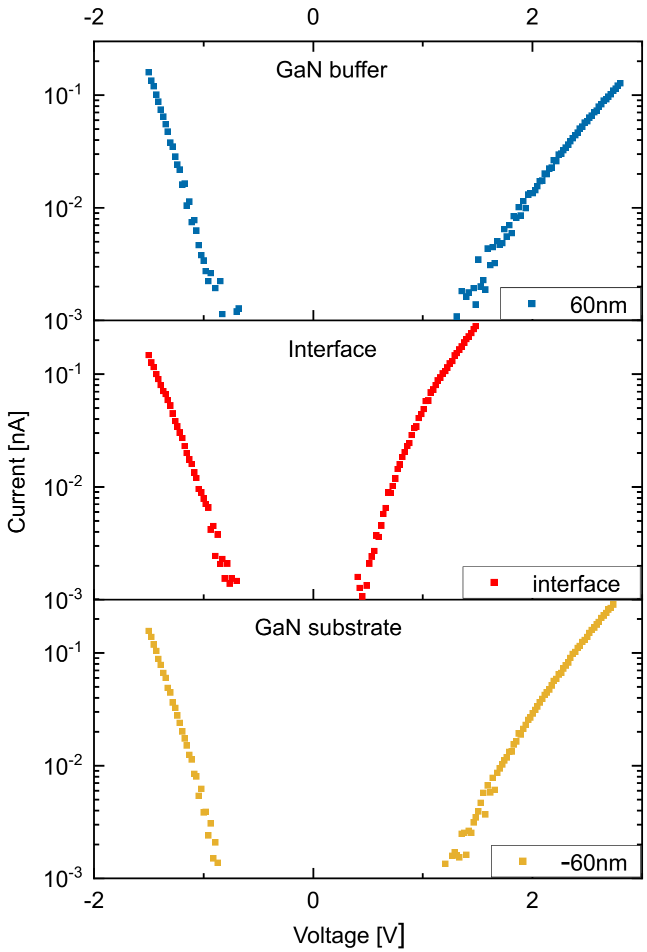

Figure 4.12: *I*-*V* spectra measured across the GaN buffer (blue spectrum)/GaN substrate (yellow) interface (red). The setpoint is -1.4 V and 80 pA. The onset voltage of the positive current branch shifts downwards by 0.8 V at the interface position, which reveals a downward band bending at the interface. Each spectrum has been averaged over a 20 nm wide region parallel to the interface.

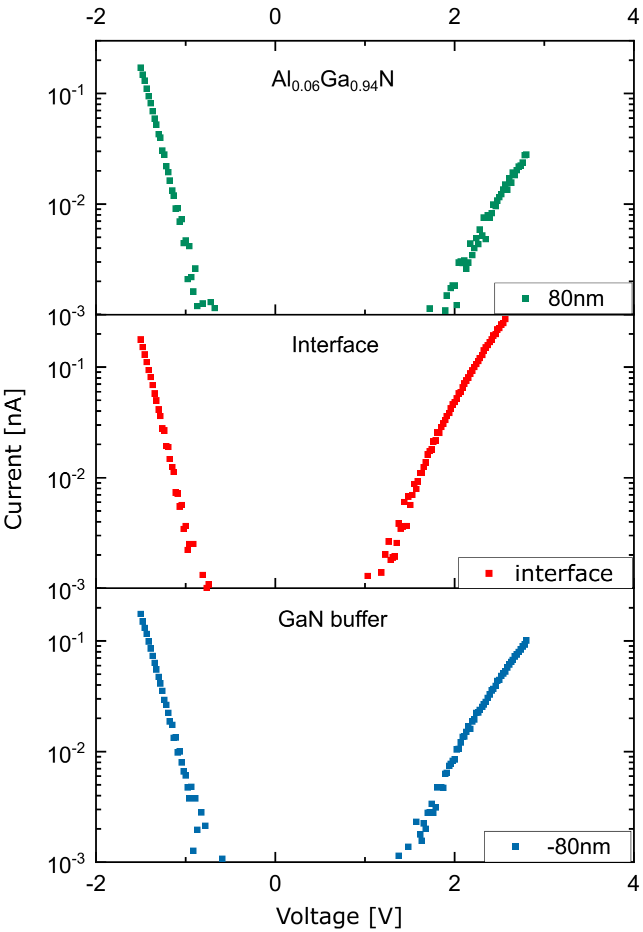

Figure 4.13: *I*-*V* spectra measured across the $Al_{0.06}Ga_{0.94}N$ (green)/GaN buffer (blue) interface (red). The setpoint is -1.4 V and 80 pA. Again the onset voltage of the positive current branch shifts downward at the interface, similar to the GaN buffer/GaN substrate interface. Each spectrum has been averaged over a 10 nm wide region parallel to the interface.

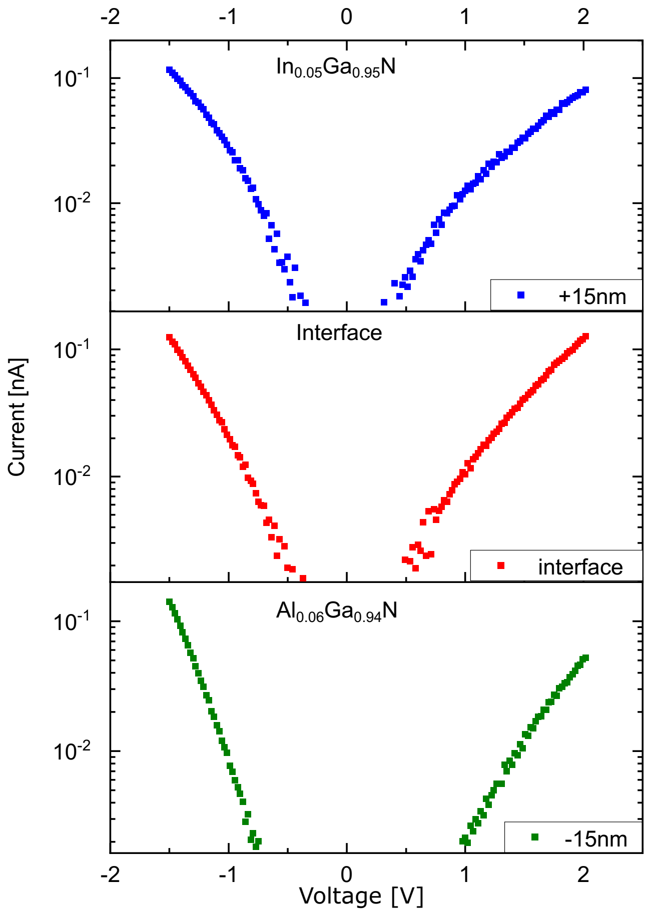

Figure 4.14: *I*-*V* spectra measured across the $In_{0.05}Ga_{0.95}N/Al_{0.06}Ga_{0.94}N$ interface. The setpoint is -1.4 V and 80 pA. Each spectrum has been averaged over a 15 nm wide region parallel to the interface. The onset voltage of the positive tunnel current branch shifts towards smaller values from $Al_{0.06}Ga_{0.94}N$ to $In_{0.05}Ga_{0.95}N$.

4.3.2 Discussion of tunneling spectra at interfaces

The tunneling spectra at the interface shown in Figs. 4.12, 4.13, and 4.14 reveal shifts of the positive voltage branch towards smaller voltages at the interfaces, which indicates a reduction of the tip-induced upward band bending at positive voltages. This can be caused by an additional downward electrostatic potential change.

The electrostatic potential change can be induced by a charge at the interface, e.g. impurities. This make sense for the GaN buffer/GaN substrate interface, due to the presence of a highly Si-doped layer at the interface found in the SIMS data in Fig. 3.3. However, for the other two interfaces, the doping concentrations at the interface are close to those of the adjacent layers.

Hence, for the $Al_{0.06}Ga_{0.94}N$/GaN interface the downward shift of the positive onset voltage suggests a local downward band bending whose origin is not related to impurity charges. Similar the continues downward shift at the $In_{0.05}Ga_{0.95}N/Al_{0.06}Ga_{0.94}N$ interface suggests a downward band bending.

However these effect cannot be discriminated from local polarization changes, electron affinity changes, or changes of the band structure. Thus, in order to obtain a comprehensive knowledge about the electrostatic potential change at the interface, we need to combine the STS data with other local electrostatic potential measurements, i.e. with electron holography in a TEM (see Chapter 5).

4.4 Conclusions

This chapter presents the topography and tunneling spectroscopy of the cross-sectionally cleaved $In_{0.05}Ga_{0.95}N/Al_{0.06}Ga_{0.94}N$/GaN heterostructure probed by STM and STS.

The topography of the m plane cleavage surface is dominated by cleavage steps separating atomically flat terraces. The orientation of the steps is mostly parallel to the c direction except in the $Al_{0.06}Ga_{0.94}N$ layer, where the steps exhibit a bending toward a direction coupled with a significant increase in their density. The step pattern is compatible with a strained $Al_{0.06}Ga_{0.94}N$ layer.

The tunneling spectra of the binary and ternary group III-nitride layers reveal a pinning of the Fermi level by the intrinsic group III atom-derived dangling bond. Surface steps induce slight further upward band bending. At the interfaces the tunneling spectra reveal a significant downward shift of the onset of the tunnel current at positive voltages (while at negative voltages no changes occur). This suggests a local downward band bending, whose origin is traced to a delta type doping profile at the GaN buffer/GaN substrate interface. For the other interfaces the conclusions are not that straightforward. Hence for a further insight, it is necessary to combine with the STS data the off-axis electron holography in the TEM, which provides a complimentary access to the local electrostatic potential.

Chapter 5

Quantitative determination of electrical properties of semiconductor interfaces by off-axis electron holography

In this chapter, the phase changes of transmitted electrons in TEM at group III-nitride semiconductors' interfaces are measured by off-axis electron holography. For this purpose the specimens are investigated by off-axis electron holography at 300 kV in an image-aberration-corrected FEI Titan G2 60-300 HOLO microscope, equipped with a high-brightness field emission gun (XFEG) and two electrostatic biprisms.[75] 300 nm thick lamellas are prepared by FIB milling in a FEI Helios Nanolab 400s dual-beam system with Ga ions as described in detail in Chapter 2. Since the electrostatic potential at the surface of the lamellas is affected by the FIB preparation and surface contaminations, a quantitative understanding of the electron phase obtained by off-axis electron holography requires a determination of the surface Fermi level pinning and a self-consistent simulation of the electrostatic potential, using all relevant properties acquired by STS and SIMS in the previous chapters. Due to no material change at the GaN buffer/GaN substrate homointerface, we first fit the phase profile of this interface to determine the surface Fermi level pinning. This enables the simulation of the other, more complex heterointerfaces, and thus the unraveling their properties.

5.1 Experimental results

Figure 5.1(b) shows the reconstructed phase image of a part of the $In_{0.05}Ga_{0.95}N$/ $Al_{0.06}Ga_{0.94}N$/GaN buffer/GaN substrate heterostructure. Within the field of view, two interfaces are present and can be discerned from changes in contrast (indicated by red dashed lines): a bright line is visible at the GaN buffer/GaN substrate interface and a step-like contrast is observed at the $Al_{0.06}Ga_{0.94}N$/GaN interface.

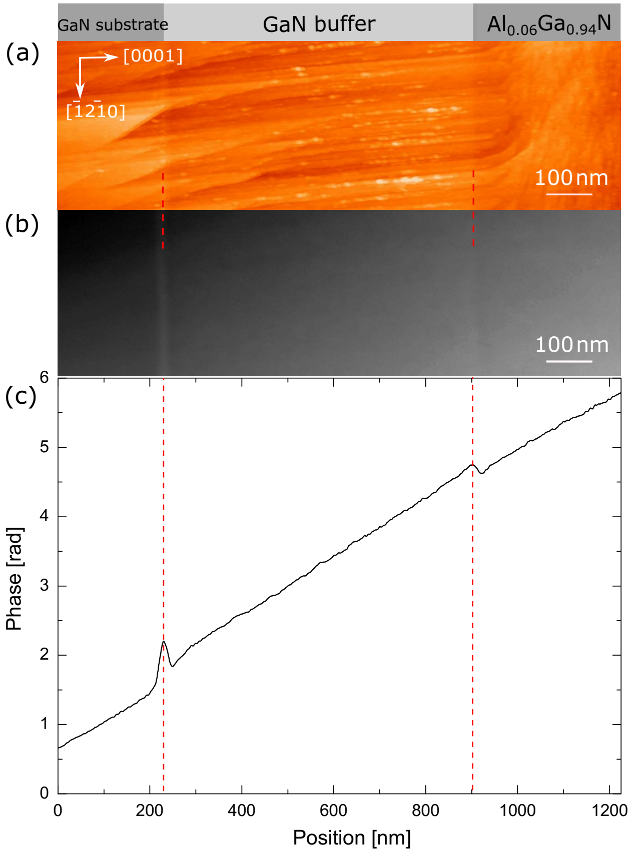

Figure 5.1: (a) Cross-sectional constant-current STM image of the $Al_{0.06}Ga_{0.94}N$/GaN buffer/GaN substrate heterostructure measured at -2.5 V and 80 pA. (b) Reconstructed phase image of the $Al_{0.06}Ga_{0.94}N$/GaN buffer/GaN substrate heterostructure. Two interfaces are present in the field of view and give rise to bright lines. (c) Line profile extracted from the phase image perpendicular to the interfaces. The background of the phase profile is linearly increasing from the GaN substrate to the $Al_{0.06}Ga_{0.94}N$ layer. At the GaN buffer/GaN substrate interface, the phase change shows a peak, whereas a step-like change is observed at the $Al_{0.06}Ga_{0.94}N$/GaN buffer interface.

The line profile of the phase change in Fig. 5.1(c), extracted from the phase image in Fig. 5.1(b), reveals a linear background on top of which a pronounced peak appears at the GaN buffer/GaN substrate interface, whereas at the $Al_{0.06}Ga_{0.94}N$/GaN interface the phase change exhibits an offset. Before further analysis a linear background subtraction is applied to the phase profile. In addition for noise reduction several measurements are averaged. For averaging only profiles without diffraction artifacts were used.

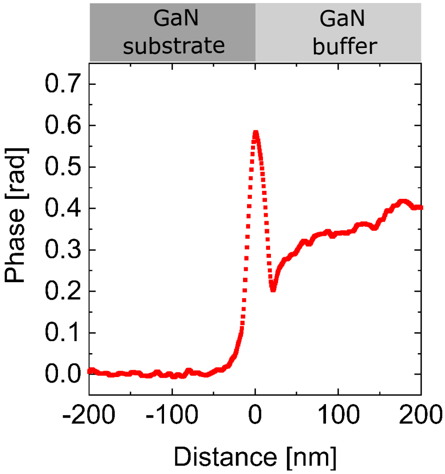

Figure 5.2: Averaged phase profile across the GaN buffer/GaN substrate interface. The peak at the interface position has a FWHM of 20 nm and a height of 0.4 rad relative to the GaN buffer. Right to the peak, a pronounced dip in the phase profile becomes apparent at the GaN buffer side before reaching the constant plateau.

Figures 5.2 and 5.3 illustrate the averaged local phase changes at the GaN buffer/GaN substrate and $Al_{0.06}Ga_{0.94}N$/GaN interfaces, respectively, after removing the linear background. Now further details of the phase change at the interfaces can be observed. Beside the already mentioned peak in the phase profile, the GaN buffer/GaN substrate interface gives rise to a dip at GaN buffer side. The peak has a FWHM of ~20 nm and a height of 0.4 rad. In contrast, the $Al_{0.06}Ga_{0.94}N$/GaN interface induces a step-like phase change of 0.17 rad, without peaks or dips.

Figure 5.4 illustrates the averaged phase profile across the $In_{0.05}Ga_{0.95}N$/$Al_{0.06}Ga_{0.94}N$ interface (not in the field of view of Fig. 5.1). Unlike the other two interfaces, a combination of a step-like change and a pronounced dip is found here. The dip exhibits a height of 0.25 rad and the offset between two plateaus is around 0.15 rad.

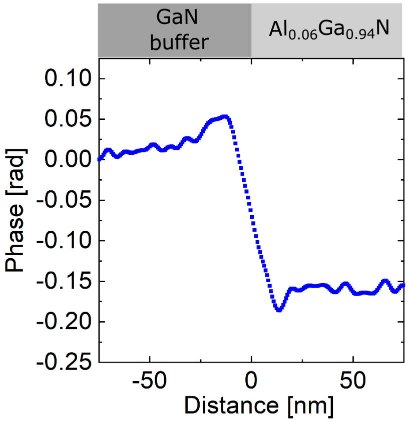

Figure 5.3: Averaged phase profile across the GaN/$Al_{0.06}Ga_{0.94}N$ interface. A step-like phase shift of ~0.17 rad is visible at this interface, decreasing from GaN to $Al_{0.06}Ga_{0.94}N$.

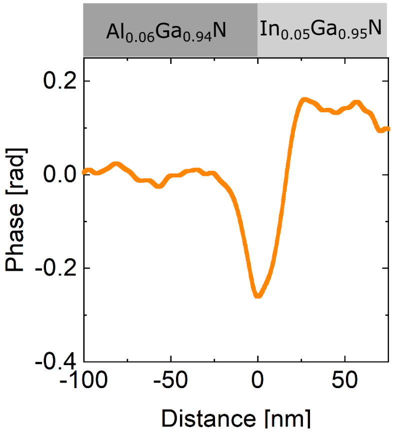

Figure 5.4: Averaged phase profile across the $In_{0.05}Ga_{0.95}N$/$Al_{0.06}Ga_{0.94}N$ interface. The phase profile exhibits a pronounced dip (0.25 rad) at the interface and an offset (0.15 rad) between two layers. The phase change increases from $Al_{0.06}Ga_{0.94}N$ to $In_{0.05}Ga_{0.95}N$.

5.2 Discussion

5.2.1 Comparison of holography with SIMS and STM

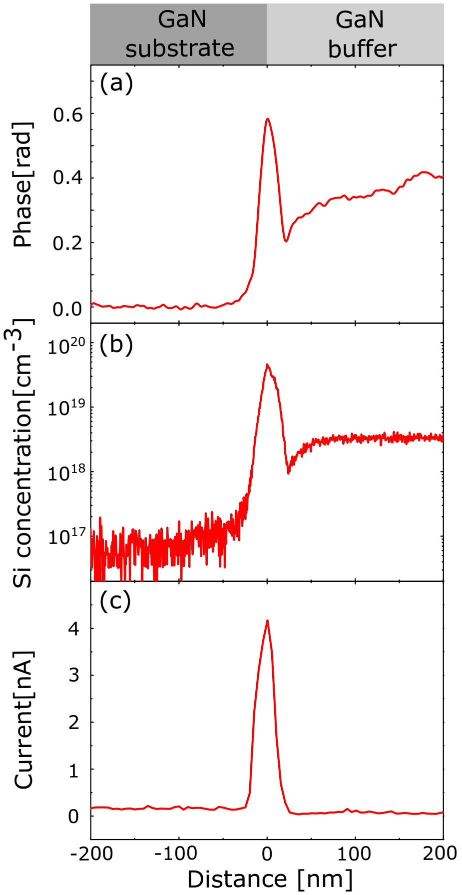

Figure 5.5: Comparison of the phase profile across the GaN buffer/GaN substrate interface with the Si concentration profile measured by SIMS and the current profile derived from the CITS map. All these profiles show a peak with a FWHM around 20 nm at the interface. Strong similarities can be observed in the phase profile and the Si concentration profile, i.e. the relative height in the layers and a decrease next to the peak before reaching a constant level.

The STM image in Fig. 5.1(a) reveals already a similarity of the interface contrast in STM and phase images. For a more detailed comparison, Fig. 5.5 depicts (a) the phase profile across the GaN buffer/GaN substrate interface measured by electron holography, (b) the Si concentration obtained by SIMS, and (c) a line profile extracted from the CITS map evaluated at +2.5 V measured by STM. All those profiles have in common a peak at the interface with a FWHM of about 20 nm. Interestingly the phase profile and the profile of the Si concentration exhibit a very similar shape, indicating that the peak and the subsequent dip in the phase profile is primarily caused by a change in doping concentration.

In the notation used throughout this thesis, a minimum of the electrostatic potential gives rise to a maximum in the electrons' phase. Hence, the maximum of the phase at the GaN buffer/GaN substrate interface corroborates the findings obtained by STS, that the electrostatic potential is decreased locally by a highly doped layer. Thus, qualitatively, the phase change at the GaN buffer/GaN substrate interface can be explained by the doping profile obtained by SIMS. However, if we turn to a quantitative analysis of the phase change, the situation becomes more complex. This can be easily understood, if one estimates the total phase change, caused by a change of the doping concentration from $1{\times}10^{18}$ to $1{\times}10^{19}\,\mathrm{cm}^{-3}$. Assuming an effective density of states mass of the conduction band of 0.2,[76] the Fermi level is increased by $\sim$37 meV due to the doping concentration change. According to Eq. 2.22, this would lead to an phase change of $\phi = C_{\mathrm{E}} {\cdot} 0.037\,\mathrm{V} {\cdot} 3 {\cdot} 10^{-7}\mathrm{m}{=}73\,\mathrm{mrad}$ for a specimen thickness of 300 nm. Obviously, the peak of the electrons' phase in Fig. 5.5(a) is significantly larger than the estimated value. Thus, further contributions to the phase change need to be discussed.

5.2.2 Theoretical discussion of electron holography

According to Eq. 2.22 in Section 2.3.2, the phase shift of the electron is given by the integral of the potential along the beam direction. Therefore the phase shift depends primarily on the following physical properties: mean inner potential (MIP), electrostatic potential and thickness of the lamella.

- MIP: V_{MIP} is related to the intrinsic materials properties.[77] Since from the GaN buffer to the GaN substrate, there is no material change, V_{MIP} does not change either. Hence, only for interfaces that exhibit composition changes, V_{MIP} affects the phase change. Thus, V_{MIP} only plays a role at the other two interfaces.

- Electrostatic potential: The electrostatic potential V_{EP} is related to the concentration of both fixed and free charges, governed by the Poisson equation. Thus it is affected by the doping concentrations, defects, and surface charges. Since the lamella is prepared by FIB milling, its surfaces can be damaged by high energy ion beams. Thereby, extrinsic surface states may have been incorporated by preparation process, leading to a surface Fermi level pinning. The screening length of the surface Fermi level pinning depends on the doping concentration of the different layers. Thus, self-consistent simulations need to be performed to reveal the electrostatic potential distribution within the lamella.

- Thickness changes: The phase in electron holography depends linearly on the thickness of the lamella along the electron beam direction. The preparation of lamellas by FIB could introduce some fluctuations in thickness. However, since the ion beam of the FIB is applied perpendicular to the interfaces (see Fig. 3.7), thickness changes introduced by the FIB do not affect the averaged line profiles of the phase across the interfaces. Hence, the thickness is assumed to be constant.

In addition to the intrinsic properties of materials and the thickness change, that lead to a phase change, there are some other effects related to the measurement method. In particular, beam-induced electron-hole pair generation and beam induced charging could play a role.

- Beam-induced electron-hole pair generation: Since the doping concentrations of the sample are in the order of $10^{18}\,\mathrm{cm}^{-3}$ or even $10^{19}\,\mathrm{cm}^{-3}$, the concentration of the beam-induced electron-hole pairs, which is found to be in the order of $10^{17}\,\mathrm{cm}^{-3}$ for the actual measurement parameters, is approximately one order of magnitude lower than the doping concentration.[78] Therefore, the effect of beam-induced carriers on the phase change is negligible for the samples investigated here.

- Beam-induced charging: The linear background of the phase profile is attributed to a charging. This could be related to a Au layer on the (0001) growth surface. The Au layer forms a Schottky contact with the semiconductor. Thus, it can be positively charged by the electron beam and the charges cannot flow away fast enough. However, such long range effects on the phase change can be easily separated from the local changes near the interfaces by subtracting the background. Hence, the influence of beam-induced charging can be also neglected.

In conclusion, for the here discussed doping and heterointerfaces, electrostatic potential changes and the MIP changes between different materials are the primary effects to the phase change of transmitted electrons in electron holography. Hence, if the MIP and the electrostatic potential, as well as the thickness are known, we can calculate the phase change using these three values. The derivation of the MIP values is described in Section 6.2. The thickness determination is given in Section 3.3.

5.2.3 Comparison with self-consistent simulations

We now turn to a quantitative analysis of the phase change. For achieving this goal, we performed self-consistent simulations of the GaN buffer/GaN substrate interface including the doping profile as revealed by SIMS. The results are compared to the measured phase change. The line of analysis is as follows: The GaN buffer/GaN substrate interface is a pure doping interface where all parameters are known and thus the electrostatic potential and hence phase change can be calculated. The only unknown parameter is the surface pinning. Therefore, the GaN buffer/GaN substrate interface is used to extract the surface pinning with help of the simulations. The extracted surface pinning is then applied to the two heterointerfaces to extract polarization and electron affinity changes.

GaN buffer/GaN substrate interface

Since the GaN buffer/GaN substrate interface is a homointerface, contributions to the phase change across the interface caused by a change of material properties like MIP, electron affinity, or polarization can be ruled out. However, as discussed in Section 5.2.1, a doping-induced change of the Fermi level alone is insufficient to explain the experimentally observed phase change. Thus, we investigated the interplay of different surface pinning levels, caused by FIB induced damage, with the different doping concentrations measured by SIMS.

Figure 5.6 illustrates the self-consistent calculation of the phase change for different surface state pinning levels (colored lines) as well as the measured phase profile across the GaN buffer/GaN substrate interface (gray symbols).

First, we discuss the situation of an unpinned ideal surface (blue dashed line): The calculated electrostatic potential without pinning by surface states exhibits only a small phase change (as estimated in Section 5.2.1), which does not fit to our measurement, although the overall shape of the measurement is reproduced. Without

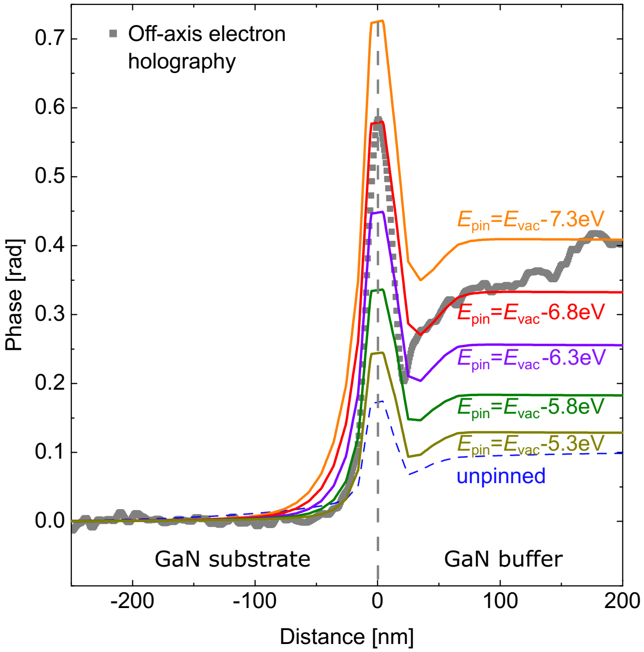

Figure 5.6: Calculated phase profiles (lines) across the GaN substrate/ GaN buffer interface, including different surface pinning conditions. The measured electron phase profile is shown in gray symbols to compare with the simulations. The best agreement between the calculated and experimentally measured phase profile is obtained for a surface pinning level at $E_{\mathrm{VAC}} - (6.8 \pm 0.2)\,\mathrm{eV}$, which equals to $E_{\mathrm{V}} + (0.69 \pm 0.2)\,\mathrm{eV}$.

surface pinning, the phase change is due to the different Fermi level positions across the interface only, which are caused by the doping profile. The disagreement of this model with the measurement indicates that the lamella's surface can not be free of surface states in the fundamental band gap (i.e. unpinned).

Thus, we introduce a surface Fermi level pinning into the calculation. Since GaN is present on both sides of the interface, we assume the pinning levels to be everywhere identical. The solid lines in Fig. 5.6 are calculated phase profiles for a series of different surface pinning levels. The peak height and relative height of two plateaus notably increase with a decrease of the pinning level (shift of pinning level toward valence band edge). The physical origin of this effect is discussed in Section 5.2.4. The best agreement between experiment and simulation is found for a surface pinning level at $E_{\mathrm{VAC}} - (6.8 \pm 0.2)\,\mathrm{eV}$, i.e. $E_{\mathrm{V}} + (0.69 \pm 0.2)\,\mathrm{eV}$, where E_{VAC} is the vacuum energy. The quantitative agreement between simulation and measurement is indicative for the presence of a surface Fermi level pinning.

The origin of the surface Fermi level pinning

In order to discuss the origin of the surface Fermi level pinning of the lamella, the lamella preparation process needs to be taken into account. After ion beam preparation in the FIB vacuum chamber, the lamella was taken out to the ambient air and transferred to a vacuum desiccator until the beginning of the TEM measurement. Although the transferring time is short, it is still possible to introduce an adsorbate coverage (typically oxygen) on the surfaces of the lamella.[79] Thus, adsorbates are expected to create midgap surface states. However, the measured peak height does not fit to the calculation for the midgap state (see the green line in Fig. 5.6) and this effect is likely secondary. The reason is that the FIB creates an amorphous surface layer, which can be anticipated to create a pinning too. In addition, below the amorphous top layer, the Ga ion beam used for FIB milling can be expected to induce point defects, such as N vacancies (V_N), N interstitials (N_i), Ga vacancies (V_{Ga}) and Ga interstitials (Ga_i). The defects concentrate at the near surface region. Since N is easier to be displaced by ion-bombardment defects (much lighter than Ga), most defects can be expected to be related to the displacement of N atom (i.e. V_N and N_i). Furthermore, the diffusion energies of the different defects are remarkably different:[80, 81] Utilizing first-principles density-functional theory (DFT), Limpijumnong *et al.*[80] found that among all types of vacancies present in GaN, V_N have the highest migration barrier (see Tab. 5.1). Hence, the V_N are expected to remain at the near surface region of the lamella, whereas interstitial atoms can migrate to the surface (i.e. incorporate in the amorphous surface layer) even at room temperature.

Deffects	Migration barriers [eV]
V_N^+	4.3
V_N^{3+}	2.6
V_{Ga}^{3-}	1.9
N_i^+	2.1
Ga_i^{3+}	0.9

Table 5.1: The migration barriers for native defects in wurtzite GaN. The highest one is that of V_N^+ with 4.3 eV.[80]

At this stage, the electronic properties of V_N need to be discussed. DFT calculations revealed that V_N exhibits two charge transition levels in the fundamental band gap.[82, 83] The (3+/+) transition level is located at 0.47 eV above the valence band, and the (+/0) transition level is 0.24 eV below the conduction band. Due to the presence of the amorphous layer and the adsorbate coverage on the surface of the lamella, the surface is at least pinned at midgap. It indicates that the transition levels close to conduction band are electrically inactive. Thus, the (3+/+) transition level of V_N, which is found at E_V+0.47 eV, is the first level that could cause a surface pinning in our lamella. This value agrees well with the pinning level of $E_V + (0.69 \pm 0.2)\,\mathrm{eV}$ extracted from the phase profile.

Since the surface treatment is identical for each layer of our lamella, the surface pinning levels with respect to the vacuum level are expected to be identical for each layer. The thus obtained pinning level will be therefore used in the following for the analysis of all other interfaces.

$Al_{0.06}Ga_{0.94}N$/GaN interface

The $Al_{0.06}Ga_{0.94}N$/GaN interface gives a step-like change of the phase. The two different plateaus, separated by the step, extend over the whole adjacent layers. If there would be an electronic effect (e.g. charge sheet, polarization change) locally confined at the interface, the free charge carriers would screen it and as a result the phase change would reflect this screening. However, only a step in the phase is found without decay on either side. Hence one can rule out polarization changes at the interface as origin of the step-like phase change (the polarization change induces a local change in the phase shift, see discussion in Section 5.2.4). However, a material contrast arising from a change of the MIP, can be expected to result in a sharp step in the phase profile across the interface (see Section 5.2.4). Similarly, an electron affinity change can also lead to a step-like phase shift without the effect of screening within the adjacent layers (see Section 5.2.4). Both, a change of the MIP and an electron affinity change can thus contribute to the measured phase shift at this interface. With the theoretical value of the MIP change at the $Al_{0.06}Ga_{0.94}N$/GaN interface ($\Delta V_{\mathrm{MIP}} = 105 \pm 32\,\mathrm{mV}$, derived in Section 6.2), the electron affinity change across the interface can be determined by fitting the simulated phase change to the measurement.

Figure 5.7 illustrates the self-consistent calculations (colored dashed and solid lines) of the phase profile together with the measured signal (symbols) across the $Al_{0.06}Ga_{0.94}N$/GaN interface. Since the lamella was tilted from the zone axis (tilt

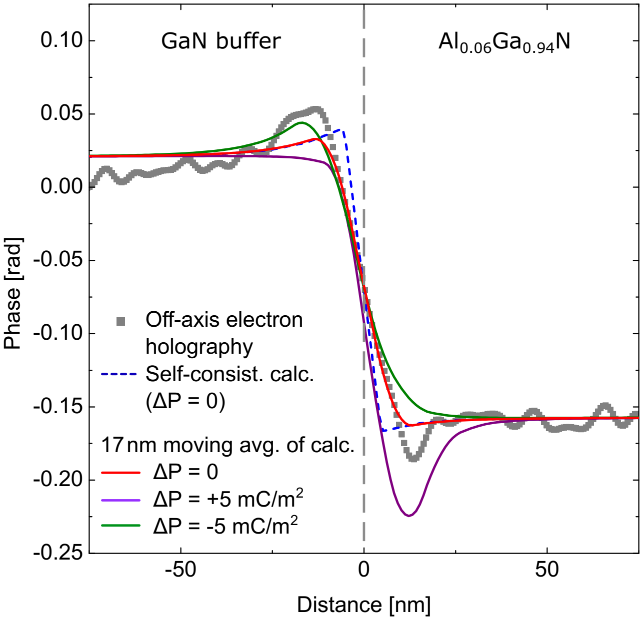

Figure 5.7: Simulated phase change across the $Al_{0.06}Ga_{0.94}N/GaN$ interface (lines) and experimental phase profile (gray symbols) measured by off-axis electron holography. The step-like change in the phase profile can be attributed to an electron affinity change and a MIP change. The self-consistent calculation of the phase change is in best agreement with the measured phase change for $\Delta\chi = +42.5 \pm 50\,\text{meV}$ and $\Delta V_{\text{MIP}} = 105 \pm 32\,\text{mV}$ (red solid line). We applied a 17 nm moving average to the simulated phase profile due to a tilt of the sample (see text). The blue dashed line is the simulated result without moving average. Furthermore, two calculations with a polarization change of $\Delta P = \pm 5\,\text{mC/m}^2$ are performed (green and purple solid lines). However, they can not reproduce the shape of measured phase around the interface, indicating no relevant polarization change at this interface. Note, the surface pinning level is identical to the one used for the GaN substrate/ GaN buffer interface.

angles 13° and 1° in *a* and *c* directions, respectively) to reduce the diffraction contrast, we applied a 17 nm moving average to the calculated phase profile. The best agreement with the measured phase profile is achieved for $\Delta\chi = +42.5 \pm 50\,\mathrm{meV}$ (red solid line) and no polarization change. In order to demonstrate that there is no detectable polarization change at this interface, we added to the graph in Fig. 5.7 two simulated phase changes assuming a rather small polarization change of $\Delta P = \pm 5\mathrm{mC/m^2}$ (green and purple solid lines). Clearly, the assumption of a polarization change at the interface completely alters the symmetry of the two opposite peaks at the interface region. This has not been observed in the experiment. Hence, we anticipate a polarization change of $\Delta P = 0 \pm 2\,\mathrm{mC/m^2}$ is achieved for the $Al_{0.06}Ga_{0.94}N$/GaN interface.

Note, for the self-consistent simulations of this interface we used the same surface Fermi level pinning as for the GaN buffer/GaN substrate interface, as discussed before.

$\mathbf{In_{0.05}Ga_{0.95}N/Al_{0.06}Ga_{0.94}N}$ interface

The phase profile across the $In_{0.05}Ga_{0.95}N/Al_{0.06}Ga_{0.94}N$ interface, shown as gray symbols in Fig. 5.8, shows a pronounced depression in addition to a step-like behavior at the interface. This asymmetric shape near the interface indicates a localized maximum of electrostatic potential, which can arise from a delta doped structure or negative bound sheet charge. According to the doping profile obtained by SIMS, no significant doping concentration changes occurs at this interface that could explain the observed depression of the phase. Thus, a bound sheet charge can be expected to be present at the interface. Bound sheet charges can be induced by interface states or a polarization discontinuity at the interface. Since no interface dislocations and defects have been detected by TEM in our sample, the depression in the phase profile can not be attributed to interface gap states. Therefore, the depression in the phase profile is indicative for a polarization change induced bound sheet charge at the interface.

In order to obtain the electron affinity change of this interface, we first fitted the plateaus-heights (i.e. step-heights) on both sides of the interface, in analogy to the $Al_{0.06}Ga_{0.94}N$/GaN interface. The best fit was obtained for an electron affinity change of $\Delta\chi = +170 \pm 50\,\mathrm{meV}$ (using a MIP change of $\Delta V_{\mathrm{MIP}} = 281 \pm 40\,\mathrm{mV}$ derived in Section 6.2) (green solid line in Fig. 5.8). On this basis, a polarization change is taken into account and the best agreement is obtained for $\Delta P = +9.7 \pm 2.0\,\mathrm{mC/m^2}$ at the $In_{0.05}Ga_{0.95}N/Al_{0.06}Ga_{0.94}N$ interface (cf. red solid line in Fig.

5.8). Note, the surface pinning level as well as the moving average, applied to the simulated phase profiles, is same as before.

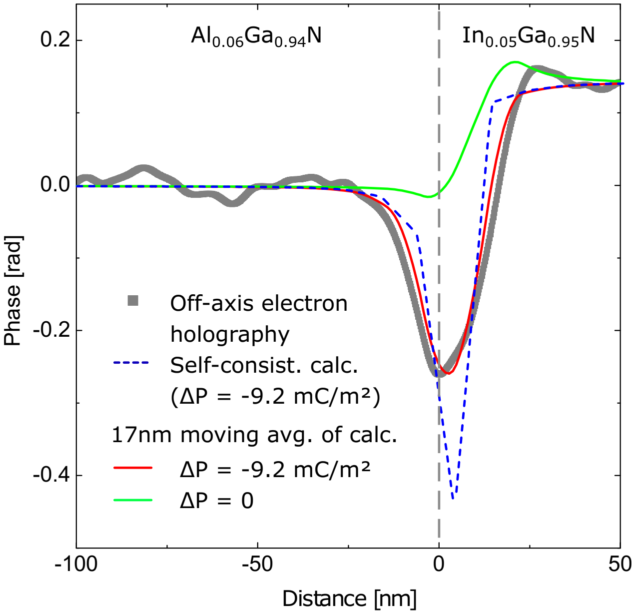

Figure 5.8: Simulated phase change across the In$_{0.05}$Ga$_{0.95}$N/Al$_{0.06}$Ga$_{0.94}$N interface (colored lines) and experimental phase profile (gray symbols) measured by off-axis electron holography. The phase profile exhibits not only a step-function like behavior but also a pronounced depression at the interface. The step-like feature can be attributed to an electron affinity change $\Delta\chi = +170 \pm 50\,\mathrm{meV}$ and a MIP change $\Delta V_{\mathrm{MIP}} = 281 \pm 40\,\mathrm{mV}$ (green solid line). The pronounced depression reveals a polarization change induced by a bound sheet charge at the interface. The best agreement is calculated for a polarization change of $\Delta P = +9.7 \pm 2.0\,\mathrm{mC/m^2}$ with applying a 17 nm moving average (red solid line). The calculation without moving average is shown in blue dashed line for comparison. The surface pinning level is the same for the other interfaces.

5.2.4 Discussion of the effect of surface Femi-level pinning, electron affinity change, MIP change, and polarization change on the phase shift

Surface Fermi level pinning

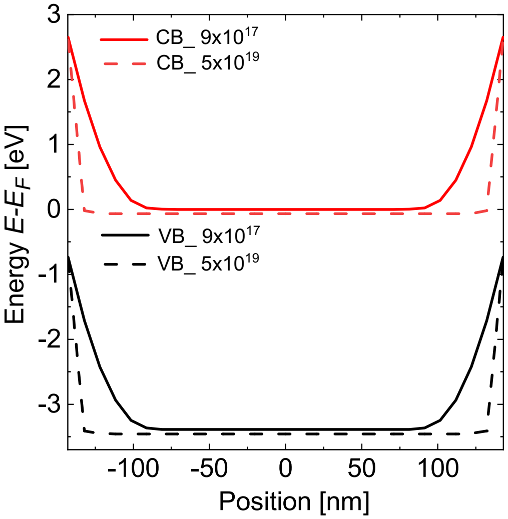

Figure 5.9: Calculated band edge positions with surface pinning for doping concentrations of $9\times10^{17}\,\mathrm{cm}^{-3}$ (solid line) versus $5\times10^{19}\,\mathrm{cm}^{-3}$ (dashed line). The doping levels correspond to the Si concentration of the GaN substrate and the GaN buffer/GaN substrate interface. The screening length significantly changes with the doping concentration, and thus effects the average electrostatic potential which governs the phase change of the transmitted electrons in TEM. This effect increases the average electrostatic potential differences between differently doped layers, and thereby increases the phase change between differently doped layers.

The presence of the surface Fermi level pinning induces a remarkable change in the phase shift, as shown in Fig. 5.6. The physical origin of this needs to be discussed. If a lamella's surface is pinned by surface states, a potential gradient is present inside the lamella at the near surface region due to screening by free charge carries. The screening length is determined by the concentration of free carriers and thus by the doping concentration. This potential gradient is responsible for the increased phase change at the GaN buffer/GaN substrate interface compared to the unpinned case.

This is illustrated by Fig. 5.9 which shows the potential gradients inside the lamella for the cases of a rather high and a moderate doping concentration. For each doping concentration, the conduction band edge is shown in red and the valence band edge is shown in black. The solid line corresponds to a lower doping concentration of $9\times10^{17}\,\mathrm{cm}^{-3}$ (GaN substrate), and the dashed line corresponds to a concentration $5\times10^{19}\,\mathrm{cm}^{-3}$ (the GaN buffer/GaN substrate interface).

Since the surface pinning level is identical for each layer, we assume that the potential gradients in the vacuum are same for every layer. Therefore, the influence of the potential gradients in the vacuum region on the phase profiles across the interfaces can be neglected here and only the potential gradients within the lamella need to be considered.

The phase is now proportional to the average electrostatic potential through the whole lamella. The average potential is decreased by the screening areas of the surface pinning. This decrease is larger for higher doping concentrations. Hence the phase contrast between two doping levels increases as compared to the pure bulk doping effect giving only slightly different band edge positions (see band edge positions in the center of the lamella in Fig. 5.9).

MIP, electron affinity and polarization changes

For heterointerfaces, the different materials may lead to changes of MIP, electron affinities and polarization. All of these changes are expected to contribute to phase shifts of transmitted electrons. In order to obtain a deeper insight of the effects on the phase shift, we study the listed effects separately to explain their influence on the phase shift.

Figure 5.10 shows the simulated phase profile across an interface which has only a MIP change (a) and only an electron affinity change (b) with a surface state pinning, respectively. Both translate into an offset at the interface. However, the electron affinity change results in a phase change with smoothed step edges, whereas the MIP results in sharp step edges in the phase change. The smeared edges can be attributed to a built-in potential introduced by the electron affinity difference: The electron affinity of semiconductors, denoted by χ, is the energy difference between the vacuum energy E_{VAC} and the minimum of the conduction band E_{C} at the surface.[84] The physical definition of χ is the energy needed to move one electron in the conduction band minimum of the semiconductor surface to the near surface vacuum.[85] Since the Fermi levels between two semiconductors align when they are connected, a discontinuity of the conduction band edges ΔE_C arises at heterointerfaces, which is given by $\Delta E_\mathrm{C}=\chi_1+(E_{\mathrm{C}_1}-E_{\mathrm{F}_1})-[\chi_2+(E_{\mathrm{C}_2}-E_{\mathrm{F}_2})]$, where χ_1 andχ_2 are the electron affinities of two different materials.[12, 86] In addition the vacuum energy needs to be continuous across the interface. This leads to a screening of the band offsets and hence the electrostatic potential, giving rise to a smeared step-like phase change of transmitted electrons. In contrast, the MIP is related to the core electrons of the atoms and does not affect the electrostatic potential or the free charge carriers. Therefore a MIP change results in a sharp offset of the phase shift.

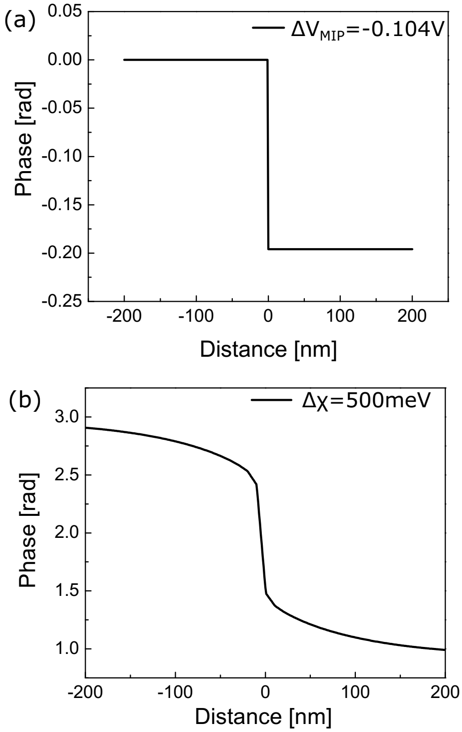

Figure 5.10: Calculated phase changes of transmitted electrons in TEM in case of (a) a MIP change and (b) an electron affinity change at an interface. Phase shifts for (a) a MIP change of -0.104 V between two layers (using the V_MIP values at the $\mathrm{Al_{0.06}Ga_{0.94}N}$/GaN interface derived in Tab. 6.2) and (b) an electron affinity change of 500 meV between two layers. The MIP change induced phase change exhibits a step-like change with sharp edges, whereas the electron affinity change induces an offset in the phase with a smeared step-like shape.

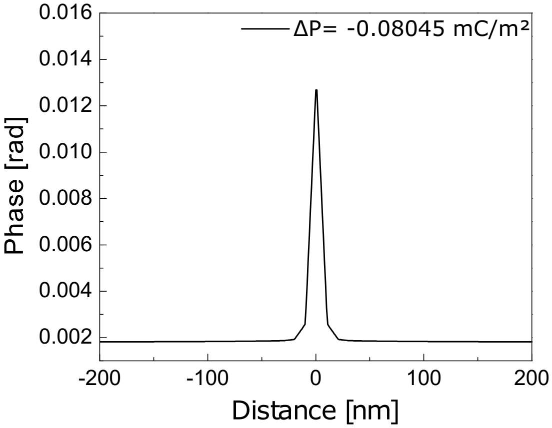

Figure 5.11: Phase changes induced by a polarization change at the interface. The orientation of the peak is dependent on the sign of polarization change.

We also simulate the influence of a polarization change on the phase. Figure 5.11 shows a peak in the calculated phase profile at the interface, which indicates a local potential change. This can be attributed to bound charges (σ_P) at the interface induced by a polarization change.[17] In dielectric materials, the bound sheet charge density is given by the gradient of polarization $\vec{P}$:

$$\sigma_\mathrm{P} = -\nabla \cdot \vec{P} \tag{5.1}$$

The polarization at the heterointerfaces is composed of two components: the piezoelectric polarization $\vec{P}_\mathrm{PE}$ and the spontaneous polarization $\vec{P}_\mathrm{SP}$. For nitrides, the orientation of these two components is parallel or antiparallel (depending on the strain). The total bound sheet charge at the heterointerface is a sum of spontaneous and piezoelectric polarizations induced charge density, $\sigma(\vec{P}_\mathrm{SP})$ and $\sigma(\vec{P}_\mathrm{PE})$, respectively. (see Section 6.4 for the calculation of the polarization changes)

We now turn to a brief discussion about the sign conventions used for the polarizations, surface sheet charges, and phase changes. The peak orientation of the phase profile dependents on the sign of the polarization charge. According to the Eq. 5.1, a negative polarization change at the interface translates into a positive sheet charge $+\sigma$. A positive sheet charge leads to a local minimum of the electrostatic potential and, according to Fig. 5.11, to a maximum of the phase.

5.3 Conclusions

The phase changes across the heterointerfaces have been investigated by off-axis electron holography. Phase contrasts are observed at all three interfaces. From line profiles, extracted from the phase image, the detailed changes at the interface are revealed: a peak with a height of around 0.4 rad at the GaN buffer/GaN substrate interface, a step-like change of 0.17 rad at the $Al_{0.06}Ga_{0.94}N$/GaN interface, and an offset of 0.15 rad in addition to a pronounced dip of 0.25 rad at the $In_{0.05}Ga_{0.95}N/Al_{0.06}Ga_{0.94}N$ interface. These phase changes are attributed to doping concentration changes, surface pinning, MIP changes, electron affinity changes and polarization changes at the interface:

First it is demonstrated in conjunction with self consistent simulations, using the delta-type doping structure at the GaN buffer/GaN substrate homointerface, that the phase changes are enhanced by Fermi level pinning at the surfaces of the TEM lamella. A quantitative determination of the pinning level is performed and used for the following interfaces as surface pinning calibration. Furthermore the pinning level of $E_V + (0.69 \pm 0.2)\,\mathrm{eV}$ is attributed to nitrogen vacancies induced in near surface regions by the FIB preparation of the TEM lamella. On this basis, for the $Al_{0.06}Ga_{0.94}N$/GaN interface, an electron affinity change of $\Delta\chi = +42.5 \pm 50\,\mathrm{meV}$ and a polarization change of $\Delta P = 0 \pm 2\,\mathrm{mC/m^2}$ are measured. For the $In_{0.05}Ga_{0.95}N/Al_{0.06}Ga_{0.94}N$ interface, an electron affinity change of $\Delta\chi = +170 \pm 50\,\mathrm{meV}$ and a polarization change of $\Delta P = +9.7 \pm 2.0\,\mathrm{mC/m^2}$ are obtained. The physical meaning of the values are discussed in Chapter 6.

The here described methodology calibrating the surface electrostatic potential provides the capability to quantitatively characterize the electron affinity and polarization changes at group III-nitride heterostructure interfaces by using off-axis electron holography in conjunction with self-consistent simulations and SIMS.

Chapter 6

Interplay of lattice strain and electronic properties at heterointerfaces

Due to lattice mismatch between the different group III-nitride semiconductors, epitaxially grown heterointerfaces can be expected to be strained. Since strain sensitively changes the electronic properties,[87, 88, 89] it is necessary to quantify the lattice strain in the different layers. In this chapter first the strain is derived experimentally. Then the expected interface polarization and electron affinity changes including their strain-induced components are derived from literature values and compared with the values derived from electron holography.

6.1 Lattice constants and strain

The symbols in Fig. 6.1 shows the a (a) and c (b) lattice constants of each layer measured by STEM. The measured lattice constants were calibrated assuming that the lattice constants of the substrate equal the generally accepted equilibrium values of 318.9 pm [90] and 518.6 pm [91] for a and c lattice constants, respectively. The a lattice constant shows almost no changes across each interface, whereas the lattice constant along c direction changes significantly. This indicates that the layers are biaxially strained.

In order to obtain the strain across the interfaces, we compare the measured lattice constants to the unstrained equilibrium lattice constants. The red dashed lines in Fig. 6.1 illustrate these equilibrium lattice constants of each layer, which are derived by Vegard's law on the basis of those of the respective group III-nitrides:

$$a(\mathrm{Al}_x\mathrm{Ga}_{1-x}\mathrm{N}) = x \cdot a(\mathrm{AlN}) + (1-x) \cdot a(\mathrm{GaN}), \tag{6.1a}$$

and

$$c(\mathrm{Al}_x\mathrm{Ga}_{1-x}\mathrm{N}) = x \cdot c(\mathrm{AlN}) + (1-x) \cdot c(\mathrm{GaN}). \tag{6.1b}$$

The unstrained equilibrium lattice constant of ternary $\mathrm{In}_x\mathrm{Ga}_{1-x}\mathrm{N}$ compounds are determined in analogy.

The strain along each direction are given by

$$\epsilon_1 = \epsilon_2 = \frac{a_{\mathrm{exp}} - a}{a}, \tag{6.2a}$$

and

$$\epsilon_3 = \frac{c_{\mathrm{exp}} - c}{c}, \tag{6.2b}$$

with the error of the strain being

$$\Delta\epsilon = \frac{\partial\epsilon}{\partial a_{\mathrm{exp}}} \times \Delta a_{\mathrm{exp}} = \frac{\Delta a_{\mathrm{exp}}}{a}. \tag{6.2c}$$

where ϵ_1 and ϵ_2 denote to the strain in a and b directions. ϵ_3 is the strain in c direction. Due to the symmetry of the wurtzite structure, ϵ_1 and ϵ_2 are identical. a_{exp} and c_{exp} are the measured lattice constants, whereas a and c are the equilibrium lattice constants. The derived strain values are displayed in Fig. 6.2.

At the $\mathrm{In}_{0.05}\mathrm{Ga}_{0.95}\mathrm{N}/\mathrm{Al}_{0.06}\mathrm{Ga}_{0.94}\mathrm{N}$ interface, the strain values along a direction (ϵ_1) reveal a tensile strain on the $\mathrm{Al}_{0.06}\mathrm{Ga}_{0.94}\mathrm{N}$ side and compressive strain on the $\mathrm{In}_{0.05}\mathrm{Ga}_{0.95}\mathrm{N}$ side, whereas strain along the c direction (ϵ_3) is compressive on the $\mathrm{Al}_{0.06}\mathrm{Ga}_{0.94}\mathrm{N}$ side and tensile on the $\mathrm{In}_{0.05}\mathrm{Ga}_{0.95}\mathrm{N}$ side. According to the linear elasticity theory, the relation of strain in a and c direction is given as

$$\epsilon_1 = -\nu\epsilon_3. \tag{6.3}$$

where ν is the Poisson's ratio, which has typically a positive value ranging between 0.18 and 0.39 for group III-nitrides.[92] Thus, the experimentally measured strain at the $\mathrm{In}_{0.05}\mathrm{Ga}_{0.95}\mathrm{N}/\mathrm{Al}_{0.06}\mathrm{Ga}_{0.94}\mathrm{N}$ interface fulfills expectation of biaxial strain.

In contrast, the derived strains across the $\mathrm{Al}_{0.06}\mathrm{Ga}_{0.94}\mathrm{N}/\mathrm{GaN}$ interface do not agree

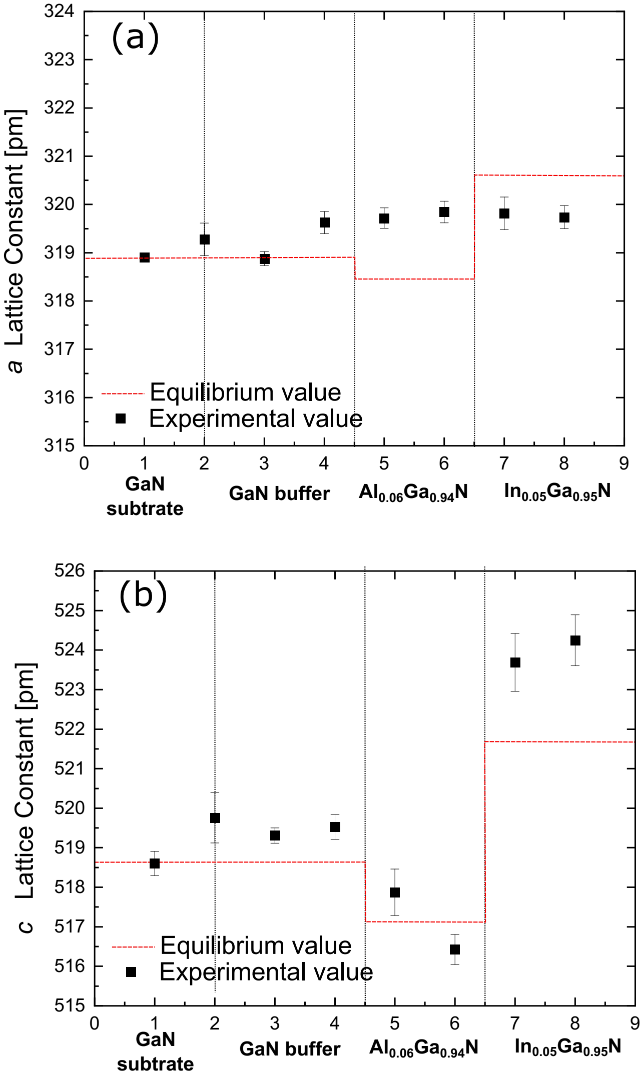

Figure 6.1: Measured (black symbols) and unstrained equilibrium (red dashed lines) values of a (a) and c (b) lattice constants of each layer in the sample. The equilibrium lattice constants of ternary group III-nitrides are calculated by Vegard's law on basis of the binary group III-nitrides' lattice constants. Lattice constants across the $Al_{0.06}Ga_{0.94}N$/GaN and $In_{0.05}Ga_{0.95}N$/$Al_{0.06}Ga_{0.94}N$ interfaces remain almost constant in a direction, but those in c direction change significantly. This indicates a biaxial strain. The experimental lattice constants were calibrated assuming that the substrates' lattice constants correspond to the unstrained generally accepted equilibrium lattice constants.

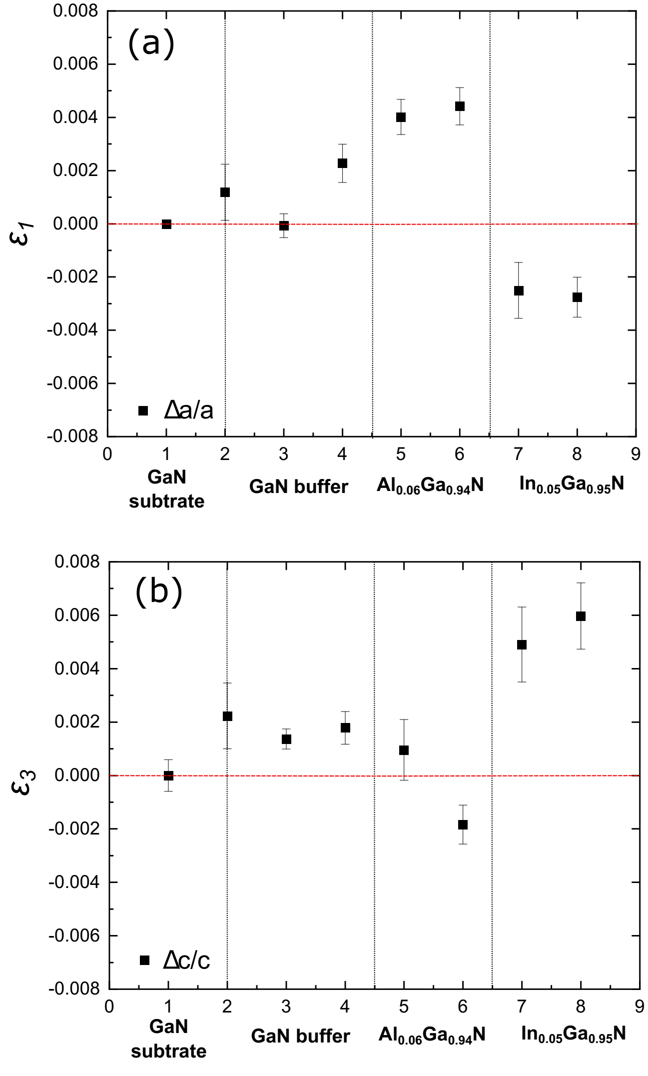

Figure 6.2: Strain along *a* direction ϵ_1 (a) and *c* direction ϵ_3 (b) on both sides of GaN buffer/GaN substrate, $Al_{0.06}Ga_{0.94}N$/GaN, and $In_{0.05}Ga_{0.95}N/Al_{0.06}Ga_{0.94}N$ interfaces, derived from lattice constants measured by STEM (Fig. 6.1).

with the expectations of linear elasticity theory in Eq. 6.3. On both sides of the interface, strain is tensile in a and c directions, which would yield a negative Poisson's ratio ν. The strain thus contains an additional hydrostatic strain component. This indicates an anomalous relaxation at the $\mathrm{Al_{0.06}Ga_{0.94}N/GaN}$ interface, deviating from the expected biaxial strain.

6.2 Derivation of the MIP values for strained ternary group III nitrides

The MIP of each ternary group III nitride layer is derived on basis of MIP values calculated by density functional theory in Ref. [93] for the binary wurtzite structure AlN, GaN, and InN compounds, as shown in Tab. 6.1. First, the unstrained MIP of the ternary compounds is obtained using Vegard's law and the calculated MIP of the respective binary compounds (see Tab. 6.1).

	GaN	AlN	InN	$\mathrm{Al_{0.06}Ga_{0.94}N}$	$\mathrm{In_{0.05}Ga_{0.95}N}$
a lattice constant [$\AA$]	3.189	3.112	3.533	3.184	3.206
c lattice constant [$\AA$]	5.186	4.982	5.693	5.174	5.211
Unstrained MIP [V]	16.89	15.88	18.90	16.829	16.991

Table 6.1: Nominal lattice constants and MIP of unstrained group III nitrides. The MIPs of the binary nitrides GaN, AlN, InN were taken from density functional theory.[93] The MIP and the shown unstrained nominal lattice constants of $\mathrm{Al_{0.06}Ga_{0.94}N}$ and $\mathrm{In_{0.05}Ga_{0.95}N}$ are calculated by Vegard's law from their corresponding binary values.

Second, the actually measured lattice constants obtained by TEM are used to derive the MIP of the strained ternary (and binary) compounds. In first approximation, we assume that the MIP of strained layers scales with the atom density, which can be derived from the measured lattice constants. Therefore, the ratio of the unstrained ($V_{\mathrm{MIP,\ unstrained}}$) to strained MIP ($V_{\mathrm{MIP,\ strained}}$) is proportional to the ratio of the strained to unstrained unit cell volume. Hence, the MIP of a strained layer can be derived using Eq. 6.4, with a_{exp} and c_{exp} being the experimentally measured lattice constants.

$$V_{\mathrm{MIP,strained}} = V_{\mathrm{MIP,unstrained}} \times \frac{a^2 c}{a_{\mathrm{exp}}^2 c_{\mathrm{exp}}}. \tag{6.4}$$

a and c are the unstrained nominal lattice constants. For the ternary compounds, these unstrained lattice constants are derived using Vegards' law from the lattice constants of the respective binary compounds (see Tab. 6.1). Tab. 6.2 gives the thereby obtained strained MIP values for every layer investigated here.

	GaN buffer	$Al_{0.06}Ga_{0.94}N$	$Al_{0.06}Ga_{0.94}N$	$In_{0.05}Ga_{0.95}N$
a lattice constant [$\AA$]	3.1962±0.0023	3.1972±0.0021	3.1985±0.0022	3.1982±0.0034
c lattice constant [$\AA$]	5.1953±0.0032	5.1787±0.0059	5.1643±0.0038	5.2369±0.0073
Strained MIP [V]	16.7835±0.02	16.6791±0.025	16.7123±0.02	16.9927±0.035

Table 6.2: Lattice constants and MIPs of the strained GaN, $Al_{0.06}Ga_{0.94}N$, and $In_{0.05}Ga_{0.95}N$. The MIPs of the strained nitrides are calculated on basis of Eq. 6.4.

The thus obtained MIP values are used for the quantitative determination of the electrons' phase change between the different layers of the investigated specimen.

6.3 Electron affinity changes

6.3.1 Without strain

The derivation of the expected electron affinity change at the interfaces from literature values is seriously hampered by the fact that mostly band gap changes are reported, but no electron affinity changes. Therefore, the following approach is chosen to derive in first approximation the electron affinity change from band gap changes.

First, the electron affinity change ($\Delta\chi$) is approximated by the negative change of the conduction band edge (ΔE_{C}), i.e. the vacuum energy is taken as constant.

$$\Delta\chi = -\Delta E_{\mathrm{C}}. \tag{6.5}$$

Second, the reported change of the band gap (ΔE_{gap}) is the sum of the conduction band edge and valence band edge changes (ΔE_{V}). Hence, with given change of the valence band edge, the change of the conduction band edge can be derived from the reported band gap changes following

$$\Delta E_{\mathrm{C}} = \Delta E_{\mathrm{gap}} + \Delta E_{\mathrm{V}}. \tag{6.6}$$

ΔE_{gap} (meV)	ΔE_{V} (meV)	ΔE_{C} (meV)	$\Delta\chi$ (meV)	Ref.
120	-	-	-	[94]
120	-	-	-	[95]
120	-	-	-	[96]
135	-	-	-	[97]
126	-	-	-	[98]
-	-30	-	-	[99]
-	-30	56	-	[100]
-	-	100	-	[101]
-	-	-	-100	[102]

Table 6.3: Reported experimental and theoretical values for the band gap ΔE_{gap}, conduction band E_{C}, valence band E_{V} and electron affinity χ changes of $\mathrm{Al}_{0.06}\mathrm{Ga}_{0.94}\mathrm{N}$ relative to unstrained GaN.

Note a negative ΔE_{V} value corresponds to a downward offset of E_{V}.

In addition, a separate report of conduction band changes and one of the electron affinity change directly, can be taken into account at this stage. The literature values taken from Refs. [101, 94, 95, 96, 97, 98, 99, 100, 102] used for the $\mathrm{Al}_{0.06}\mathrm{Ga}_{0.94}\mathrm{N}$ layer are given in Tab. 6.3. On this basis the derived unstrained electron affinity change relative to unstrained GaN is then $\Delta\chi$=-89 meV. Note, considering the accuracy of the literature values, particularly the reading of values in printed curves, the accuracy is estimated to ± 20 meV.

For the $\mathrm{In}_{0.05}\mathrm{Ga}_{0.95}\mathrm{N}$ layer, again no direct electron affinity changes relative to GaN are available. Hence, the band gap and valence band changes are taken from Ref. [103] (see Tab. 6.4) to extract the conduction band change relative to GaN. These values are in agreement with other calculations.[104, 96] This yields an electron affinity change for unstrained $\mathrm{In}_{0.05}\mathrm{Ga}_{0.95}\mathrm{N}$ relative to GaN of 190±40 meV. Relative to the adjacent $\mathrm{Al}_{0.06}\mathrm{Ga}_{0.94}\mathrm{N}$ layer the change in electron affinity is 279±45 meV in absence of strain.

6.3.2 With strain

The electron affinity values above change, however, if the layers adjacent to the heterointerfaces are strained. In order to estimate the expected electron affinity change for strained layers, the measured lattice constants and the therefrom derived strain components (see Section 6.1) are taken into account. DFT calculations show

ΔE_{gap} (meV)	ΔE_{V} (meV)	ΔE_{C} (meV)	Ref.
-220	30	-190	[103]

Table 6.4: Reported theoretical values for the band gap ΔE_{gap}, conduction band E_{C}, and valence band E_{V} of $\text{In}_{0.05}\text{Ga}_{0.95}\text{N}$ relative to unstrained GaN.[103]

that the band edges and band gap are changing sensitively with strain.[105, 104] Therefore, we extracted from those calculation the band gap change vs. strain for biaxially strained GaN and hydrostatically strained GaN listed in Tab. 6.5, as well as directly the band gap change for biaxially strained $\text{In}_{0.05}\text{Ga}_{0.95}\text{N}$.

Materials	Strain type	Slope of band gap change vs. strain (eV/strain)	Band gap change (eV)
GaN	biaxial strain	-15.00	
	hydrostatic strain	-23.25	
$\text{In}_{0.05}\text{Ga}_{0.95}\text{N}$	biaxial strain		0.030

Table 6.5: Slope of band gap change vs. strain for GaN. The band gap change is linear with strain for both biaxial and hydrostatic strain. For $\text{In}_x\text{Ga}_{1-x}\text{N}$ the change of band gap vs. strain is nonlinear with the In composition. Hence, the strain is extracted for the In composition of 5% directly from Ref. [105].

Next we assumed that the band gap change of strained GaN ($\text{In}_{0.05}\text{Ga}_{0.95}\text{N}$) is distributed with a ratio of 1:3 (1:6) on the valence and conduction band side, similar to the composition-induced band edge changes relative to GaN in the case of unstrained $\text{Al}_{0.06}\text{Ga}_{0.94}\text{N}$ ($\text{In}_{0.05}\text{Ga}_{0.95}\text{N}$). Finally, in absence of calculations of the strain-induced band gap change for $\text{Al}_{0.06}\text{Ga}_{0.94}\text{N}$, the effect of strain on the electron affinity for GaN is taken in first approximation for the $\text{Al}_{0.06}\text{Ga}_{0.94}\text{N}$ layer.

For the GaN buffer layer, the strain has a large hydrostatic component. Therefore, we used the calculated hydrostatic change of band gap vs. strain for the GaN buffer instead of the biaxial one. We again assumed the 1:3 ratio of valence to conduction band changes for deriving the electron affinity change due to hydrostatic strain.

On this basis the electron affinity changes under consideration of strain at the $Al_{0.06}Ga_{0.94}N/GaN$ and $In_{0.05}Ga_{0.95}N/Al_{0.06}Ga_{0.94}N$ interfaces are -80±28 meV and 204±46 meV, respectively. The values for each layer and the difference at the interfaces are given in Tab. 6.6.

	GaN	$Al_{0.06}Ga_{0.94}N$	$Al_{0.06}Ga_{0.94}N$	$In_{0.05}Ga_{0.95}N$
$\Delta E_{\text{C, unstrained}}$ (meV)	0	89±20	89±20	-190±40
$\Delta E_{\text{gap, strained}}$ (meV)	-47±17	-60±10	-66±11	30±5
$\Delta E_{\text{C, strained}}$ (meV)	-35±17	44±22	40±23	-164±40
$\Delta \chi_{\text{strained}}$ (meV)	35±17	-44±22	-40±23	164±40
Interface $\Delta \chi_{\text{strained}}$ (meV)	-80±28		204±46	

Table 6.6: Bandgap changes $\Delta E_{\text{gap, strained}}$, conduction band offset $\Delta E_{\text{C, strained}}$ (meV) and electron affinity changes $\Delta \chi_{\text{strained}}$ of the layers and across the $Al_{0.06}Ga_{0.94}N/GaN$ and $In_{0.05}Ga_{0.95}N/Al_{0.06}Ga_{0.94}N$ interfaces calculated on basis of literature values, taking into account the experimentally measured strain.

6.4 Polarization changes

6.4.1 Without strain

The strain-free effective spontaneous polarization of the different ternary layers is calculated using Vegard's law from the effective polarization of the binary group III-nitride compounds.[106] This yields theoretical values of polarization changes at the $Al_{0.06}Ga_{0.94}N/GaN$ interface of $\Delta P_{\text{unstrained}}=-2.3\,\text{mC/m}^2$, and at the $In_{0.05}Ga_{0.95}N/Al_{0.06}Ga_{0.94}N$ interface of $\Delta P_{\text{unstrained}}=+16.6\,\text{mC/m}^2$.

6.4.2 With strain

The theoretical values of polarization changes at strained interfaces are derived following Ref.[107]. The polarization in presence of strain is given as

$$P_{\text{strained}} = P_{\text{eff,H}} + (\epsilon_1 + \epsilon_2)(e_{31} - P_{\text{eff,H}}) + \epsilon_3 e_{33}. \qquad (6.7)$$

$P_{\text{eff,H}}$ is the effective spontaneous polarization constant of wurtzite structure, using hexagonal reference structures. e_{31} and e_{33} denote the piezoelectric polarization

	GaN	$Al_{0.06}Ga_{0.94}N$	$Al_{0.06}Ga_{0.94}N$	$In_{0.05}Ga_{0.95}N$	Ref.
e_{31} (C/m^2)	-0.551	-0.5585	-0.5585	-0.55365	[105] and Vegard's law
e_{33} (C/m^2)	1.02	1.05294	1.05294	1.0309	
$P_{\text{eff,H}}$ (C/m^2)	1.312	1.314	1.3143	1.2977	
ϵ_1	0.0023	0.0040	0.0044	-0.0025	Experiments see Fig. 6.2
ϵ_3	0.0018	0.0010	-0.0018	0.0049	
P_{strained} (C/m^2)	1.3055±3	1.3003±3	1.2959±3	1.3120±4	
$\Delta P_{\text{strained}}$ at interfaces (mC/m^2)	-5.0±4		+16.2±5		

Table 6.7: Values used to derive the polarization changes across $Al_{0.06}Ga_{0.94}N$/GaN and $In_{0.05}Ga_{0.95}N/Al_{0.06}Ga_{0.94}N$ interfaces, using Eq. 6.7 taking the measured strain into account.

constants. Since effective spontaneous polarization constants and piezoelectric polarization constants are only available for binary nitrides, we derived the values for ternary compounds by Vegard's law. The polarization for the strained layers are calculated on this basis, taking into account the experimentally measured strain value ϵ_1 and ϵ_2 (see Fig. 6.2). The theoretical expectations of polarization changes across $Al_{0.06}Ga_{0.94}N$/GaN and $In_{0.05}Ga_{0.95}N/Al_{0.06}Ga_{0.94}N$ interfaces are given in Tab. 6.7.

6.5 Discussion

At this stage, we compare the measured electron affinity and polarization changes at the $Al_{0.06}Ga_{0.94}N$/GaN and $In_{0.05}Ga_{0.95}N/Al_{0.06}Ga_{0.94}N$ interfaces with the expected values calculated on basis of literature for unstrained and strained cases (listed in Tab. 6.8).

First, we discuss the unstrained case. For each interface, the measured electron affinity change deviates significantly from that expected for unstrained materials on both sides of the interface. Similarly, the measured polarization changes at both interfaces do not agree with those expected for unstrained interfaces. In fact, the measured and theoretical polarization changes have the opposite sign. Note the theoretical polarization changes were calculated using a hexagonal reference. If a zincblende reference is used, the sign would agree, but in both cases the absolute value is either too large or too small (i.e. +3 mC/m^2 vs measured +9.7 mC/m^2

	Holography	literature	
Interface	$\Delta\chi$ (meV)	$\Delta\chi_{\text{unstrained}}$ (meV)	$\Delta\chi_{\text{biaxial strain}}$ (meV)
$Al_{0.06}Ga_{0.94}N/GaN$	$+43 \pm 50$	-89 ± 20	-80 ± 28
$In_{0.05}Ga_{0.95}N/Al_{0.06}Ga_{0.94}N$	$+170 \pm 50$	$+279 \pm 45$	$+204 \pm 46$
	ΔP (mC/m^2)	$\Delta P_{\text{unstrained}}$ (mC/m^2)	$\Delta P_{\text{biaxial strain}}$ (mC/m^2)
$Al_{0.06}Ga_{0.94}N/GaN$	0 ± 2	$+2.3$	-5.0 ± 4
$In_{0.05}Ga_{0.95}N/Al_{0.06}Ga_{0.94}N$	$+9.7 \pm 2$	-16.6	$+16.2 \pm 5$

Table 6.8: Comparison of expectation values extracted from literature and experimental values measured by off-axis electron holography: electron affinity changes and polarization at the $Al_{0.06}Ga_{0.94}N/GaN$ and $In_{0.05}Ga_{0.95}N/Al_{0.06}Ga_{0.94}N$ interfaces.

for the $In_{0.05}Ga_{0.95}N/Al_{0.06}Ga_{0.94}N$ interface and -3.1 mC/m^2 vs 0 mC/m^2 for the $Al_{0.06}Ga_{0.94}N/GaN$ interface). Hence the unstrained case does not provide a satisfactory agreement.

Hence, we turn to the strained case. For the $In_{0.05}Ga_{0.95}N/Al_{0.06}Ga_{0.94}N$ interface, the electron affinity change expected from literature becomes significantly smaller and now agrees well with the experimentally measured one. Similarly, the theoretical polarization change change the sign and agrees within the error margins with the experimentally measured one.

However, the experimentally measured electron affinity and polarization change values at the $Al_{0.06}Ga_{0.94}N/GaN$ interface still deviate from those expected for the measured strain: Although no polarization change was measured, the theoretical polarization change for the given strain values is $\Delta P_{\text{strained}} = -5 \pm 4$ mC/m^2, i.e. too large. The electron affinity changes measured and expected still have the opposite sign.

These discrepancies are significant and require a further discussion. First for the $In_{0.05}Ga_{0.95}N/Al_{0.06}Ga_{0.94}N$ interface the strain (see Fig. 6.2), i.e. the lattice relaxation, behaves as expected for biaxial strain. In contrast, the lattice constants measured near the $Al_{0.06}Ga_{0.94}N/GaN$ interface point to an anomalous strain and relaxation behavior (see Fig. 6.2). On this basis, we anticipate that the decrease of measured polarization change at the $Al_{0.06}Ga_{0.94}N/GaN$ interface is intimately related to the anomalous lattice relaxation found in Fig. 6.2.

At this stage we recall that a polarization change creates a sheet of bound charges.

This sheet of bound charges can be modified by lattice relaxations[108] through relaxation-induced changes of the polarization. Furthermore, the sheet of bound charges adds a Coulomb interaction energy term to the total energy of the system. Hence, the total energy consists of an electronic energy term, a lattice deformation energy term and a Coulomb interaction energy term. The lattice deformation at the interface can be understood as reduction of the polarization change and hence bound charge at the interface and thereby the Coulomb interaction energy. This is counter balanced by the additional strain energy due to lattice distortion. The experimental observation suggests that the lowering of the Coulomb energy dominates over the lattice deformation energy, hence creating the anomalous interface relaxation. Hence, the origin of the anomalous relaxation at the interface can be explained by the minimization of total energy, driven primarily by the reduction of the Coulomb interaction energy.

6.6 Conclusions

In this chapter the polarization and electron affinity changes at the different interfaces investigated by off-axis electron holography are discussed on basis of the lattice constant changes measured by STEM and compared with expected values derived from experimental and theoretical literature data. The interfaces are shown to be strained due to the lattice mismatch between the layers. However, one interface, i.e. the $Al_{0.06}Ga_{0.94}N/GaN$ interface, exhibits an anomalous lattice relaxation, whereas the other, i.e. $In_{0.05}Ga_{0.95}N/Al_{0.06}Ga_{0.94}N$, interface is biaxially strained as expected. The measured polarization and electron affinity changes of the latter interface agree well with those expected for the measured biaxial strain. In contrast the former interface's zero polarization change and small positive electron affinity change disagrees significantly with the expected values. The disagreement is attributed to the presence of an anomalous strain at the $Al_{0.06}Ga_{0.94}N/GaN$ interface. The driving mechanisms of the formation of an anomalous relaxation at the interface is proposed to be the minimization of the Coulomb interaction energy of polarization-induced bound charges.

Chapter 7

Summary

In this thesis a methodology for a quantitative understanding of electron phase changes in transmission electron microscopy at semiconductor interfaces is developed by combining scanning tunneling microscopy (STM) and spectroscopy (STS), secondary ion mass spectrometry (SIMS), off-axis electron holography in transmission electron microscopy (TEM), scanning transmission electron microscopy (STEM), and self-consistent calculation. This methodology is demonstrated to investigate polarization and electron affinity changes at group III-nitride heterostructure interfaces.

The physical limitation of a quantitative understanding of off-axis electron holography is originating primarily from the sample preparation process, which is necessary to obtain thin lamellas that are suitable for TEM measurements. The preparation creates samples with a high surface-to-bulk ratio and affects the surface properties: Specifically a thin amorphous shell is created that covers the crystalline semiconductor and point defects in the vicinity of the amorphous-crystalline transition region give rise to a Fermi-level pinning at the outside of the crystalline part of the TEM lamella. The implications of this preparation induced surface damage has neither been investigated nor taken into account in quantitative analyzes of off-axis electron holography measurements of III-nitride semiconductors before. It is thus reasonable to assume that the neglect of this fact in earlier studies is one reason for the underestimation of the electron phase contrast in theoretical predictions based on self-consistent electrostatic simulations of semiconducting TEM lamellas. In this thesis, however, the influence of the surface damage induced Fermi-level pinning is taken into account in the analysis of the electrostatic potential obtained by off-axis electron holography.

This is illustrated using a group III-nitride semiconductor heterostructure sample which is specifically designed for tackling the above mentioned problem: Besides the $In_{0.05}Ga_{0.95}N/Al_{0.06}Ga_{0.94}N/GaN$ heterointerfaces of interest, that are investigated quantitatively in a second step, the sample exhibits a delta-type doping structure embedded within GaN (located at the GaN buffer/substrate interface). The different carrier concentrations of the delta-type doping structure, precisely determined by SIMS, give rise to different screening lengths of the surface damage induced Fermi level pinning and thus alter the measured electron phase. Hence, we used experimental electron phase maps, SIMS data, a precisely determined sample thickness, and theoretical phase maps derived from self-consistent electrostatic simulations of the delta-type doping structure, to determine the Fermi level pinning position $[E_V + (0.69 \pm 0.2)\,\mathrm{eV}]$ and thus to fit the theoretical phase maps to the experimental ones. The pinning level position agrees with the charge transition level of nitrogen vacancies, which can be hence anticipated to be the dominant point defects near the amorphous-crystalline transition region.

Since the amorphous shell and the chemical composition of the amorphous-crystalline transition region can be assumed to be identical everywhere throughout the TEM lamella (i.e. for every layer), the calibration of the surface damage induced Fermi level pinning enables, for the first time, a quantitative assessment of the localized electronic properties of group III-nitride heterostructure interfaces using off-axis electron holography: The $Al_{0.06}Ga_{0.94}N/GaN$ and $In_{0.05}Ga_{0.95}N/Al_{0.06}Ga_{0.94}N$ interfaces reveal a step-like phase change with offsets of 0.17 rad and 0.15 rad, respectively. The $In_{0.05}Ga_{0.95}N/Al_{0.06}Ga_{0.94}N$ interface exhibits in addition a dip of 0.25 rad. These phase changes can be attributed to changes of the mean inner potential, the electron affinity, and the polarization. In order to quantify these changes, we first derived the mean inner potential changes from literature values of the binary compounds, using Vegard's law and taking into account strain, as measured by HAADF-STEM. We then applied self-consistent simulations of the electrostatic potential at the heterointerfaces, taking into account the surface damage induced Fermi level pinning, to obtain the electron affinity- and polarization changes. For the $Al_{0.06}Ga_{0.94}N/GaN$ interface, these are $\Delta\chi = +42.5 \pm 50\,\mathrm{meV}$ and $\Delta P = 0 \pm 2\,\mathrm{mC/m^2}$, respectively; for the $In_{0.05}Ga_{0.95}N/Al_{0.06}Ga_{0.94}N$ interface, they are $\Delta\chi = +170 \pm 50\,\mathrm{meV}$ and $\Delta P = +9.7 \pm 2.0\,\mathrm{mC/m^2}$.

The thus obtained values were compared to values derived from literature using the strained a and c lattice constants measured at the interfaces by HAADF-STEM: The measured electron affinity and polarization changes at the $In_{0.05}Ga_{0.95}N/$ $Al_{0.06}Ga_{0.94}N$ interface agree well with the expected values, compatible with a biaxally strained interface. However, for the $Al_{0.06}Ga_{0.94}N/GaN$ interface, a vanishing polarization- and electron affinity change in conjunction with an anomalous strain relaxation is in disagreement with the expected values. Hence we anticipate that a minimization of the system's total energy is achieved by a delicate interplay of the anomalous strain relaxation and the minimization of polarization-induced interface charge.

Finally, the electrostatic potential changes of the group III-nitride heterointerfaces and in particular of the delta-type doping structure have been consolidated using cross-sectional STM and STS. Tunneling spectra measured across the delta-type doping structure reveal locally an enhanced screening (i.e. smaller surface band bending) of the intrinsic empty surface state on freshly cleaved, clean m plane surfaces. The enhanced screening capabilities are attributed to the increased carrier concentration of the delta-type doping structure, in agreement with both, SIMS and off-axis electron holography results.

The methodology developed and presented here for quantitative characterization of the electronic properties of group III-nitride heterointerfaces is applicable to other semiconductor heterointerfaces. However, a proper treatment of the TEM lamella's surface damage by calibrating the damage induced Fermi level pinning is inevitable.

Bibliography

[1] Y. Hao, J. Zhang, B. Shen, and X. Liu, "Progress in Group III nitride semiconductor electronic devices," *Journal of Semiconductors*, vol. 33, p. 081001, aug 2012.

[2] S. Nakamura, S. Pearton, and G. Fasol, *The Blue Laser Diode: The Complete Story*. Springer, 2000. p. 34.

[3] M. R. Krames, O. B. Shchekin, R. Mueller-Mach, G. Mueller, L. Zhou, G. Harbers, and M. G. Craford, "Status and future of high-power light-emitting diodes for solid-state lighting," *J. Display Technol.*, vol. 3, pp. 160–175, Jun 2007.

[4] A. Acharya, "Group III–Nitride Semiconductors: Preeminent Materials for Modern Electronic and Optoelectronic Applications," *Himalayan Physics*, vol. 5, pp. 22–26, Jun. 2015.

[5] M. T. Hardy, D. F. Feezell, S. P. DenBaars, and S. Nakamura, "Group III-nitride lasers: a materials perspective," *Materials Today*, vol. 14, no. 9, pp. 408 – 415, 2011.

[6] J. K. Sheu, F. W. Huang, C. H. Lee, M. L. Lee, Y. H. Yeh, P. C. Chen, and W. C. Lai, "Improved conversion efficiency of GaN-based solar cells with Mn-doped absorption layer," *Applied Physics Letters*, vol. 103, no. 6, p. 063906, 2013.

[7] M. Vecchia, S. Ravyts, G. Van den Broeck, and J. Driesen, "Gallium-nitride semiconductor technology and its practical design challenges in power electronics applications: An overview," *Energies*, vol. 12, p. 2663, 07 2019.

[8] X. H. Wu, L. M. Brown, D. Kapolnek, S. Keller, B. Keller, S. P. DenBaars, and J. S. Speck, "Defect structure of metal-organic chemical vapor deposition-grown epitaxial (0001) GaN/Al_2O_3," *J. Appl. Phys.*, vol. 80, no. 6, pp. 3228–3237, 1996.

[9] M. Kuzuhara and H. Tokuda, "Low-Loss and High-Voltage III-Nitride Transistors for Power Switching Applications," *IEEE Transactions on Electron Devices*, vol. 62, pp. 405–413, Feb 2015.

[10] B. Roul, M. Kumar, M. K. Rajpalke, T. N. Bhat, and S. B. Krupanidhi, "Binary group III-nitride based heterostructures: band offsets and transport properties," *Journal of Physics D: Applied Physics*, vol. 48, p. 423001, sep 2015.

[11] W. R. Frensley, "Chapter 1 - heterostructure and quantum well physics," in *Heterostructures and Quantum Devices* (N. G. Einspruch and W. R. Frensley, eds.), vol. 24 of *VLSI Electronics Microstructure Science*, pp. 1 – 24, Elsevier, 1994.

[12] A. Franciosi and C. G. Van de Walle, "Heterojunction band offset engineering," *Surface Science Reports*, vol. 25, no. 1, pp. 1 – 140, 1996.

[13] M. Matys, B. Adamowicz, A. Domanowska, A. Michalewicz, R. Stoklas, M. Akazawa, Z. Yatabe, and T. Hashizume, "On the origin of interface states at oxide/III-nitride heterojunction interfaces," *Journal of Applied Physics*, vol. 120, no. 22, p. 225305, 2016.

[14] M. Matys, B. Adamowicz, Y. Hori, and T. Hashizume, "Direct measurement of donor-like interface state density and energy distribution at insulator/AlGaN interface in metal/Al_2O_3/AlGaN/GaN by photocapacitance method," *Applied Physics Letters*, vol. 103, no. 2, p. 021603, 2013.

[15] C. Roff, J. Benedikt, P. J. Tasker, D. J. Wallis, K. P. Hilton, J. O. Maclean, D. G. Hayes, M. J. Uren, and T. Martin, "Analysis of DC–RF Dispersion in AlGaN/GaN HFETs Using RF Waveform Engineering," *IEEE Transactions on Electron Devices*, vol. 56, pp. 13–19, Jan 2009.

[16] F. Bernardini, V. Fiorentini, and D. Vanderbilt, "Spontaneous polarization and piezoelectric constants of III-V nitrides," *Phys. Rev. B*, vol. 56, no. 16, p. R10024, 1997.

[17] O. Ambacher, R. Dimitrov, M. Stutzmann, B. Foutz, M. Murphy, J. Smart, J. Shealy, N. Weimann, K. Chu, M. Chumbes, B. Green, A. Sierakowski, W. Schaff, and L. Eastman, "Role of Spontaneous and Piezoelectric Polarization Induced Effects in Group-III Nitride Based Heterostructures and Devices," *physica status solidi (b)*, vol. 216, no. 1, pp. 381–389, 1999.

[18] R. Chaudhuri, S. J. Bader, Z. Chen, D. A. Muller, H. G. Xing, and D. Jena, "A polarization-induced 2D hole gas in undoped gallium nitride quantum wells," *Science*, vol. 365, pp. 1454–1457, 2019.

[19] M. A. Khan, J. N. Kuznia, J. M. V. Hove, N. Pan, and J. Carter, "Observation of a two-dimensional electron gas in low pressure metalorganic chemical vapor deposited GaN-$\mathrm{Al_xGa_{1\text{-}x}N}$ heterojunctions," *Appl. Phys. Lett.*, vol. 60, no. 24, pp. 3027–3029, 1992.

[20] H. S. Kim, J. Y. Lin, H. X. Jiang, W. W. Chow, A. Botchkarev, and H. Morkoç, "Piezoelectric effects on the optical properties of GaN/$\mathrm{Al}_x\mathrm{Ga}_{1-x}\mathrm{N}$ multiple quantum wells," *Applied Physics Letters*, vol. 73, no. 23, pp. 3426–3428, 1998.

[21] M.-H. Kim, M. F. Schubert, Q. Dai, J. K. Kim, E. F. Schubert, J. Piprek, and Y. Park, "Origin of efficiency droop in GaN-based light-emitting diodes," *Applied Physics Letters*, vol. 91, no. 18, p. 183507, 2007.

[22] T. Takeuchi, C. Wetzel, S. Yamaguchi, H. Sakai, H. Amano, I. Akasaki, Y. Kaneko, S. Nakagawa, Y. Yamaoka, and N. Yamada, "Determination of piezoelectric fields in strained gainn quantum wells using the quantum-confined stark effect," *Applied Physics Letters*, vol. 73, no. 12, pp. 1691–1693, 1998.

[23] C. Wetzel, T. Takeuchi, H. Amano, and I. Akasaki, "Piezoelectric Franz–Keldysh effect in strained GaInN/GaN heterostructures," *Journal of Applied Physics*, vol. 85, no. 7, pp. 3786–3791, 1999.

[24] D. M. Graham, A. Soltani-Vala, P. Dawson, M. J. Godfrey, T. M. Smeeton, J. S. Barnard, M. J. Kappers, C. J. Humphreys, and E. J. Thrush, "Optical and microstructural studies of InGaN/GaN single-quantum-well structures," *Journal of Applied Physics*, vol. 97, no. 10, p. 103508, 2005.

[25] M. D. Craven, S. H. Lim, F. Wu, J. S. Speck, and S. P. DenBaars, "Structural characterization of nonpolar $(11\bar{2}0)$ a-plane gan thin films grown on $(1\bar{2}02)$ r-plane sapphire," *Applied Physics Letters*, vol. 81, no. 3, pp. 469–471, 2002.

[26] P. Waltereit, O. Brandt, A. Trampert, H. T. Grahn, J. Menniger, M. Ramsteiner, M. Reiche, and K. H. Ploog, "Nitride semiconductors free of electrostatic fields for efficient white light-emitting diodes," *Nature*, vol. 406, pp. 865–868, aug 2000.

[27] C. Durand, C. Bougerol, J.-F. Carlin, G. Rossbach, F. Godel, J. Eymery, P.-H. Jouneau, A. Mukhtarova, R. Butté, and N. Grandjean, "*M*-Plane

GaN/InAlN Multiple Quantum Wells in Core-Shell Wire Structure for UV Emission," *ACS Photonics*, vol. 1, no. 1, pp. 38–46, 2014.

[28] E. R. Buß, P. Horenburg, U. Rossow, H. Bremers, T. Meisch, M. Caliebe, F. Scholz, and A. Hangleiter, "Non- and semipolar AlInN one-dimensionally lattice-matched to GaN for realization of relaxed buffer layers for strain engineering in optically active GaN-based devices," *phys. stat. sol. (b)*, vol. 253, no. 1, pp. 84–92, 2016.

[29] M. F. Schubert, J. Xu, J. K. Kim, E. F. Schubert, M. H. Kim, S. Yoon, S. M. Lee, C. Sone, T. Sakong, and Y. Park, "Polarization-matched GaInN/AlGaInN multi-quantum-well light-emitting diodes with reduced efficiency droop," *Appl. Phys. Lett.*, vol. 93, no. 4, p. 041102, 2008.

[30] M. Jetter, C. Wächter, A. Meyer, and P. Michler, "MOVPE grown quaternary AlInGaN layers for polarization matched quantum wells and efficient active regions," *physica status solidi c*, vol. 8, no. 7-8, pp. 2163–2166, 2011.

[31] D. Jena, J. Simon, A. K. Wang, Y. Cao, K. Goodman, J. Verma, S. Ganguly, G. Li, K. Karda, V. Protasenko, C. Lian, T. Kosel, P. Fay, and H. Xing, "Polarization-engineering in group III-nitride heterostructures: New opportunities for device design," *physica status solidi (a)*, vol. 208, no. 7, pp. 1511–1516, 2011.

[32] H. H. Yao, Y. Lu, K. H. Li, F. A. Qatari, C. H. Liao, and X. Li, "Polarization matched c-plane III nitride quantum well structure," in *Light-Emitting Devices, Materials, and Applications* (J. K. Kim, M. R. Krames, and M. Strassburg, eds.), vol. 10940 of *Proc. SPIE*, p. 109400K, 2019.

[33] S. Chung, S. R. Johnson, Y. H. Zhang, D. J. Smith, and M. R. McCartney, "Off-axis electron holographic potential mapping across AlGaAs/AlAs/GaAs heterostructures," *J. Appl. Phys.*, vol. 105, p. 014910, 2009.

[34] N. Fujimura, A. Ohta, K. Makihara, and S. Miyazaki, "Evaluation of valence band top and electron affinity of SiO_2 and Si-based semiconductors using X-ray photoelectron spectroscopy," *Japanese Journal of Applied Physics*, vol. 55, p. 08PC06, jul 2016.

[35] V. Thakur and S. Shivaprasad, "Electronic structure of GaN nanowall network analysed by XPS," *Applied Surface Science*, vol. 327, pp. 389 – 393, 2015.

[36] C. L. Wu, C. H. Chen, and S. Gwo, "Valence band offset of wurtzite InN/AlN heterojunction determined by photoelectron spectroscopy," *Appl. Phys. Lett.*, vol. 88, no. 3, p. 032105, 2006.

[37] Y. Yang, Y. Takahashi, A. Tsurumaki-Fukuchi, M. Arita, M. Moors, M. Buckwell, A. Mehonic, and A. J. Kenyon, "Probing electrochemistry at the nanoscale: in situ TEM and STM characterizations of conducting filaments in memristive devices," *J. Electroceram.*, 2017.

[38] O. Krivanek, T. Lovejoy, and N. Dellby, "Aberration-corrected STEM for atomic-resolution imaging and analysis," *Journal of Microscopy*, vol. 259, no. 3, pp. 165–172, 2015.

[39] M. R. McCartney and D. J. Smith, "Electron holography: Phase imaging with nanometer resolution," *Annual Review of Materials Research*, vol. 37, no. 1, pp. 729–767, 2007.

[40] J. K. Weiss, W. J. de Ruijter, M. Gajdardziska-Josifovska, M. R. McCartney, and D. J. Smith, "Applications of electron holography to the study of interfaces," *Ultramicroscopy*, vol. 50, pp. 301–311, 1993.

[41] M. R. McCartney, F. A. Ponce, and J. Cai, "Mapping electrostatic potential across an AlGaN/InGaN/AlGaN diode by electron holography," *Appl. Phys. Lett.*, vol. 76, p. 3055, 2000.

[42] M. R. McCartney, N. Agarwal, S. Chung, D. A. Cullen, M. G. Han, K. He, L. Li, H. Wang, L. Zhou, and D. J. Smith, "Quantitative phase imaging of nanoscale electrostatic and magnetic fields using off-axis electron holography," *Ultramicroscopy*, vol. 110, no. 5, pp. 375 – 382, 2010. Hannes Lichte 65th Birthday.

[43] L. Zhou, D. A. Cullen, D. J. Smith, M. R. McCartney, A. Mouti, M. Gonschorek, E. Feltin, J. F. Carlin, and N. Grandjean, "Polarization field mapping of $Al_{0.85}In_{0.15}N$/AlN/GaN heterostructure," *Appl. Phys. Lett.*, vol. 94, p. 121909, 2009.

[44] Q. Y. Wei, T. Li, J. Y. Huang, F. A. Ponce, E. Tschumak, A. Zado, and D. J. As, "Free carrier accumulation at cubic AlGaN/GaN heterojunctions," *Appl. Phys. Lett.*, vol. 100, p. 142108, 2012.

[45] G. Binnig, H. Rohrer, C. Gerber, and E. Weibel, "Surface Studies by Scanning Tunneling Microscopy," *Phys. Rev. Lett.*, vol. 49, pp. 57–61, 1982.

[46] G. Binnig, H. Rohrer, C. Gerber, and E. Weibel, "Tunneling through a controllable vacuum gap," *Appl. Phys. Lett.*, vol. 40, no. 2, pp. 178–181, 1982.

[47] W. Nolting, *Grundkurs Theoretische Physik 5/1.* Springer, 7 ed., 2009.

[48] F. Schwabl, *Quantum Mechanics.* Springer, 4th edition ed., 2007.

[49] G. Binnig and H. Rohrer, "Scanning tunneling Microscopy," *Surf. Sci.*, vol. 126, pp. 236–244, 1983.

[50] J. Bardeen, "Tunnelling from a many-particle point of view," *Phys. Rev. Lett.*, vol. 6, no. 2, pp. 57–59, 1961.

[51] A. D. Gottlieb and L. Wesoloski, "Bardeen's tunnelling theory as applied to scanning tunnelling microscopy: a technical guide to the traditional interpretation," *Nanotechnol.*, vol. 17, no. 8, p. R57, 2006.

[52] P. Dirac, "The question theory of the emission and absorption of radiation," *Proceedings of the Royal Society of London Series A*, vol. 114, no. 767, pp. 243–265, 1927.

[53] G. Wentzel, "Über strahlungslose Quantensprünge," *Zeitschrift für Physik*, vol. 43, pp. 524–530, 1927.

[54] J. Tersoff and D. R. Hamann, "Theory and Application for the Scanning Tunneling Microscope," *Phys. Rev. Lett.*, vol. 50, pp. 1998–2001, Jun 1983.

[55] J. Tersoff and D. R. Hamann, "Theory of the scanning tunneling microscope," *Phys. Rev. B*, vol. 31, pp. 805–813, Jan 1985.

[56] B. Voigtländer, *Scanning Probe Microscopy: Atomic Force Microscopy and Scanning Tunneling Microscopy.* Nanoscience and Technology, Springer, 2015.

[57] G. D, "A new microscopic principle," *Nature*, vol. 161, pp. 777–778, May 1948.

[58] M. Lehmann, E. Völkl, and F. Lenz, "Reconstruction of electron off-axis holograms: a new and fast alternative method," *Ultramicroscopy*, vol. 54, no. 2, pp. 335 – 344, 1994.

[59] R. E. Dunin-Borkowski, A. Kovács, T. Kasama, M. R. McCartney, and D. J. Smith, *Springer Handbook of Microscopy*, ch. 16. Electron Holography, pp. 767–818. Springer Handbook, Springer, Cham, 2019.

[60] M. Schnedler, V. Portz, P. H. Weidlich, R. E. Dunin-Borkowski, and Ph. Ebert, "Quantitative description of photoexcited scanning tunneling spectroscopy and its application to the GaAs(110) surface," *Phys. Rev. B*, vol. 91, p. 235305, 2015.

[61] J. P. Ibe, P. P. Bey, S. L. Brandow, R. A. Brizzolara, N. A. Burnham, D. P. DiLella, K. P. Lee, C. R. K. Marrian, and R. J. Colton, "On the electrochemical etching of tips for scanning tunneling microscopy," *J. Vac. Sci. Technol. A*, vol. 8, no. 4, pp. 3570–3575, 1990.

[62] M. Schnedler, *Quantitative scanning tunneling spectroscopy of non-polar compound semiconductor surfaces.* PhD thesis, RWTH Aachen University, 2015.

[63] Ph. Ebert, "Untersuchungen der InP(110)-Oberfläche mit dem Rastertunnelmikroskop," Diplomarbeit, RWTH Aachen, 1990.

[64] Ph. Ebert and K. Szot, "Scanning Probe Analysis," in *Nanoelectronics and Information Technology* (R. Waser, ed.), ch. 11, pp. 255–281, Weinheim: Wiley-VCH, 3 ed., 2012.

[65] Y. Yabuuchi, S. Tametou, T. Okano, S. Inazato, S. Sadayama, Y. Yamamoto, K. Iwasaki, and Y. Sugiyama, "A study of the damage on FIB-prepared TEM samples of $\mathrm{Al}_x\mathrm{Ga}_{1-x}\mathrm{As}$," *Journal of electron microscopy*, vol. 53, pp. 471–7, 2004.

[66] A. C. Twitchett, R. E. Dunin-Borkowski, R. F. Broom, and P. A. Midgley, "Quantitative electron holography of biased semiconductor devices," *Journal of Physics: Condensed Matter*, vol. 16, pp. S181–S192, dec 2003.

[67] Ph. Ebert, L. Ivanova, and H. Eisele, "Scanning tunneling microscopy on unpinned GaN$(1\bar{1}00)$ surfaces: Invisibility of valence-band states," *Phys. Rev. B*, vol. 80, p. 085316, 2009.

[68] N. D. Jäger, E. R. Weber, K. Urban, and Ph. Ebert, "Importance of carrier dynamics and conservation of momentum in atom-selective STM imaging and band gap determination of GaAs(110)," *Phys. Rev. B*, vol. 67, p. 165327, 4 2003.

[69] L. Ivanova, S. Borisova, H. Eisele, M. Dähne, A. Laubsch, and Ph. Ebert, "Surface states and origin of the Fermi level pinning on nonpolar GaN(100) surfaces," *Appl. Phys. Lett.*, vol. 93, no. 19, p. 192110, 2008.

[70] J. E. Northrup and J. Neugebauer, "Theory of GaN$(10\bar{1}0)$ and $(11\bar{2}0)$ surfaces," *Phys. Rev. B*, vol. 53, pp. R10477–R10480, 1996.

[71] M. Schnedler, V. Portz, H. Eisele, R. E. Dunin-Borkowski, and Ph. Ebert, "Polarity-dependent pinning of a surface state," *Phys. Rev. B*, vol. 91, p. 205309, 2015.

[72] H. Eisele, J. Schuppang, M. Schnedler, M. Duchamp, C. Nenstiel, V. Portz, T. Kure, M. Bügler, A. Lenz, M. Dähne, A. Hoffmann, S. Gwo, S. Choi, J. S. Speck, R. E. Dunin-Borkowski, and Ph. Ebert, "Intrinsic electronic properties of high-quality wurtzite InN," *Phys. Rev. B*, vol. 94, no. 24, p. 245201, 2016.

[73] L. Lymperakis, P. H. Weidlich, H. Eisele, M. Schnedler, J.-P. Nys, B. Grandidier, D. Stievenard, R. E. Dunin-Borkowski, J. Neugebauer, and Ph. Ebert, "Hidden surface states at non-polar GaN $(10\bar{1}0)$ facets: Intrinsic pinning of nanowires," *Appl. Phys. Lett.*, vol. 103, no. 15, p. 152101, 2013.

[74] L. Lymperakis private communication.

[75] Ernst Ruska-Centre for Microscopy and Spectroscopy with Electrons (ER-C), "FEI Titan G2 60-300 HOLO," *Journal of large-scale research facilities*, vol. 2, p. A44, 2016.

[76] M. Suzuki, T. Uenoyama, and A. Yanase, "First-principles calculations of effective-mass parameters of AlN and GaN," *Phys. Rev. B*, vol. 52, pp. 8132–8139, Sep 1995.

[77] M. O'Keeffe and J. C. H. Spence, "On the average Coulomb potential (Σ_0) and constraints on the electron density in crystals," *Acta Crystallographica Section A*, vol. 50, pp. 33–45, Jan. 1994.

[78] L. Houben, M. Luysberg, and T. Brammer, "Illumination effects in holographic imaging of the electrostatic potential of defects and *pn* junctions in transmission electron microscopy," *Phys. Rev. B*, vol. 70, p. 165313, 2004.

[79] T. K. Zywietz, J. Neugebauer, and M. Scheffler, "The adsorption of oxygen at GaN surfaces," *Applied Physics Letters*, vol. 74, no. 12, pp. 1695–1697, 1999.

[80] S. Limpijumnong and C. G. Van de Walle, "Diffusivity of native defects in GaN," *Phys. Rev. B*, vol. 69, p. 035207, 2004.

[81] A. Kyrtsos, M. Matsubara, and E. Bellotti, "Migration mechanisms and diffusion barriers of carbon and native point defects in GaN," *Phys. Rev. B*, vol. 93, p. 245201, 2016.

[82] Q. Yan, A. Janotti, M. Scheffler, and C. G. Van de Walle, "Role of nitrogen vacancies in the luminescence of Mg-doped GaN," *Appl. Phys. Lett.*, vol. 100, no. 14, p. 142110, 2012.

[83] J. L. Lyons and C. G. V. de Walle, "Computationally predicted energies and properties of defects in GaN," *npj Comput. Mater.*, vol. 3, p. 12, 2017.

[84] J. S. Escher, “NEA Semiconductor Photoemitters,” *Semiconductors and Semimetals*, vol. 15, no. Supplement C, pp. 195–300, 1981.

[85] A. Nussbaum, “The Theory of Semiconducting Junctions,” *Semiconductors and Semimetals*, vol. 15, no. Supplement C, pp. 39–194, 1981.

[86] J. L. Shay, S. Wagner, and J. C. Phillips, “Heterojunction band discontinuities,” *Applied Physics Letters*, vol. 28, no. 1, pp. 31–33, 1976.

[87] A. Bykhovski, B. Gelmont, and M. Shur, “The influence of the strain-induced electric field on the charge distribution in GaN-AlN-GaN structure,” *Journal of Applied Physics*, vol. 74, no. 11, pp. 6734–6739, 1993.

[88] A. Romanov, T. Baker, S. Nakamura, J. Speck, and A. Romanov, “Strain-induced polarization in wurtzite III-nitride semipolar layers,” *J. Appl. Phys.*, vol. 100, no. 2, pp. 701–706, 2006.

[89] M. D. Rahmani and P. Masri, “Electronic properties of strained heterostructures,” *Journal de Physique III*, vol. 3, 09 1993.

[90] W. Gian, M. Skowronski, and G. S. Rohrer, “Structural Defects and Their Relationship to Nucleation of Gan Thin Films,” *MRS Proceedings*, vol. 423, p. 475, 1996.

[91] V. Bougrov, “Properties of Advanced SemiconductorMaterials GaN, AlN, InN, BN, SiC, SiGe,” in *Gallium Nitride (GaN)* (M. E. Levinshtein, S. L. Rumyantsev, and A. Zubrilov, eds.), pp. 1–30, John Wiley and Sons, 2001.

[92] H. Morkoç, *Handbook of Nitride Semiconductors and Devices*, ch. 1, pp. 15–35. John Wiley & Sons, Ltd, 2009.

[93] M. Schowalter, A. Rosenauer, D. Lamoen, P. Kruse, and D. Gerthsen, “Ab initio computation of the mean inner Coulomb potential of wurtzite-type semiconductors and gold,” *Appl. Phys. Lett.*, vol. 88, p. 232108, 2006.

[94] T. J. Ochalski, B. Gil, P. Lefebvre, N. Grandjean, M. Leroux, J. Massies, S. Nakamura, and H. Morkoc, “Photoreflectance investigations of the bowing parameter in AlGaN alloys lattice-matched to GaN,” *Appl. Phys. Lett.*, vol. 74, no. 22, pp. 3353–3355, 1999.

[95] D. Brunner, H. Angerer, E. Bustarret, F. Freudenberg, R. Höpler, R. Dimitrov, O. Ambacher, and M. Stutzmann, “Optical constants of epitaxial AlGaN films and their temperature dependence,” *J. Appl. Phys.*, vol. 82, p. 5090, 1997.

[96] R. R. Pelá, C. Caetano, M. Marques, L. G. Ferreira, J. Furthmüller, and L. K. Teles, "Accurate band gaps of AlGaN, InGaN, and AlInN alloys calculations based on LDA-1/2 approach," *Appl. Phys. Lett.*, vol. 98, no. 15, p. 151907, 2011.

[97] B. Meyer, G. Steude, A. Göldner, A. Hoffmann, H. Amano, and I. Akasaki, "Photoluminescence Investigations of AlGaN on GaN Epitaxial Films," *phys. stat. sol. (b)*, vol. 216, no. 1, pp. 187–191, 1999.

[98] D. Mourad and G. Czycholl, "Theory of band gap bowing of disordered substitutional II-VI and III-V semiconductor alloys," *Eur. Phys. J. B*, vol. 85, p. 153, 2012.

[99] P. G. Moses, M. Miao, Q. Yan, and C. G. Van de Walle, "Hybrid functional investigations of band gaps and band alignments for AlN, GaN, InN, and InGaN," *J. Chem. Phys.*, vol. 134, no. 8, p. 084703, 2011.

[100] A. Kyrtsos, M. Matsubara, and E. Bellotti, "First-principles study of the impact of the atomic configuration on the electronic properties of $\mathrm{Al}_x\mathrm{Ga}_{1-x}\mathrm{N}$ alloys," *Phys. Rev. B*, vol. 99, p. 035201, 2019.

[101] C. Coughlan, S. Schulz, M. A. Caro, and E. P. O'Reilly, "Band gap bowing and optical polarization switching in AlGaN alloys," *phys. stat. sol. (b)*, vol. 252, no. 5, pp. 879–884, 2015.

[102] S. P. Grabowski, M. Schneider, H. Nienhaus, W. Mönch, R. Dimitrov, O. Ambacher, and M. Stutzmann, "Electron affinity of $\mathrm{Al}_x\mathrm{Ga}_{1-x}\mathrm{N}(0001)$ surfaces," *Appl. Phys. Lett.*, vol. 78, no. 17, pp. 2503–2505, 2001.

[103] P. G. Moses and C. G. Van de Walle, "Band bowing and band alignment in InGaN alloys," *Appl. Phys. Lett.*, vol. 96, no. 2, p. 021908, 2010.

[104] Y. Cui, S. Lee, C. Freysoldt, and J. Neugebauer, "Role of biaxial strain and microscopic ordering for structural and electronic properties of $\mathrm{In}_x\mathrm{Ga}_{1-x}\mathrm{N}$," *Phys. Rev. B*, vol. 92, p. 085204, Aug 2015.

[105] Q. Yan, P. Rinke, A. Janotti, M. Scheffler, and C. G. Van de Walle, "Effects of strain on the band structure of group-III nitrides," *Phys. Rev. B*, vol. 90, p. 125118, Sep 2014.

[106] F. Bernardini and V. Fiorentini, "Nonlinear macroscopic polarization in III-V nitride alloys," *Phys. Rev. B*, vol. 64, p. 085207, Aug 2001.

[107] C. E. Dreyer, A. Janotti, C. G. Van de Walle, and D. Vanderbilt, “Correct Implementation of Polarization Constants in Wurtzite Materials and Impact on III-Nitrides,” *Phys. Rev. X*, vol. 6, p. 021038, Jun 2016.

[108] R. E. Dunin-Borkowski, W. O. Saxton, and W. M. Stobbs, “The Electrostatic Contribution to the Forward-Scattering Potential at a Space Charge Layer in High-Energy Electron Diffraction. I. Theory Neglecting the Effects of Fringing Fields,” *Acta Cryst.*, vol. A52, pp. 705–711, 1996.

Acknowledgement

First of all, I would like to thank Prof. Dr. R. Dunin-Borkowski for offering the opportunity to prepare my PhD thesis at the Institute for Microstructure Research of the Peter Grünberg Institute at the Forschungszentrum Jülich and in addition for many valuable scientific discussions.

I would like to express my sincere gratitude to Priv.-Doz. Dr. Ph. Ebert for supervising my thesis, for guidance during my PhD, and for helpful scientific discussions.

In addition I would like to thank Prof. Dr. J. Mayer from the Gemeinschaftslabor für Elektronenmikroskopie (GFE) der RWTH Aachen for the co-supervision of my PhD thesis.

I would like to thank Prof. Dr. N. Grandjean, Dr. R. Butté, and Dr. J.-F. Carlin from École Polytechnique Féderale de Lausanne, Switzerland for generously providing me with the samples and for their help with the interpretation and assessment of the experimental results.

I also would like to thank Prof. Dr. H. Eisele from the Institut für Festkörperphysik at the Technische Universität Berlin for valuable scientific discussions.

I would like to thank Dr. M. Schnedler for the simulation and generous support during the whole PhD.

Moreover I would like to thank Dr. F. Zheng, Dr. Q. Lan and Dr. Y. Lu for their kind support on measurements and discussions.

My thanks also go to Dr. D. Song, Dr. H. Du, Dr. L. Jin and Z. Ma for their helpful suggestions and discussions.

I would like to thank D. Meertens, M. Kruth and L. Kibkalo for their assistance with specimen preparation.

I would like to thank K. H. Graf for technical support and the maintenance of technical equipment.

Furthermore I would like to express my sincere thankfulness to my colleagues and former colleagues L. Freter, R. Gehlhaar, Dr. V. Portz and Dr. L. Zhang for the countless help and scientific discussions.

I would like to thank my parents for their support.

Band / Volume 50
Investigation of switching mechanism in Ta_2O_5-based ReRAM devices
K. Wonjoo (2017), iii, 138 pp
ISBN: 978-3-95806-261-0

Band / Volume 51
Development of ReRAM-based Devices for Logic- and Computation-in-Memory Applications
T. Breuer (2017), x, 179 pp
ISBN: 978-3-95806-270-2

Band / Volume 52
Resistive switching memory devices from atomic layer deposited binary and ternary oxide thin films
N. Aslam (2017), X, 172 pp
ISBN: 978-3-95806-274-0

Band / Volume 53
Operando X-ray photoemission electron microscopy (XPEEM) investigations of resistive switching metal-insulator-metal devices
C. J. Schmitz (2017), IX, 153 pp
ISBN: 978-3-95806-283-2

Band / Volume 54
Optimization of powder and ceramic processing, electrical characterization and defect chemistry in the system $Yb_xCa_{1-x}MnO_3$
M. Rahmani (2018), XIV, 164 pp
ISBN: 978-3-95806-323-5

Band / Volume 55
Organic-Metal Hybrid Interfaces at the Mesoscopic Scale
G. Zamborlini (2018), xi, 133 pp
ISBN: 978-3-95806-328-0

Band / Volume 56
Configurable frequency synthesizer for large scale physics experiments
N. Parkalian (2019), xxi, 114 pp
ISBN: 978-3-95806-393-8

Band / Volume 57
Resistive switching phenomena in stacks of binary transition metal oxides grown by atomic layer deposition
H. Zhang (2019), ix, 196 pp
ISBN: 978-3-95806-399-0

Band / Volume 58
Element-Selective Investigation of Femtosecond Spin Dynamics in Ni_xPd_{1-x} Magnetic Alloys using Extreme Ultraviolet Radiation
S. Gang (2019), 93, xx pp
ISBN: 978-3-95806-411-9

Band / Volume 59
Defect engineering in oxide thin films
F. V. E. Hensling (2019), 10, 164 pp
ISBN: 978-3-95806-424-9

Band / Volume 60
Chemical control of the electrical surface properties of *n*-doped transition metal oxides
M. Andrä (2019), X, 150, XXXVIII pp
ISBN: 978-3-95806-448-5

Band / Volume 61
Digital Signal Processing and Mixed Signal Control of Receiver Circuitry for Large-Scale Particle Detectors
P. Muralidharan (2020), xv, 109 pp
ISBN: 978-3-95806-489-8

Band / Volume 62
Development of Electromagnetic Induction Measurement and Inversion Methods for Soil Electrical Conductivity Investigations
X. Tan (2020), ix, 124 pp
ISBN: 978-3-95806-490-4

Band / Volume 63
Novel System Approach for a mm-range Precision Indoor Positioning System
R. Xiong (2020), xi, 144 pp
ISBN: 978-3-95806-517-8

Band / Volume 64
Quantitative investigation of group III-nitride interfaces by a combination of scanning tunneling microscopy and off-axis electron holography
Y. Wang (2021), 102 pp
ISBN: 978-3-95806-534-5

Weitere ***Schriften des Verlags im Forschungszentrum Jülich*** unter
http://wwwzb1.fz-juelich.de/verlagextern1/index.asp

Information
Band / Volume 64
ISBN 978-3-95806-534-5

Mitglied der Helmholtz-Gemeinschaft

JÜLICH
Forschungszentrum